1. Report No.	2. Government Accession No.	3. Recipient's Catalog No.
FHWA/TX-05/0-4524-2		

4. Title and Subtitle	5. Report Date
MEASUREMENTS OF SURFACE ENERGY AND ITS RELATIONSHIP TO MOISTURE DAMAGE	May 2005
	6. Performing Organization Code

7. Author(s)	8. Performing Organization Report No.
Robert L. Lytton, Eyad A. Masad, Corey Zollinger, Rifat Bulut, Dallas Little	0-4524-2

9. Performing Organization Name and Address	10. Work Unit No. (TRAIS)
Texas Transportation Institute The Texas A&M University System College Station, Texas 77843-3135	11. Contract or Grant No. Project 0-4524

12. Sponsoring Agency Name and Address	13. Type of Report and Period Covered
Texas Department of Transportation Research and Technology Implementation Office P. O. Box 5080 Austin, Texas 78763-5080	Technical Report: September 2003-May 2005
	14. Sponsoring Agency Code

15. Supplementary Notes

Project performed in cooperation with the Texas Department of Transportation and the Federal Highway Administration.

Project Title: Application of Surface Energy Measurements to Evaluate Moisture Susceptibility of Asphalt and Aggregates

16. Abstract

Moisture damage in asphalt mixes can be defined as loss of strength and durability due to the presence of moisture at the binder-aggregate interface (adhesive failure) or within the binder (cohesive failure). This research focuses on the evaluation of the susceptibility of aggregates and asphalts to moisture damage through understanding the micro-mechanisms that influence adhesive bond between aggregates and asphalt and the cohesive strength and durability of the binder.

Moisture damage susceptibility is assessed using surface energy measurements and Dynamic Mechanical Analysis (DMA). Surface energy is defined as the energy needed to create a new unit surface area of material in vacuum condition. Surface energy measurements are used to compute the adhesive bond strength between the aggregates and asphalt and cohesive bond strength in the binder.

DMA testing evaluates the rate of damage accumulation in asphalt binders and mastics. The DMA apparatus applies a cyclic, torsional strain-controlled loading to cylindrical asphalt mastics until failure. DMA results are analyzed using continuum damage mechanics that focus on separating the energy expended in damaging the material from that associated with viscoelastic deformation. This report presents a new approach developed to analyze DMA results and calculate the rate of damage.

The developed approach is used to evaluate six asphalt mixtures that have performed either well or poorly in the field. The resistance of the field mixes to moisture damage is shown to be related to the calculations of bind energies and the accumulated damage in DMA.

17. Key Words	18. Distribution Statement
Moisture Damage, Surface Energy, Fracture, DMA	No restrictions. This document is available to the public through NTIS: National Technical Information Service Springfield, Virginia 22161 http://www.ntis.gov

19. Security Classif.(of this report)	20. Security Classif.(of this page)	21. No. of Pages	22. Price
Unclassified	Unclassified	172	

MEASUREMENTS OF SURFACE ENERGY AND ITS RELATIONSHIP TO MOISTURE DAMAGE

by

Robert L. Lytton
Research Engineer
Texas Transportation Institute

Eyad A. Masad
Associate Research Scientists
Texas Transportation Institute

Corey Zollinger
Graduate Assistant Research
Texas Transportation Institute

Rifat Bulut
Postdoctoral Research Associate
Texas Transportation Institute

and

Dallas Little
Research Engineer
Texas Transportation Institute

Report 0-4524-2
Project Number 0-4524
Research Project Title: Application of Surface Energy Measurements to Evaluate Moisture Susceptibility of Asphalt and Aggregates

Performed in cooperation with the
Texas Department of Transportation
and the
Federal Highway Administration

May 2005

TEXAS TRANSPORTATION INSTITUTE
The Texas A&M University System
College Station, Texas 77843-3135

DISCLAIMER

The contents of this report reflect the views of the author, who is responsible for the facts and the accuracy of the data presented herein. The contents do not necessarily reflect the official view or policies of the Texas Department of Transportation (TxDOT) or the Federal Highway Administration (FHWA). This report does not constitute a standard, specification, or regulation. The researcher in charge of the project was Robert Lytton.

ACKNOWLEDGMENTS

The author thanks Dr. German Claros, Darren Hazlett and the project advisory committee for their valuable input on various aspects of the research activities.

TABLE OF CONTENTS

Page

TABLE OF CONTENTS (Continued)

Page

LIST OF FIGURES

LIST OF FIGURES (Continued)

Figure Page

LIST OF TABLES

LIST OF TABLES (Continued)

Table Page

CHAPTER I
INTRODUCTION

Asphalt concrete is one of the primary materials used to build and maintain roadways in the world. Aggregates and asphalts are relatively cheap and abundant materials that exhibit properties such as elasticity, stability, durability, and moisture resistance when combined effectively to make hot mix asphalt (HMA) pavements.

Each year it becomes more important that these materials perform at higher levels to combat the effects of increased traffic and environmental effects. From 1990 to 2000, the United States commuting population increased from 4 million to 23.6 million. During that same time, the total roadway mileage inside the United States remained at approximately 3.95 million miles. Approximately 2.3 million of the total roadway miles are either asphalt or Portland cement concrete. In the year 1980, the United States spent a total of $41.8 billion on the highway system. Of the $41.8 billion, $20.3 billion was spent on capital expenditures and $11.4 billion was spent on maintenance. By the year 2000, the United States spent a total of $126.7 billion on the highway system. Of that total, $64.6 billion was spent on capital expenditures and $30.9 billion was spent on maintenance (*1*). As can be seen from these data, the best way to improve our roadways is not to spend more money but to improve design, construction, and maintenance of our roadways.

Many state agencies have decided that moisture damage in asphalt pavements can be reduced by developing a reliable test to predict moisture susceptibility. Moisture damage in asphalt mixes can be defined as early loss of strength and durability caused by moisture penetrating the asphalt-aggregate mixture. Moisture damage in asphalt mixes has become a prevalent problem for most departments of transportation. In 1989, Hicks conducted a survey of state departments of transportation, collecting data on moisture-related distresses (*2*). Of the states that responded, four states reported that 30 to 50 percent of pavements within the state have experienced moisture-related distress. One of these states was Arizona, which means rainfall is not the primary source of moisture causing damage to the roadways. Twelve states reported that 10 to 30 percent of pavements within the state have experienced moisture-related distress. Fifteen states reported that 1 to 10 percent of pavements within the state have experienced moisture-related distress. These

data indicate that it is becoming increasingly important to understand the mechanisms causing moisture damage and, even more importantly, to know how to measure a certain mix's susceptibility to moisture damage.

Moisture damage occurs at either the asphalt-aggregate interface (adhesive failure) or within the asphalt (cohesive failure), depending on the thickness of the asphalt. Since moisture is in our natural environment, it is able to penetrate the HMA system through air voids. Once water is in the HMA it deteriorates the aggregate-asphalt structure by entering the asphalt through absorption, which reduces the cohesive strength of the mastic and weakens the pavement's ability to resist damage due to pore pressure and premature cracking. Water is also able to penetrate to the asphalt-aggregate interface and strip the binder away from the aggregate.

This research focuses on developing an approach to evaluate the susceptibility of aggregates and asphalts to moisture damage by understanding the micro-mechanisms that influence the adhesive bond between aggregates and asphalt and the cohesive strength and durability of the asphalt. Researchers used the developed approach to evaluate six asphalt mixtures that have performed either well or poorly in the field. The results were then compared to actual reported field performance and further used to predict which combinations of asphalt and aggregate will produce superior in-service performance.

The following chapters guide the reader through the research process. Chapter II gives a brief review of literature relating to moisture damage of asphalt-aggregate mixtures, surface energy, continuum damage mechanics, and aggregate characteristics. The following chapter (Chapter III) contains a detailed description of the experimental design and equipment used in this study. Chapter IV provides the test results and analysis from each test method. In addition, Chapter IV discusses the relationship between the results and field performance. Finally, the summary of findings and the main conclusions are stated in Chapter V. Also, Chapter V includes recommendations on the selection of combinations of aggregates and asphalt in order to reduce moisture susceptibility.

CHAPTER II
LITERATURE REVIEW

OVERVIEW OF MECHANISMS CONTRIBUTING TO MOISTURE DAMAGE

Moisture damage in asphalt mixtures has been a major problem for state and federal highway agencies for many years, as is evidenced by increasing budget needs for maintenance and rehabilitation. In order to reduce these needs it is necessary understand the mechanisms that cause moisture damage and, consequently, to know how to measure an asphalt mix's susceptibility to moisture damage prior to construction.

Moisture damage can occur by deteriorating the aggregate-asphalt bond by loosening the adhesion of the asphalt from the aggregate surface, causing adhesive failure. Another mechanism of moisture damage occurs when water enters the asphalt through absorption, reducing the cohesive strength of the HMA, and causing the mixture to lose stability, termed cohesive failure. Moisture is able to penetrate the HMA system through the air voids (*3*) or by diffusion through the binder.

Researchers have identified several mechanisms by which adhesive and cohesive failures occur including displacement, detachment, pore pressure, emulsion formation, and interfacial tension (*3*-*7*).

Displacement involves separation of the asphalt from the aggregate surface through a break in the asphalt film (*3*). The break in the asphalt film can be caused by many mechanisms including incomplete coating of aggregate surface, film rupture from highly angular aggregates, or traffic and freeze-thaw cycles that stresses the pavement, causing early bleeding, rutting, or fatigue cracking. Scott presents a chemical reaction theory to describe how changes in the pH of the water at the aggregate surface alter the type of polar groups absorbed, therefore building up opposing negatively charged electrical double layers on the surfaces. This buildup attracts more water and increases the physical separation (*8*).

Detachment occurs because a thin film of water is able to penetrate to the surface of the aggregate without actually breaking the asphalt film (*7*). Consequently, water causes detachment of asphalt from the aggregate surface. Thelen (*6*) described how water reduces the adhesive bond strength between asphalt and aggregate due to interfacial tensions of the

three phases. Thelen provides data describing how asphalt spreads over water films on stone in order to decrease the free energy of the system.

Moisture damage has also been attributed to buildup of pore pressure in HMA under saturated conditions (*7*). The buildup of pore pressure causes growth of microcracks, and eventually rupture of the asphalt film (*7*). Microcracks eventually become macrocracks, increasing both cohesive and adhesive failures. Experimental evidence shows that there exists an air void range in which water is trapped in HMA (*9*).

Spontaneous emulsification occurs as an inverted emulsion of water that penetrates the asphalt film in droplets and breaks the bond between asphalt and aggregate (*3*). Fromm observed spontaneous emulsification by placing asphalt-coated slides in water (*3*). Within 24 days there was visible evidence of the surface tension of water pulling asphalt from the slide, and after seven months the emulsion had penetrated to the glass and broken the adhesive bond (*3*).

Researchers have noted that moisture damage mechanisms are complicated and often work together. There continues to be great discussion and debate as to which mechanisms dominate, how they interact, and how to measure moisture damage under the complex interactions of the mechanisms discussed above.

CONVENTIONAL METHODS FOR MEASURING MOISTURE SUSCEPTIBILITY

For many years engineers have measured moisture susceptibility of asphalt mixtures using empirical tests. These empirical tests can be broken into two categories: quantitative strength tests and subjective tests. The following is a review of some of the more conventional and widely used test procedures. During the review it is necessary to recognize that no single test method has been widely accepted because the repeatability and correlation to field performance is still unsatisfactory.

Quantitative Strength Tests

Lottman Test (NCHRP 246)

The first credible strength test was developed by Lottman (*10*) in a project for the National Cooperative Highway Research Program (NCHRP). This test established the fundamentals for most strength tests that would follow and are discussed later. Nine test

specimens (100 mm diameter and 63.5 mm high) are prepared by compaction to field air void content. The nine specimens are broken into three groups of three specimens each. The first group does not receive any conditioning and is the control group. Group 2 is vacuum saturated (13-67 kPa partial pressure) to condition the sample with water for 30 minutes. Group 3 is also vacuum saturated and then placed in a freeze cycle (-18^{o} C water bath for 15 hours) and then a thaw cycle (60^{o} C water bath for 24 hours). All specimens are tested for either resilient modulus (M_R) or indirect tensile strength (ITS). The retained tensile strength ratio (TSR) is calculated for Groups 2 and 3 as follows:

$$TSR = \frac{ITS_{Conditioned}}{ITS_{Control}} \quad (1)$$

The Group 2 TSR value is assumed to reflect moisture susceptibility up to 4 years, while Group 3 reflects moisture susceptibility from 4 to 12 years. Lottman recommended a minimum TSR value of 0.70.

Modified Lottman Test (AASHTO T283)

This method was adopted by Association of American State and Transportation Officials (AASHTO) in 1985 and implemented in the Superpave mix design procedures because of its wide acceptance by state departments of transportation (*2*, *11*). Six test specimens (100 mm diameter and 63.5 mm high) are prepared by compaction to 7 ± 0.5 percent air void content. The six specimens are broken into two groups of three specimens each. The first group does not receive any conditioning and is the control group. Group 2 is partially vacuum saturated (13-67 kPa partial pressure) to 75 ± 5 percent saturation. If the saturation is greater than 80 percent, the sample must be discarded. Group 2 is then placed in a freeze cycle (-18^{o} C water bath for 16 hours) and then a thaw cycle (60^{o} C water bath for 24 hours). All specimens are tested for ITS, and TSR is calculated as in Equation (1).

Tex-531-C Test

This test method is very similar to the Modified Lottman Test. The only change is the moisture saturation time is limited to 30 minutes. This test has been used by the Texas Department of Transportation as the primary method for measuring moisture susceptibility

of mixes. Recent research results on this test have concluded that the repeatability and reproducibility of the test are very poor, leading to a decision to discontinue the test in Texas.

Subjective Tests

Boiling Water Test (ASTM D3625)

This test method has been used primarily as a screening test for selection of possible mix designs. The method specifies adding loose HMA mix into boiling water for 10 minutes. If 95 percent of the visible area of the aggregate retains its original coating of asphalt, the mix passes the test. Strength testing is not performed.

Static-Immersion Test (AASHTO T182)

This test method has also been used primarily as a screening for selection of possible mix designs. The method specifies adding loose HMA mix into distilled water at 25 ^{o}C for 16 hours. If 95 percent of the visible area of the aggregate as viewed in water retains its original coating of asphalt, the mix passes the test. Strength testing is not performed.

Many state departments of transportation including Texas have decided to seek more fundamental approaches to predicting moisture susceptibility because of the unreliability of the empirical test methods.

FACTORS AFFECTING MOISTURE DAMAGE

Asphalt Film Thickness

Damage in asphalt mixtures can occur within the mastic (cohesive failure) or at the aggregate-mastic interface (adhesive failure). Whether a cohesive or adhesive failure occurs depends on the nature of the mastic and the thickness of the mastic around the aggregate. The mastic is considered as the pure asphalt binder plus the aggregate particles finer than .075 mm sieve. In 1968, Marek and Herrin provided experimental observations relating tensile strength of binder and failure type to film thickness (*12*). Using these data, Lytton used micromechanics to determine the relationship between binder film thickness and failure type (adhesive or cohesive) (*13*). The result of the micromechanics analysis is

shown schematically in Figure 1. For thinner film thicknesses, the adhesive tensile strength is less than cohesive tensile strength. However, at thicker film thicknesses the cohesive tensile strength is less than adhesive tensile strength (*13*). Since mastic thicknesses vary in asphalt pavements, both adhesive and cohesive failures could occur in the asphalt mix, with one of them perhaps being dominant.

Aggregate Shape Characteristics

Aggregate shape characteristics influence mechanical adhesion between the aggregate and binder. Pocius (*14*) stated that three factors contribute to mechanical adhesion: physical "lock and key," redistribution of stresses, and increased surface area. It is well established that increased aggregate texture and angularity improves mix resistance to deformation and, consequently, the relative sliding between aggregates through the binder film. As discussed later in this chapter, an important aspect of resistance to moisture damage is the bond strength per unit area within the binder and at the binder-aggregate interface. Increased aggregate texture and angularity causes increased surface area, and the result is increased total bond energy in the mix.

The influence of mechanical adhesion on resistance to deformation and moisture damage is evident in the literature and in recent work at the Texas Transportation Institute (TTI). Based on the work of McBain and Hopkins, Hicks reported that it is generally accepted that aggregates with a porous, slightly rough surface promote adhesion by providing a mechanical interlocking effect (*2, 15, 16*). A possible adverse effect of angularity on moisture damage is an increased probability of puncturing the asphalt film and allowing intrusion of water to the asphalt-aggregate surface.

In recent years, researchers have made great strides in developing methods to measure aggregate shape, texture, and form using the Aggregate Imaging System (AIMS) (*17*). Researchers can distinguish between different aspects that constitute particle geometry. Particle geometry can be fully expressed in terms of three independent properties: form, angularity (or roundness), and surface texture. Figure 2 shows a schematic diagram that illustrates the differences between these characteristics

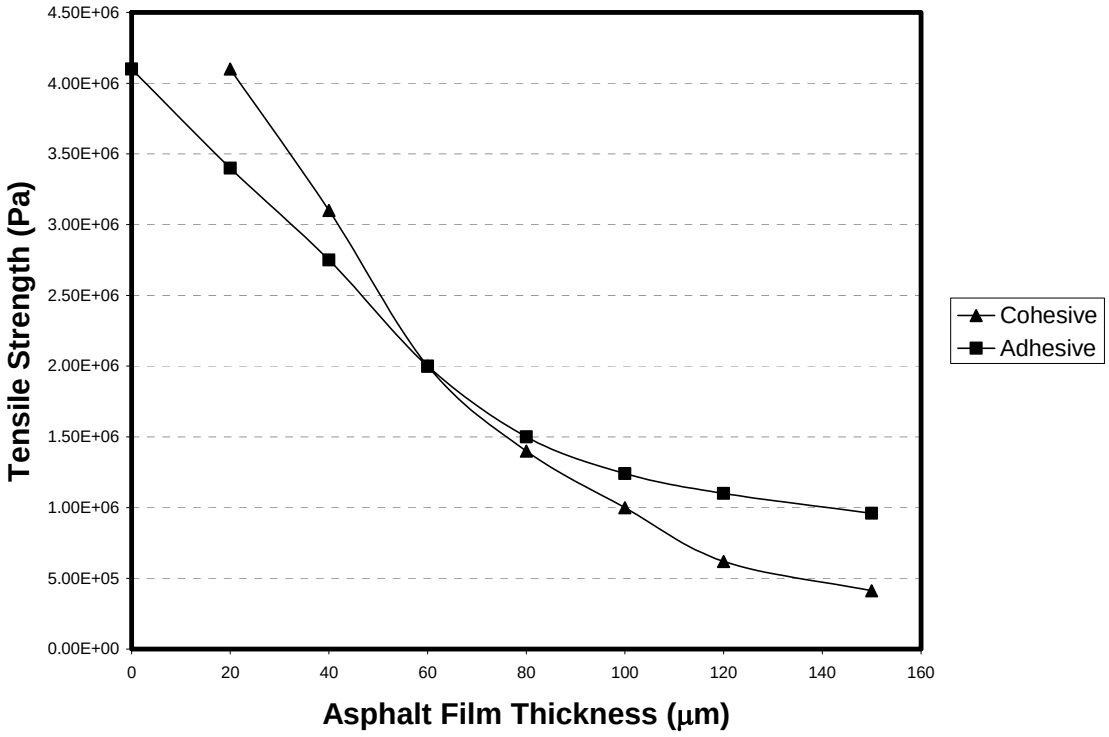

Figure 1. Tensile Strength versus Film Thickness *(13)*.

.

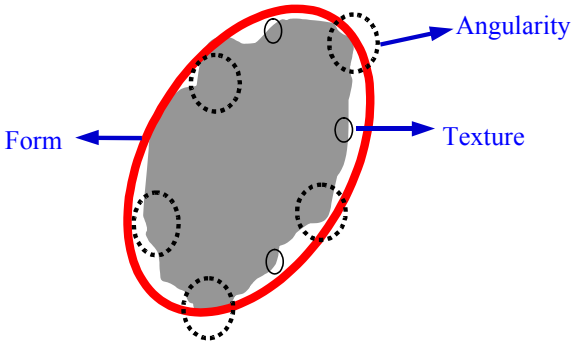

Figure 2. Components of an Aggregate Shape: Form, Angularity, and Texture *(18)*.

Form, the first-order property, reflects variations in the proportions of a particle. Angularity, the second-order property, reflects variations at the corners, that is, variations superimposed on shape. Surface texture describes the surface irregularity at a scale that is too small to affect the overall shape. These three properties can be distinguished because of their different scales with respect to particle size, and this feature can also be used to order them. Any of these characteristics can vary widely without necessarily affecting the other two characteristics.

The relationship between aggregate shape properties and HMA performance was described in detail by Masad et al. and is summarized here (*18*). Researchers tested and analyzed HMA mixes with limestone, gravel, and granite aggregates. The granite aggregate exhibited the highest texture, followed by limestone, and then gravel. HMA mixes were tested using the Asphalt Pavement Analyzer (APA) under dry conditions, the Hamburg Wheel Tracking Test (HW) under wet conditions, and the Dynamic Modulus Test (DM) under both dry and wet conditions (*18*).

In the APA test, after 8000 cycles, the average rutting for the gravel mix was 14.6 mm, while there was no significant rutting in the limestone and granite mixes. In the Hamburg test, the maximum rut depth of 12.5 mm was reached in 14,200 cycles for the granite mix, the limestone mix reached maximum depth in 5451 cycles, and the uncrushed gravel mix reached it in 1280 cycles. Dynamic modulus of mixtures for both granite and limestone aggregates was approximately 1.24×10^8 Pa in dry condition. For the wet condition, the dynamic modulus of granite was around 8.61×10^7 Pa, and it was 3.79×10^7 Pa for limestone. In addition, mixtures prepared with granite aggregate showed the highest wet/dry ratios of dynamic modulus compared to the other three aggregate mixtures.

The results suggested the performance of the granite mix is superior to the limestone mix under wet conditions, as evaluated in the HW test and the DM test. Researchers theorized that the granite retained a superior level of bonding in the presence of water compared with the limestone aggregate because of its higher texture and angularity. The granite and limestone mixes outperformed the gravel mix in both the wet and dry tests. It is interesting to note that surface energy measurements indicated that the limestone mix had higher bond than the granite. This indicates that the mechanical bond due to the high texture had significant effect on moisture damage.

Masad et al. developed a viscoplastic model for asphalt mixes at high temperature (*19*). One of the model parameters, a work-hardening parameter, $\bar{\kappa}$, represents the effect of adhesion between the binder and aggregate or cohesion within the binder on permanent deformation. In Figures 3 and 4, it is shown that the texture index of the fine fraction correlates with the initial $\bar{\kappa}$ at 1 percent viscoplastic strain, while the texture for the coarse aggregate correlates with the final $\bar{\kappa}$ at 8 percent viscoplastic strain. The coarse fraction of granite exhibits the highest texture index and, accordingly, the highest final $\bar{\kappa}$ value.

Surface Energy

The fundamental law of fracture for viscoelastic materials was proposed by Schapery in 1984 and is presented in Equation (2) (*20*). This theory states that fracture damage caused by load-induced energy is balanced by the energy stored on newly created crack faces.

$$W = E_R D(t_\alpha) J_R \qquad (2)$$

where, W is the work of adhesion (W^a) or cohesion (W^c) per unit of each crack surface area created (i.e., the minimum energy required to cause fracture). The term on the right side is termed pseudostrain energy because the energy required to overcome nonlinear and viscoelastic effects is eliminated. E_R is the reference modulus used in determining the pseudostrain energy that is available to extend the crack; $D(t_\alpha)$ is the viscoelastic creep compliance over a period t_α, the time required for a crack to move a distance equal to the length (α) of the process zone ahead of the crack tip; and the J-integral J_R, is the pseudostrain energy release rate per unit crack area from one load cycle to the next. When the pseudostrain energy released is greater than the required minimum energy for bond breakage, crack extension occurs.

Hefer et al. (*21*) provided a synthesis of research on bitumen-aggregate adhesion within the framework of theories and mechanisms established in the general field of adhesion. Hefer et al. (*21*) stated that surface energy in combination with other material properties serves as an important ingredient in performance prediction, including moisture damage.

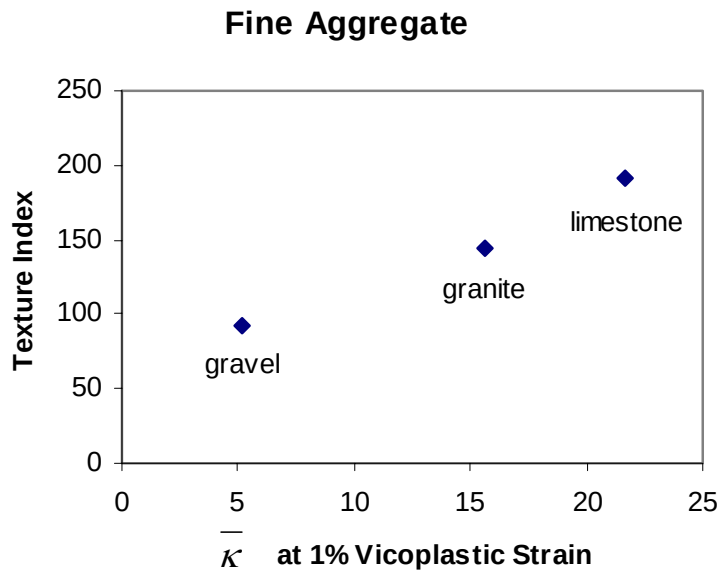

Figure 3. Relationship between the Hardening Model Parameter and Fine Aggregate Surface Texture *(19)*.

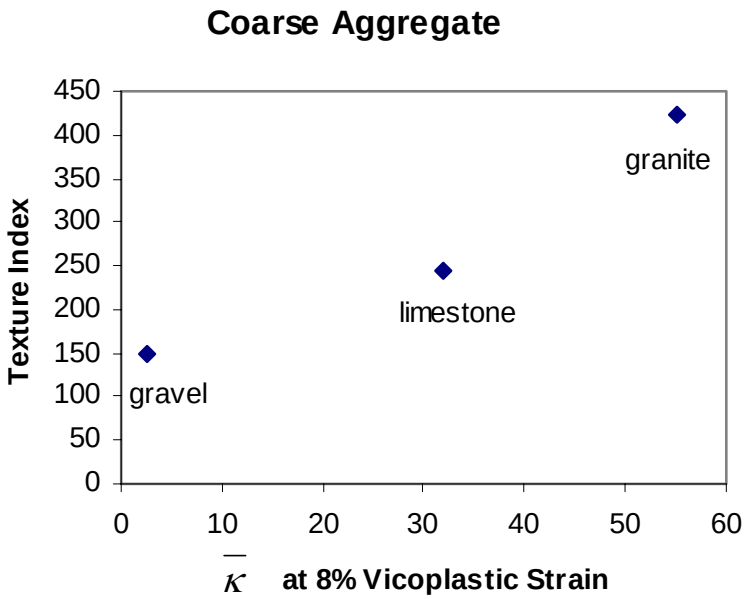

Figure 4. Relationship between the Hardening Model Parameter and Coarse Aggregate Surface Texture *(19)*.

The relationships between the Gibbs free energy, work of adhesion, and surface energy are presented below. The surface energy, γ, in a thermodynamic sense is the reversible work required to create a unit area of new surface. Although equal in magnitude, the work of adhesion (W^a) and the Gibbs free energy of adhesion (ΔG^a) should be interpreted as in Equation (3):

$$W^a = -\Delta G^a \tag{3}$$

Consider a brittle material of unit cross-sectional area subjected to a tensile force. Then, if the material is completely brittle, the work done on the sample is dissipated only through propagation of a crack, thereby creating two new surfaces. The total work expended per unit of surface area in forming the two surfaces is then equal to twice the surface energy per unit of surface area of the material under consideration. Under these conditions and for cohesive failure,

$$W^c = 2\gamma \tag{4}$$

or, $$\Delta G^c = -2\gamma \tag{5}$$

When two dissimilar materials form an interface by being in intimate contact, a tensile force can be applied to split the materials into dissimilar parts. For a completely brittle interface of unit cross-sectional area, the energy expended is the sum of the individual surface energies for the two materials involved, minus an interfacial energy *(14)*. Dupré, in 1867, postulated the following formulas for computing work of adhesion and Gibbs free energy of adhesion between two materials:

$$W^a = \gamma_i + \gamma_j - \gamma_{ij} \tag{6}$$

or, $$\Delta G^a = \gamma_{ij} - \gamma_i - \gamma_j \tag{7}$$

where, γ_i is the surface energy of the i_{th} material and γ_{ij} is the interfacial energy between the two materials in contact.

Following the form suggested by Fowkes *(22)*, the surface energy of a single phase is given by,

$$\gamma_i = \gamma_i^{LW} + \gamma_i^{AB} \tag{8}$$

where, LW denotes Lifshitz-van der Waals, and AB denotes acid-base.

It follows that the free energy of cohesion and adhesion likewise constitutes two components. Therefore, the Gibbs free energy of cohesion is,

$$\Delta G_i^{\,c} = -2\gamma_i = \Delta G_i^{\,cLW} + \Delta G_i^{\,cAB} \tag{9}$$

and the Gibbs free energy of adhesion is,

$$\Delta G_{ij}^{\,a} = \gamma_{ij} - \gamma_i - \gamma_i = \Delta G_{ij}^{\,aLW} + \Delta G_{ij}^{\,aAB} \tag{10}$$

The van der Waals forces represent the interaction between two symmetric molecules. For the LW component, the Berthelot geometric mean rule therefore holds,

$$\Delta G_{ij}^{\,aLW} = -2\sqrt{\gamma_i^{\,LW}\gamma_j^{\,LW}} \tag{11}$$

The AB component cannot be treated the same and was derived empirically by Van Oss et al. (*23*),

$$\Delta G_{ij}^{\,aAB} = -2\left(\sqrt{\gamma_i^{\,+}\gamma_j^{\,-}} + \sqrt{\gamma_i^{\,-}\gamma_j^{\,+}}\right) \tag{12}$$

Van Oss and his co-workers presented the full version of the Young-Dupré equation by inserting ΔG^{LW} and ΔG^{AB},

$$-\Delta G^{a} = W^{a} = \gamma_L^{\,Tot}\left[1+\cos(\theta)\right] = 2\left(\sqrt{\gamma_L^{\,LW}\gamma_S^{\,LW}} + \sqrt{\gamma_L^{\,+}\gamma_S^{\,-}} + \sqrt{\gamma_L^{\,-}\gamma_S^{\,+}}\right) \tag{13}$$

where, L represents the liquid and S the solid under consideration. Equation (13) solves for three unknown surface energy components if the contact angles of three liquids with different and known polarities are measured on the unknown surface. These polarities have been defined as monopolar basic, monopolar acidic, bipolar (basic and acidic), or apolar (only van der Waals forces).

An important practical application of this theory is that it can be used to predict the work of adhesion between two materials such as asphalt and aggregate, if their surface energy components are known. Similarly, the work of cohesion can be predicted within the asphalt. By adapting the Dupré equation, the adhesive bond energy between asphalt and aggregate in the presence of water is:

$$\Delta G_{ikj} = \gamma_{ij} - \gamma_{ik} - \gamma_{jk} \tag{14}$$

where, subscript i refers to asphalt, j refers to aggregate, and k refers to water. With the components of the free energy of interfacial interaction additive, the adhesive bond energy is computed as:

$$\Delta G_{ikj}^{a} = \Delta G_{ikj}^{aLW} + \Delta G_{ikj}^{aAB} \tag{15}$$

Van Oss and coworkers (*23, 24*) proposed the following complete formula to compute the adhesive bond energy between asphalt and aggregate in the presence of water:

$$\Delta G_{ikj}^{a} = 2\left[\begin{array}{l}\sqrt{\gamma_i^{LW}\gamma_k^{LW}} + \sqrt{\gamma_j^{LW}\gamma_k^{LW}} - \sqrt{\gamma_i^{LW}\gamma_j^{LW}} - \gamma_k^{LW} + \\ \sqrt{\gamma_k^{+}}\left(\sqrt{\gamma_i^{-}} + \sqrt{\gamma_j^{-}} - \sqrt{\gamma_k^{-}}\right) + \\ \sqrt{\gamma_k^{-}}\left(\sqrt{\gamma_i^{+}} + \sqrt{\gamma_j^{+}} - \sqrt{\gamma_k^{+}}\right) - \sqrt{\gamma_i^{+}\gamma_j^{-}} - \sqrt{\gamma_i^{-}\gamma_j^{+}}\end{array}\right] \quad (16)$$

When the liquid is water, this interaction is called the "hydrophobic interaction" where the adhesive bond strength is less than zero. This indicates the interaction between aggregate and asphalt becomes repulsion, which is the driving force for water to displace asphalt from the aggregate surface (*23*).

Thermodynamic concepts have been used by many researchers to describe adhesion between bitumen and aggregate materials. Lytton (*13*) utilized surface energies measured on bitumen and aggregate surfaces to calculate free energies of adhesion and cohesion by applying modern surface energy theories. Surface energy has played an important role in discovering the rules governing microfracture and healing in bitumen-aggregate mixtures (*25*). Resistance to fracture increase has been correlated to total dewetting or fracture bond energy increase. Healing potential is enhanced by increasing the acid-base component of the wetting bond energy. On the other hand, the LW component of the wetting bond energy affects healing negatively, as described by Cheng et al. (*26*).

Water increases the asphalt's ability to heal (an increase in the acid-base component) and reduces its resistance to fracture (a decrease in the total fracture bond energy). As explained by Cheng et al. (*26*), this phenomenon occurs because the hydrogen atoms in the water have good interaction or affinity with those of the AB component of the asphalt; hence, water makes the hydrogen bonds stronger and enhances the healing capability. This phenomenon reinforces the fact that it is beneficial to have a greater AB component and a lower LW component. However, the bonding of these hydrogen atoms takes time and therefore it is associated with long-term healing of asphalt (*24*). More detailed literature review on the theory of surface energy and factors that influence its measurement are available in Appendix A.

Air Void Distribution and Permeability

It has been long recognized that water permeability is an important factor influencing moisture damage. Many researchers have assumed that a proportional relationship exists between HMA permeability and moisture damage. The relationship between HMA moisture damage, air void structure, and pore pressure was investigated by Castelblanco et al. (*9*). The study involved two mixes with two different aggregate types, limestone and granite. Each mix had varying gradations in order to produce varying air void distributions among specimens. All mixes were designed to meet the Superpave volumetric requirements, and specimens were compacted to 7 percent target percent air voids.

The wet and dry samples were subjected to the Superpave^{TM} indirect tension test to induce damage. The parameter to quantify moisture damage was the number of cycles to failure, N_f, required to grow a crack 25.4 mm wide (*9*).

Air void distribution was analyzed using the X-ray computed tomography (X-ray CT) imaging technique (*27*). Researchers found different air void sizes within the same mix type due to the different aggregate gradations, and the granite mixes had in general larger air voids than their limestone counterparts (*9*). Examples of the results of air void distributions in limestone and granite mixes with the same gradations are shown in Figure 5.

Researchers determined that there is an average diameter size or a "pessimum size" at which moisture damage is maximum. Researchers suggested that small air void sizes reduce infiltration of water to the mix, while large air voids make it easier for the water to drain out of the mix. Hence, good resistance to moisture damage is obtained at these two levels of air void sizes. At the pessimum air void size, water gets into the mix and it is difficult to drain it out, leading to more moisture damage. This pessimum air void size depends on the type of the mix; for the granite mix it was ranged between 1.2 and 1.4 mm, and it ranged from 0.8 to 1.0 mm for the limestone mix (*9*). The relationships between air void size distributions and moisture damage for the limestone and granite mixes are shown in Figure 6. The y-axis is the ratio of number of cycles to failure for moisture-conditioned specimens divided by the number of cycles to failure for dry specimens.

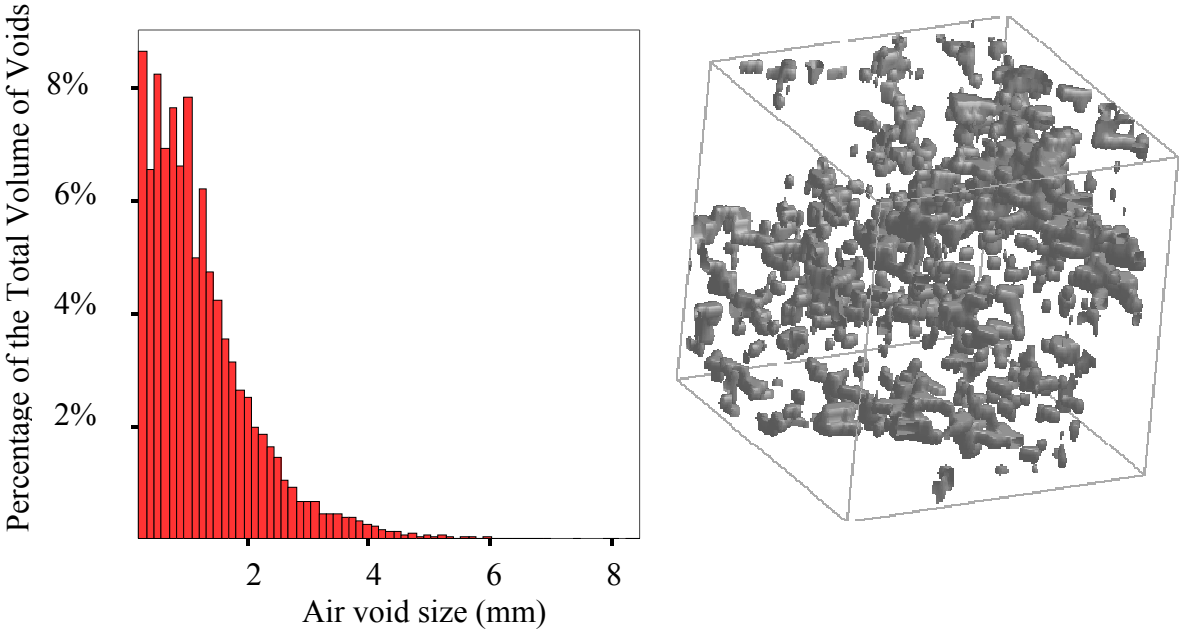

(a)

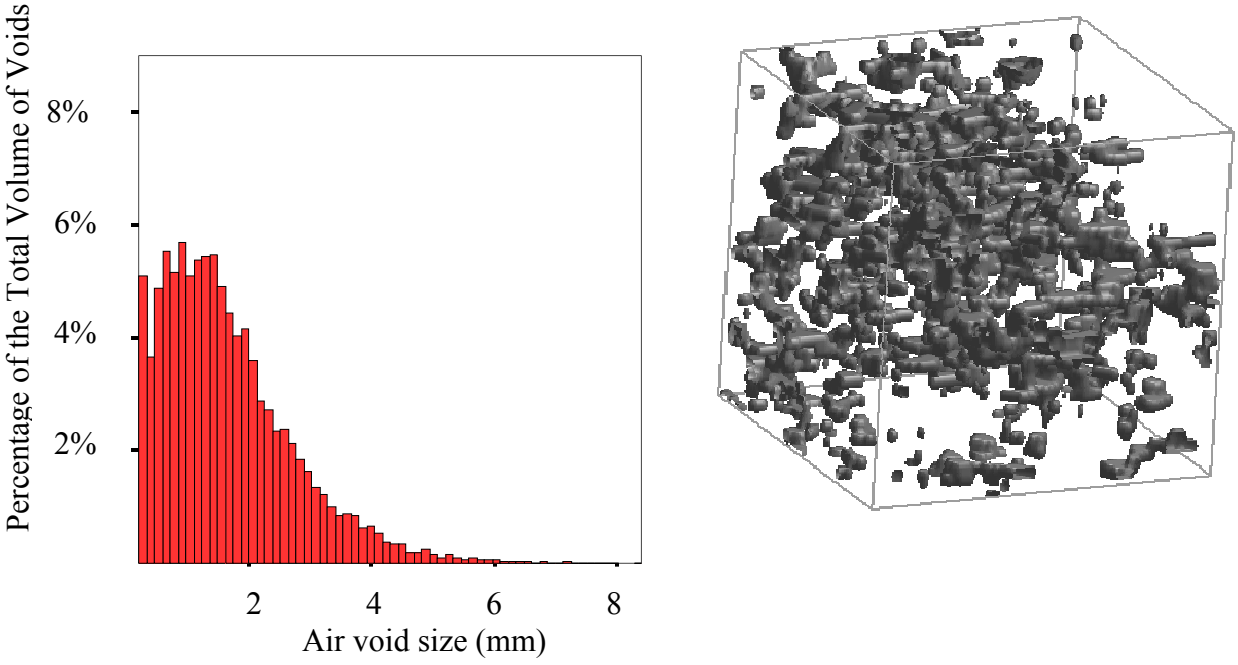

(b)

Figure 5. Distributions and Three Dimensional Visualization of Air Voids: (a) Limestone and (b) Granite (9).

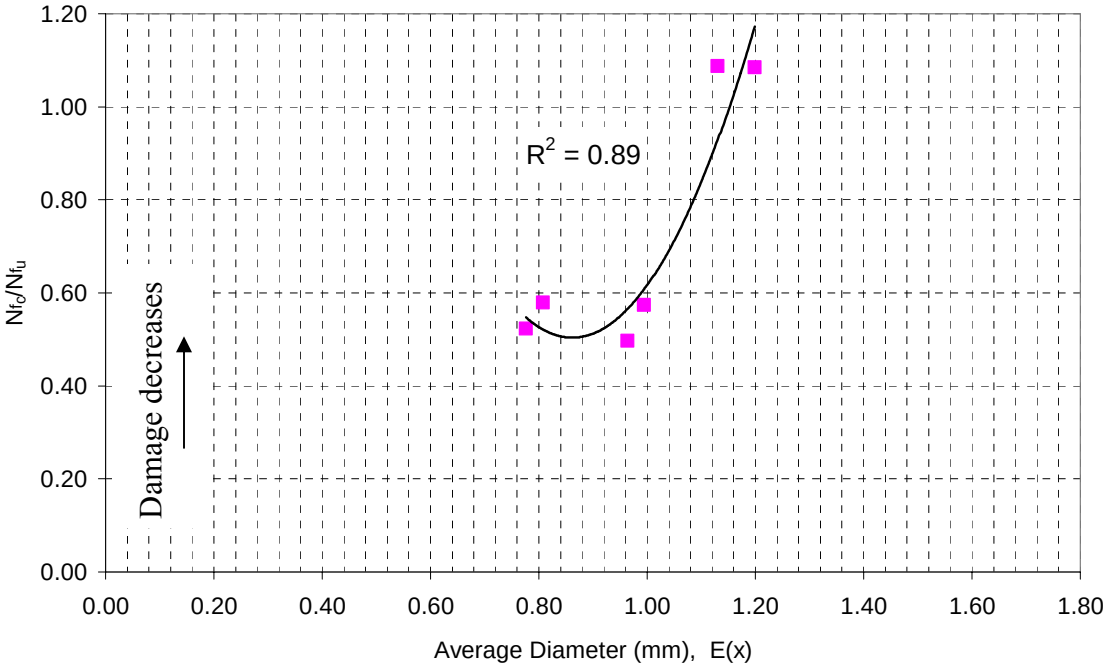

(a)

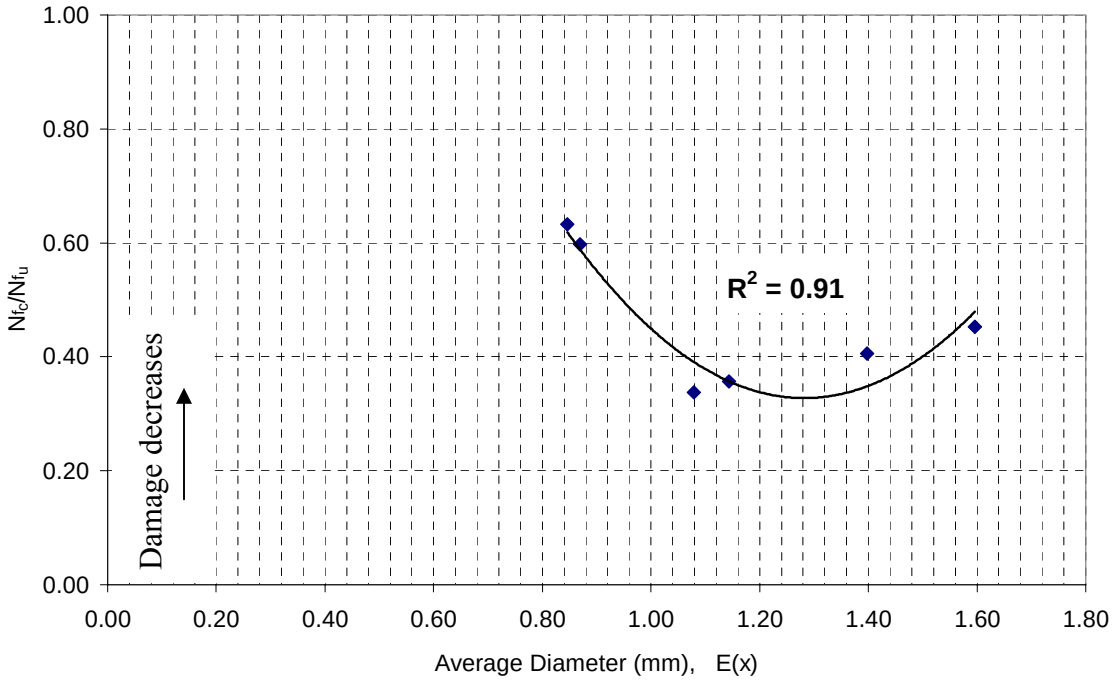

(b)

Figure 6. N_f Ratio and Average Diameter: (a) Limestone and (b) Granite *(9)*.

ANALYSIS METHODS OF MOISTURE DAMAGE

Empirical Parameters

Moisture damage in asphalt mixes causes a reduction in the fatigue life. Therefore, moisture damage can be assessed by the reduction in fatigue life due to moisture conditioning. The point of fatigue failure has been a controversial topic. Some researchers have suggested a 50 percent reduction in modulus (*28*). Other researchers suggest changes in dissipated energy per loading cycle or the accumulated dissipated energy (*29, 30*). Reese argues that the point at maximum phase angle versus time is a good indication of fatigue failure because the phase angle curve shows a rapid decrease at the same point the mixture stops accumulating distress, as illustrated in Figure 7 (*31*).

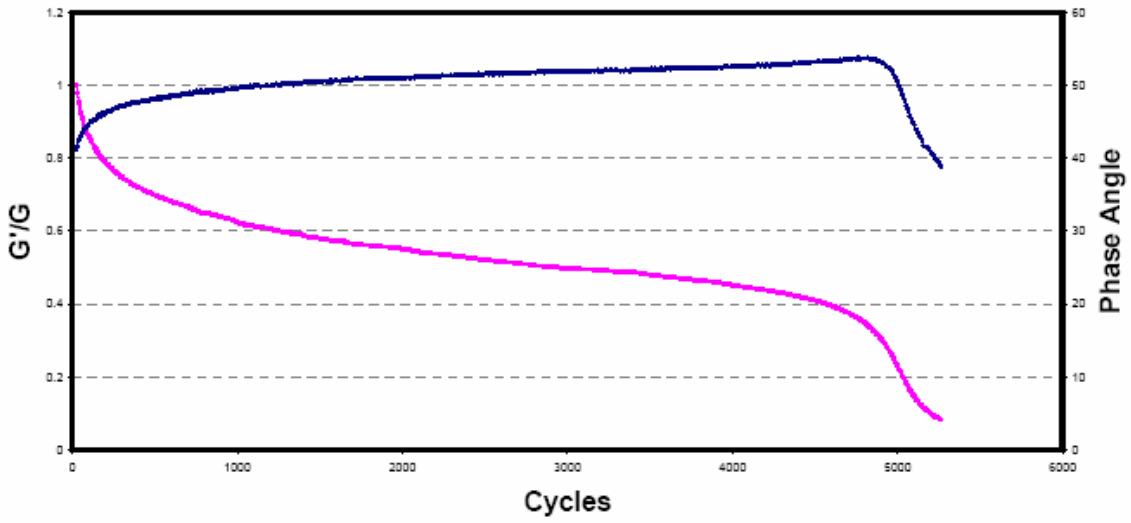

Figure 7. Plot of Modulus and Phase Angle versus Number of Cycles.

One potential fatigue failure point is determined by plotting G*n versus n and computing the maximum value as suggested by Rowe and Bouldin and illustrated in Figure 8 (*30*). During controlled-strain fatigue testing, the stiffness decreases with time, typically showing two inflection points and a transition point as shown by Rowe and Bouldin and illustrated in Figure 8 (*30*). Cross-plots and error analyses demonstrate the transition point as a reasonable estimate of the fatigue life (*32*).

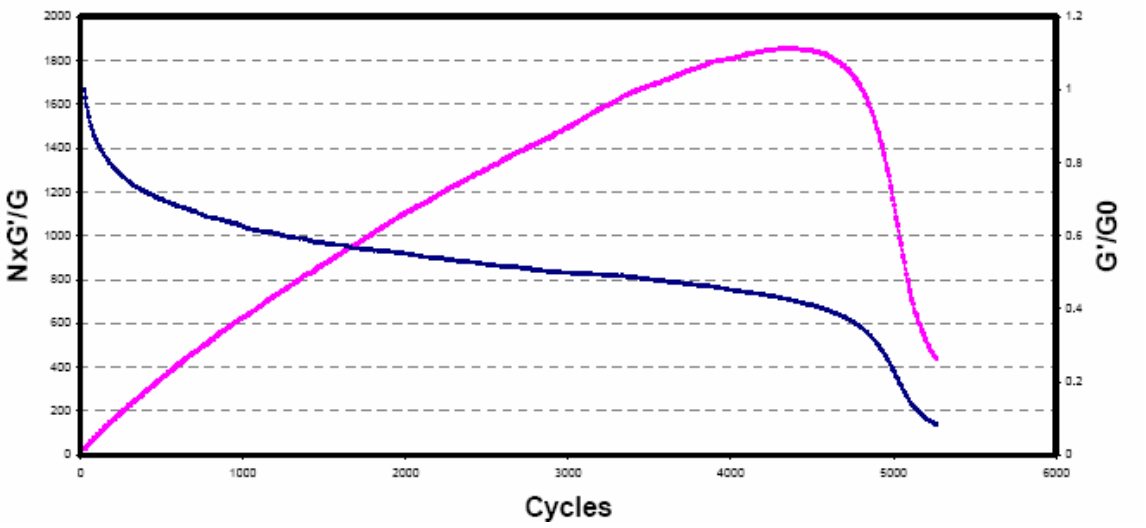

Figure 8. Plot of Modulus and N × G'/G versus Number of Cycles.

Continuum Damage Mechanics Approach

Continuum damage mechanics has been used to analyze the results of dynamic testing of asphalt binders and mastics using the dynamic mechanical analyzer (DMA). The DMA applies a cyclic, torsional strain-controlled loading to cylindrical asphalt mastics until failure. Kim et al. demonstrated that the rate of damage and the amount of damage various mastics can accumulate before failure depends on the nature of the mastic (*33*). This is very important because well-designed mastics will tolerate more damage to failure than those that are not. The nature of the mastic can be changed by the type and amount of filler added to the binder and by polymer modification. Kim et al. showed that unfilled binders and nonmodified binders accumulated less damage than filled binders and modified binders. This result provides data supporting the mastic nature's ability to affect moisture susceptibility for the entire mix and control the type of failure (adhesive or cohesive) that will occur.

The samples tested using the DMA are cylindrical shaped, 50 mm long (L), and a constant 12 mm radius (R). Kim provides a complete analysis method that will be referred to and described below (*32*). The samples are subjected to torsional loading with torque (T) to a constant angle of twist (φ). The analytical harmonic representation of the twisting displacement at time (t) under the zero mean cyclic displacement condition is expressed in sinusoidal form:

$$\varphi(t) = \varphi_0 \sin(\omega t) H(t) \tag{17}$$

where, φ_0 is the twisting amplitude, ω is the angular velocity, and H(t) is the heaviside step function. The angular velocity is computed by Equation (18), where f is the loading frequency.

$$\omega = 2\pi f \tag{18}$$

The corresponding oscillatory shear strain history at time (t) is:

$$\gamma(t) = \gamma_O \sin(\omega t) H(t) \tag{19}$$

and $$\gamma_o = \frac{\varphi r}{L} \tag{20}$$

where, γ_o is the shear strain amplitude. If the samples exhibit linear viscoelastic behavior, the corresponding shear stress due to the oscillatory shear strain is:

$$\tau(t) = \gamma_o \left|G^*(\omega)\right| \sin(\omega t + \phi) \tag{21}$$

where, $\left|G^*(\omega)\right|$ is the linear viscoelastic dynamic modulus in shear and ϕ is the linear viscoelastic phase angle.

As discussed previously, Schapery proposed the extended elastic-viscoelastic correspondence principle, which applies to both linear and nonlinear viscoelastic materials (*20*). This concept allows the use of pseudo variables to represent damage of viscoelastic materials. Applying this concept to strain, pseudostrain allows elimination of viscoelastic time dependency, not associated with damage, to be eliminated so additional material damage can be measured. When DMA specimens are subjected to oscillation, damage occurs and hysteretic loops exist when plotting measured stress and pseudostrain. Using Equation (21), pseudostrain is computed as following:

$$\gamma^R(t) = \frac{1}{E_R}\left[\gamma_o \left|G^*(\omega)\right| \sin(\omega t + \phi)\right] \tag{22}$$

where, E_R is the reference modulus.

One parameter used by previous researchers to assess damage is pseudostiffness (C) (*32*). Pseudostiffness is computed as follows:

$$C = \frac{\tau_N}{\gamma_N^R} \tag{23}$$

where γ^R_N is the maximum pseudostrain, and τ_N is the corresponding stress.

Using DMA testing, damage to fatigue life can be analyzed using continuum damage mechanics based on the pseudostrain concept previously discussed. Song et al. provided a comprehensive evaluation of damage in asphalt mastics using continuum mechanics and micromechanics, which is referenced and discussed below (*34*). A continuum damage parameter (*S*) was defined by Kim et al. (*35*), who applied the approach developed by Kim et al. (*36*), to DMA analysis. The following equations describe the development of the damage parameter *S*:

$$\tau_N = IC(S)\gamma_N^R \tag{24}$$

$$W_N^R = \frac{I}{2}C(S)(\gamma_N^R)^2 \tag{25}$$

where *I* is the initial pseudostiffness, W_N^R is the maximum value of the pseudostrain energy density function in the Nth cycle, γ_N^R is peak pseudostrain in the Nth cycle, *C(S)* is a damage function, and τ_N is the physical stress corresponding to γ_N^R. The continuum damage function is expressed as a function of *S*:

$$\frac{dC}{dS} = \frac{dC}{dt}\frac{dt}{dS} \tag{26}$$

$$\frac{dS}{dt} = \left[-\frac{I}{2}\frac{dC}{dS}(\gamma_N^R)^2\right]^{\alpha} \tag{27}$$

Substituting Equation (26) into Equation (27) yields:

$$\frac{dS}{dt} = \left[-\frac{I}{2}\frac{dC}{dt}(\gamma_N^R)^2\right]^{\alpha/(1+\alpha)} \tag{28}$$

Finally, the equation is rearranged by means of integration.

$$S \cong \sum_{i=1}^{N}\left[\frac{I}{2}\left(\gamma_{N,i}^R\right)^2\left(C_{i-1} - C_i\right)\right]^{a/(1-a)}(t_i - t_{i-1})^{1/(1+a)} \tag{29}$$

where, S is the damage parameter at each discrete cycle, C_i is the pseudostiffness, and t_i is the corresponding time. The material constant α is initially assumed and then varied until cross plotting the measured C against *S* at several different load levels results in closure.

The second parameter used to quantify damage is dissipated pseudostrain energy (DPSE) or Wr, which is the area within the hysteresis loop in the stress-pseudostrain domain. An illustration of the viscoelastic hysteresis behavior resulting from DMA fatigue

tests in a given cycle is shown in Figure 9. The cumulative dissipated pseudostrain energy (CDPSE) has also been used as a parameter describing damage accumulation in the DMA test.

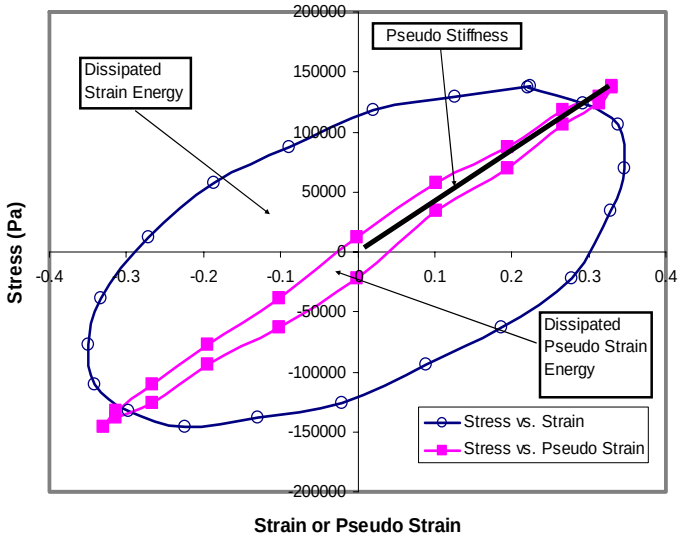

Figure 9. Illustration of the Viscoelastic Hysteresis Behavior from DMA (37).

Song et al. used X-ray CT as a tool to capture the internal structure of wet and dry DMA specimens at four steps during the fatigue test, in order to measure damage. Step 1 represents the initial condition where no damage had occurred. Step 2 is at the first inflection point (FIP) in the curve. Step 3 is at the second inflection point (SIP). Step 4 represents a point beyond the failure point. The X-ray CT images were analyzed to calculate the air void and crack areas as a function of the position ratio and used to compute the damage parameter, $\overline{\xi}$ (*34*).

Some of the experimental results are presented by Song et al. for dry specimens without rest periods, dry specimens with rest periods, and wet specimens without rest periods (*34*). Figures 10 and 11 show the results of the damage parameter ξ at different loading steps. The height ratio is defined as the ratio of vertical distance from the top of the specimen to the center of the specimen. It is convenient to use the specimen height ratio rather than the actual distance due to the slight differences in heights among the DMA specimens.

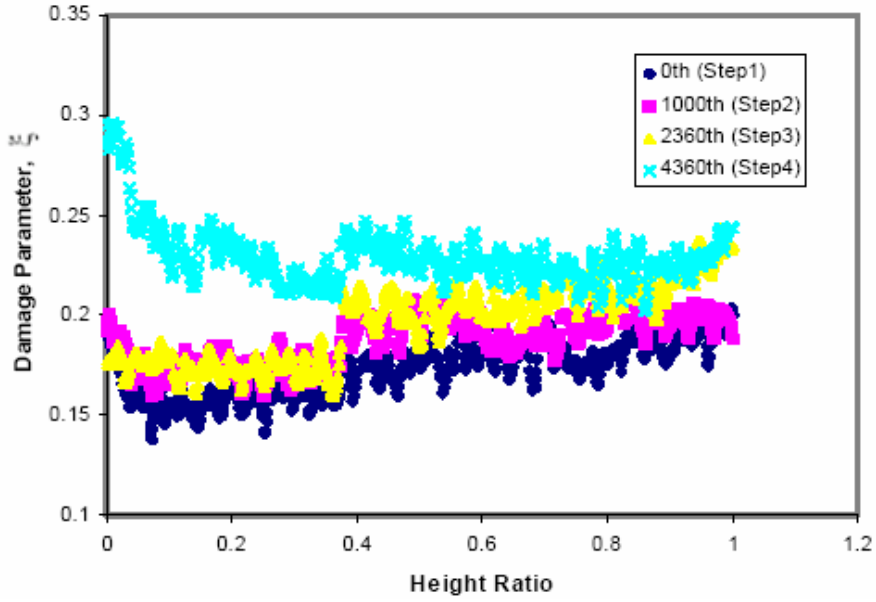

Figure 10. Damage Parameter ξ Distribution for Dry Condition without Rest Periods *(34)*.

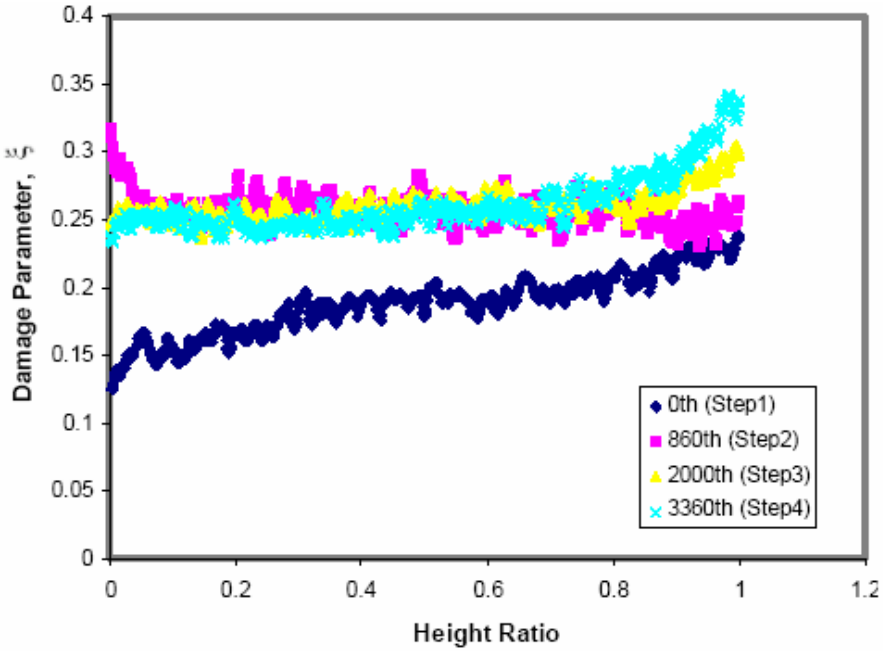

Figure 11. Damage Parameter ξ Distribution for Wet Condition without Rest Periods *(34)*.

Figure 10 shows that significant change in ξ occurred between Step 3 and Step 4 for the dry condition without rest periods. Figure 11 shows that the change in ξ for the wet specimens occurred primarily between Steps 1 and 2, while slight changes occurred between Step 2 and Step 4. These results indicate that damage occurred earlier in wet specimens compared to dry specimens.

DPSE was calculated by determining the area within the hysteresis loop at each cycle. Then the CDPSE was calculated. As shown in Figure 12, the dry specimens experienced higher CDPSE than wet specimens. This indicates that the dry specimens can sustain more damage prior to failure compared to wet specimens. As was shown by the *S* value, the CDPSE clearly shows the benefits of rest periods in promoting healing and the ability to accommodate more cumulative energy prior to failure.

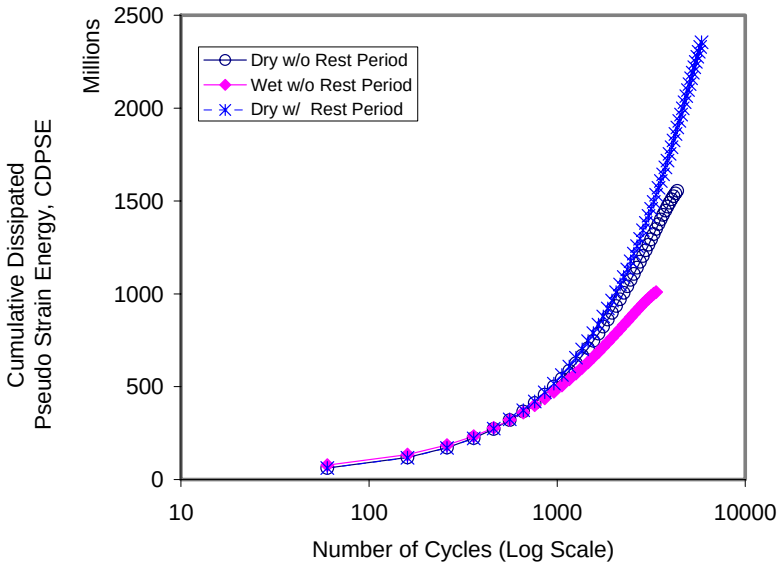

Figure 12. Changes in the Cumulative Dissipated Pseudostrain Energy (*34*).

Micromechanics Approach

Lytton (*13*) developed Equations (30) and (31) which relate the damaged modulus to an undamaged modulus of binder or mastic. These equations are based on setting the energy in the damaged material (composed of an undamaged phase with modulus equal to

G and cracks) equal to an equivalent material with modulus equal to G' (where modulus G' represents a transformed, equivalent section but without cracks). It is assumed here that reduction in mastic modulus follows the same pattern as that of the binder. Lytton (*13*) derived equations for both stress-controlled and strain-controlled modes. Since DMA testing is conducted in the strain-controlled mode, only the equations developed for strain-controlled are presented here:

Cohesive:

$$\frac{G'}{G} = \left[1 - 2\pi^2 \left(\frac{m}{A}\right)\frac{\bar{r}^3}{t}\left(1 - \frac{G\Delta G_f^c}{\pi\tau^2 \bar{r}}\right)\right] = \left[1 - 2\pi\xi\frac{\bar{r}}{t}\left(1 - \frac{G\Delta G_f^c}{\pi\tau^2 \bar{r}}\right)\right] \quad (30)$$

Adhesive:

$$\frac{G'}{G} = \left\{1 - \pi^2 \left(\frac{m}{A}\right)\frac{\bar{r}^3}{t}\left[\left(1 + \frac{G}{G_s}\right) - \frac{4G_f\left(\Delta G^a\right)}{\pi\tau^2 \bar{r}}\right]\right\} = \left\{1 - \pi\xi\frac{\bar{r}}{t}\left[\left(1 + \frac{G}{G_s}\right) - \frac{4G_f\left(\Delta G^a\right)}{\pi\tau^2 \bar{r}}\right]\right\} \quad (31)$$

where, $\bar{t}$ is the average asphalt film thickness, A is the cross-sectional area of the material, m is the number of voids, $\bar{r}$ is the average void radius, G is the binder undamaged modulus, G_s is the solid or aggregate undamaged modulus, τ is the applied shear modulus, ΔG^c is the cohesive bond energy, ΔG^a is the adhesive bond energy, and $\bar{\xi}$ is the damage parameter, which is the volume of voids (air voids and cracks) divided by the total volume. The subscript, f, indicates that the bond energy is associated with the fluid (asphalt binder). The bar ($\bar{}$) indicates that the parameter is averaged for the whole specimen. The right side of the above equations is equal to one minus the energy released by introducing m number of cracks with an average radius equal to $\bar{r}$. Also, these equations can be used for elastic materials or viscoelastic materials at a given frequency, where G* replaces G for a viscoelastic material. Figure 13 shows the comparison of measured and calculated normalized shear moduli in the dry and wet conditions (*34*).

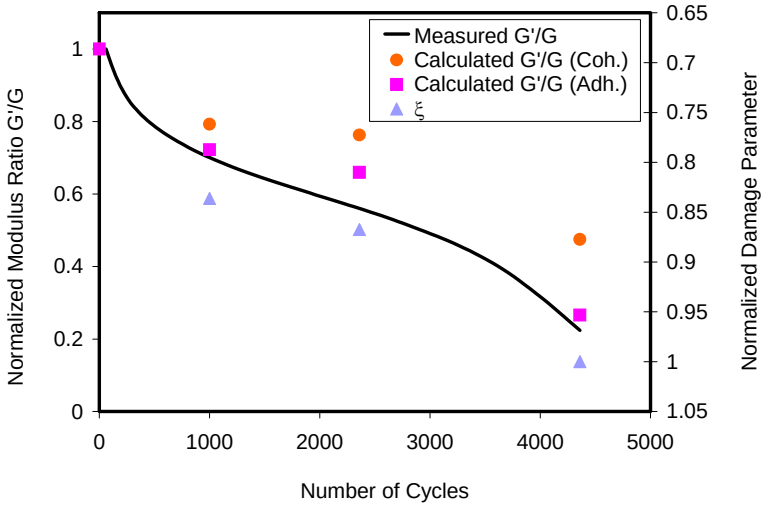

(a)

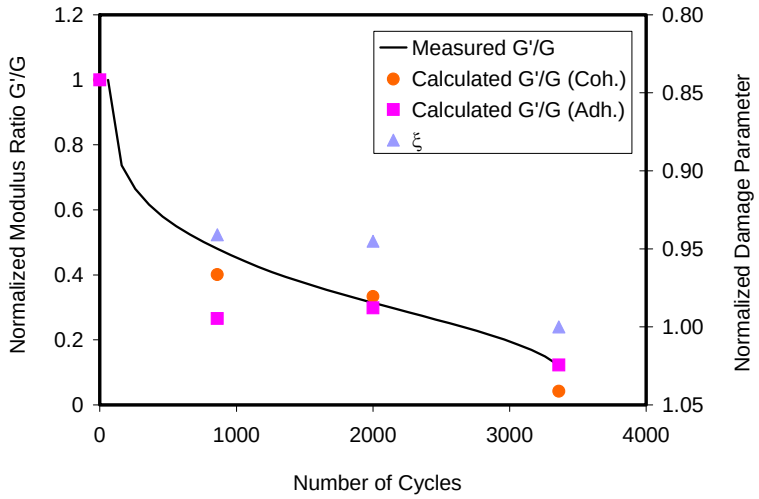

(b)

Figure 13. Comparison of Measured and Calculated Normalized Shear Moduli in (a) Dry Condition and (b) Wet Condition (*34*).

CHAPTER III
MATERIALS AND EXPERIMENTAL DESIGN

INTRODUCTION

The strategy undertaken to validate the application of surface energy measurements and dynamic mechanical analysis to evaluate moisture susceptibility was to identify asphalt mixtures with known field performance (good or poor) and to determine the relationship of laboratory measurements to performance. In cooperation with the Texas Department of Transportation (TxDOT) and the Ohio Department of Transportation (ODOT), six asphalt mixtures were identified with known field performance. In addition, two more mixtures with pre-construction laboratory measurements were included in this study. Aggregates and binders were collected by each agency and provided to TTI. Researchers tested these materials to determine fundamental material properties such as surface energy, dynamic modulus, and pseudostrain energy under dynamic loading.

MIXTURE DESCRIPTIONS

The eight mixtures selected represent varying mixture designs, geological origins of aggregates, and binder grades. Table 1 includes a summary of these mixtures, while Appendix B provides the detailed aggregate gradations.

Mixtures 1 and 2 are composed of the same aggregates. About 88 percent of the aggregate blend by weight is granite. The remaining portion is limestone mineral filler, fibers, and lime. The binder grade is PG 76-22 for both mixtures, but the binders were from two different sources. Mixture 1 was constructed on Texas FM 369 near Wichita Falls, Texas. Prior to construction, Mixture 2 was designed and the Hamburg test was performed. However, this mixture experienced significant rutting and did not meet TxDOT requirements. Consequently, the binder source was changed and the new

Table 1. Mixture Descriptions.

Mix #	Highway	Mix Description	Location	Reported Field Moisture Performance	Aggregate Type	Binder Grade
1	Texas FM 369	Stone Matrix Asphalt (SMA)	Wichita Falls, TX	Hamburg Data Only	Granite	PG 76-22
2	Texas FM 369	SMA	Wichita Falls, TX	Hamburg Data Only	Granite	PG 76-22
3	Texas IH 20 (Test Section 3)	SuperPave	Atlanta, TX	Good	Quartzite	PG 76-22
4	Texas IH 20 (Test Section 2)	SuperPave	Atlanta, TX	Good	Sandstone	PG 76-22
5	Texas IH 20 (Test Section 1)	SuperPave	Atlanta, TX	Good	River Gravel	PG 76-22
6	Texas IH 30	TY C	Atlanta, TX	Poor	Sandstone	PG 76-22
7	Ohio SR 511	TY 1	Ashland County, OH	Poor	Gravel, Limestone, Reclaimed Asphalt Pavement (Rap)	PG 64-22
8	Ohio SR 226	TY 1 Intermediate	Wayne County, OH	Poor	Gravel, Rap	PG 64-28

mixture (Mixture 1) met the requirements. Mixture 1 was designated as a good performer by TxDOT, and Mixture 2 was designated a poor performer by TxDOT.

Mixtures 3, 4, and 5 are from nine test sections constructed by the TxDOT Atlanta District on IH-20 in Harrison County. All three mixtures were designed following current Superpave mixture design procedures. Mixture 3 includes 89 percent quartzite, 10 percent igneous screenings, and 1 percent hydrated lime. Mixture 4 consists of 91 percent sandstone, 8 percent igneous screenings, and 1 percent hydrated lime. Mixture 5 consists of 67 percent siliceous river gravel, 32 percent limestone screenings, and 1 percent hydrated lime. The binder grade for all 3 mixtures is PG 76-22. Several agencies participated in both field and laboratory testing and data collection. Different field and laboratory tests were performed before, during, and after construction. Based on the test results and analysis, all three surface mixtures exhibited overall good performance in all of the tests performed. In most cases, their measured properties were numerically similar (*38*). These sections did not exhibit evidence of moisture damage.

Mixture 6 was constructed on Interstate 30 in the TxDOT Atlanta District. The aggregates in Mixture 6 are from the same source as Mixture 4, except it does not use igneous screenings. Mixture 6 uses 87 percent sandstone, 12 percent quartz local field sand, and 1 percent hydrated lime. Of the 87 percent sandstone, 28 percent is sandstone screenings. The binder grade for Mixture 6 is PG 76-22. This mixture was designated as a poor performer in terms of moisture damage in the field. The field performance was described by Mr. Miles Garrison, District Materials Engineer, TxDOT Atlanta District in a personal communication: "Maybe six months to a year of age cores taken from the location, some of the lower 50 mm asphalt concrete pavement (ACP) did not come out intact. The cores that did come whole one could almost pull apart by hand. Asphalt turned loose of aggregate. Classic areas on the aggregate looked as if asphalt had never been in contact with the aggregate. After milling down to the concrete, water could be seen flowing into the milled area from the adjacent ACP. Heavy wheel loads were

ejecting fines at intermittent locations along the longitudinal joint between outside traffic lane and shoulder *(39)*."

Mixture 7 was constructed in Ashland County, Ohio, on SR 511. Mixture 7 includes 32 percent limestone, 22 percent gravel, 26 percent natural sand, and 20 percent reclaimed asphalt pavement (RAP). During the laboratory testing, the RAP material was replaced and apportioned with the other aggregates in the mixture according to the job mix formula (JMF). The binder grade for Mixture 7 is PG 64-22.

Mixture 8 was constructed in Wayne County, Ohio, on SR 226. Mixture 8 consists of 52 percent gravel, 14 percent limestone sand, 14 percent natural sand, and 20 percent RAP. During the laboratory testing, the RAP material was replaced and apportioned with the other aggregates in the mixture according to the JMF.

Mixture 8 is a conventional mixture design used in Ohio for many years; however, it has experienced moisture damage with the gravel being suspected as the main problem. In response to this, ODOT has developed new mixture designs implementing more limestone. The field performance of these mixtures was described by a pavement performance report provided by ODOT: "Districts start looking to overlay when the Pavement Condition Rating (PCR) is low 60s to high 50s. Typically, before an overlay is needed, we get about 10-12 years with the 100 percent limestone mixtures, 7-8 years with the 100 percent gravel mixtures (Mixture 8), and it is still premature to tell about the 50/50 mixtures (Mixture 7), but the PCR data looks like they are holding up a little bit better." The PCR for Mixture 7 dropped from 95 to 89 from year 2000 to 2004, while the PCR for Mixture 8 dropped from 97 to 60 from year 1998 to 2004. Mixtures 7 and 8 are both designated as poor performers; however, Mixture 8 is considered to be even worse than 7. Mixture 7 is considered poor because of the existence of the gravel. The pavement performance summary report details more of the past history with these types of mixture designs in Ohio: "The pavement system with gravel aggregates showed the most problems, with cracking the most predominant problem. The cracking seen was typically extensive with many different types of cracking present. Those types of cracks that predominate are reflective due to base

failure, reflective due to previous overlay cracks, widening cracks, top down wheel track cracks and moisture damage/age induced cracks. It was noted that some types of top down cracks are very small at first and are only seen when stopping to get out of the car and look more closely. These types will grow with time and result in raveling and other problems. The reflective cracks from older underlying pavement and moisture/age induced cracks were most dominant in frequency and extent and thus dominate PCR data. These types of cracks were not evident in limestone asphalt pavements in the secondary system either in frequency or extent. The gravel problem consists of two significant problems. One is called 'popouts' where coarse aggregate has a soft core that with moisture/freeze/thaw and load breaks. Popouts create an ugliness issue for the surface of pavements but may not quickly lead to pavement failure, depending on the extent of material prone to this problem in the asphalt mixture. The PCR can rate these pavement problems as raveling if it is extensive. The material does not stand up to moisture as well and is not as sound a fine aggregate as is a whole natural or limestone sand (*40*)."

EXPERIMENTAL PROCEDURES

Surface Energy Measurements

Surface energy of aggregates is measured using the Universal Sorption Device (USD), while surface energy of binder is measured using the Wilhelmy Plate. The USD indirectly determines the aggregate surface energy by using gas adsorption characteristics of three solvents. The Wilhelmy Plate determines the surface energy of binder by using the contact angle between a thin plate coated with binder immersed and withdrawn from a liquid with a known surface energy components.

Universal Sorption Device

The aggregates are dry-sieved, passing the 4.75 mm sieve and retained on the 2.36 mm sieve. The aggregate size is controlled by the aluminum mesh aggregate sample holder used in the USD. Approximately 40 grams of aggregates retained on the

2.36 mm sieve are washed with potable water to remove dust particles. The aggregates are then put through a washing cycle for final preparation. The washing cycle consists of rinsing the aggregate with distilled water, then methanol, then hexane, then methanol again. After washing, the aggregates are placed in an oven and dried for at least 4 hours. After drying, the aggregates are cooled down to room temperature in a desiccator. Once cooled, the aggregates are placed in the aluminum mesh sample holder to be put in the USD.

The USD testing protocol at TTI was developed by Cheng and improved by many others since then (*41*, *42*). A brief summary of the test method will follow; however, greater detail is provided in Appendix C. A picture of the main components of the USD is provided in Figure 14. The aggregate sample is placed in a sealed vacuum chamber, while the pre-selected solvent is released into the chamber at a specific vapor pressure. A magnetic suspension balance measures the amount of solvent on the aggregate surface, while also measuring vapor pressure. The vapor pressure is increased and stabilized to the steady-state at 10 different stages while the mass of solvent is measured. The sample is tested in the following order with three solvents: nHexane, methyl propyl ketone (MPK), and water. A washing cycle is performed in between each solvent.

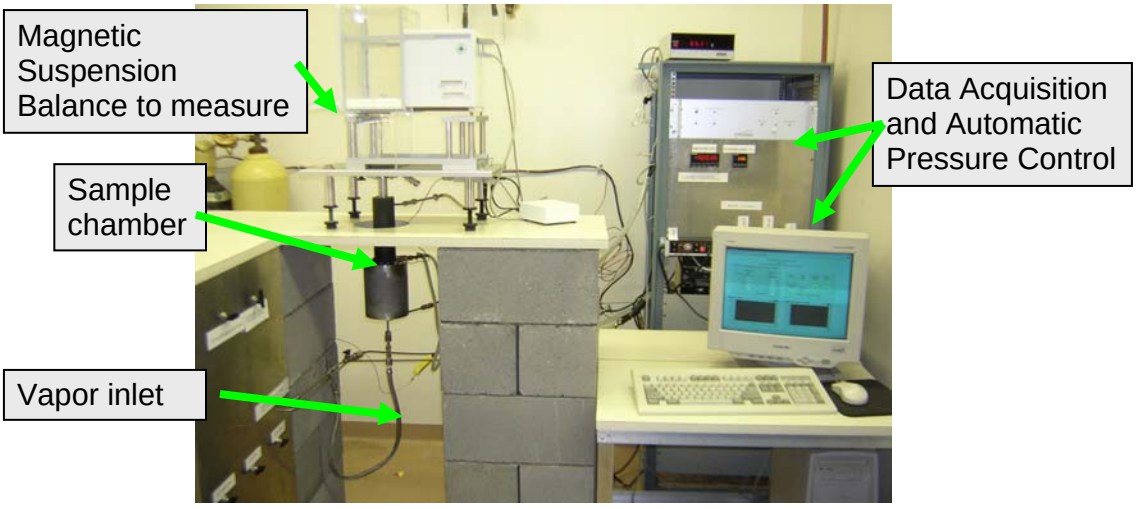

Figure 14. Universal Sorption Device.

The USD testing protocol requires inserting vapor into the chamber in 10 stages until reaching the saturation vapor pressure as seen in Figure 15. The adsorbed solvent mass is also measured for each stage and is shown in Figure 16. Figure 17 illustrates how these data can be used to construct an isotherm of the amount of solvent adsorbed versus relative pressure at constant temperature.

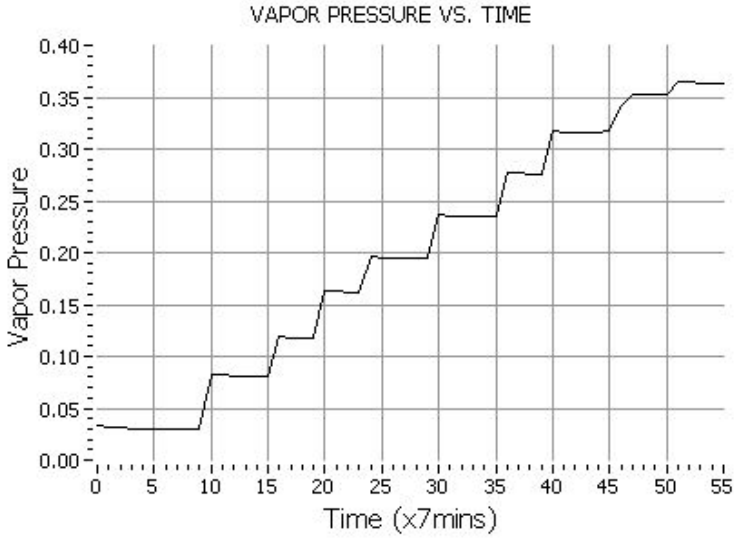

Figure 15. Vapor Pressure versus Time Plot from USD.

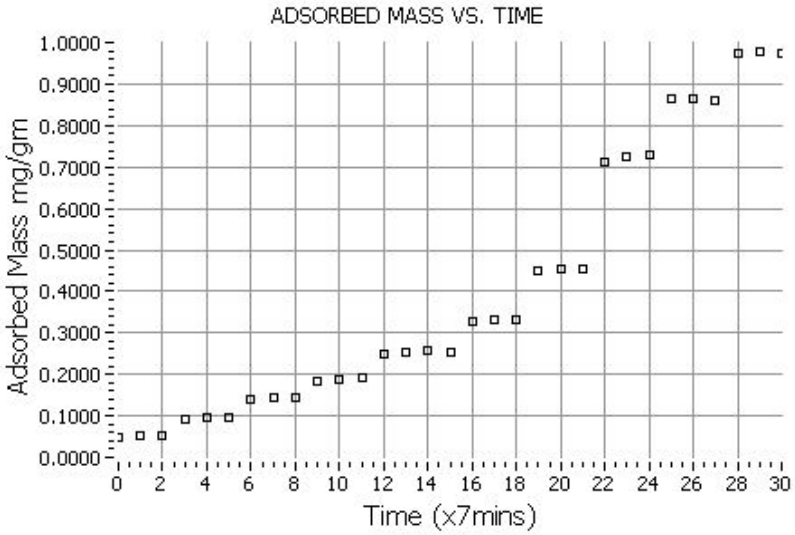

Figure 16. Absorbed Solvent Mass versus Time from USD.

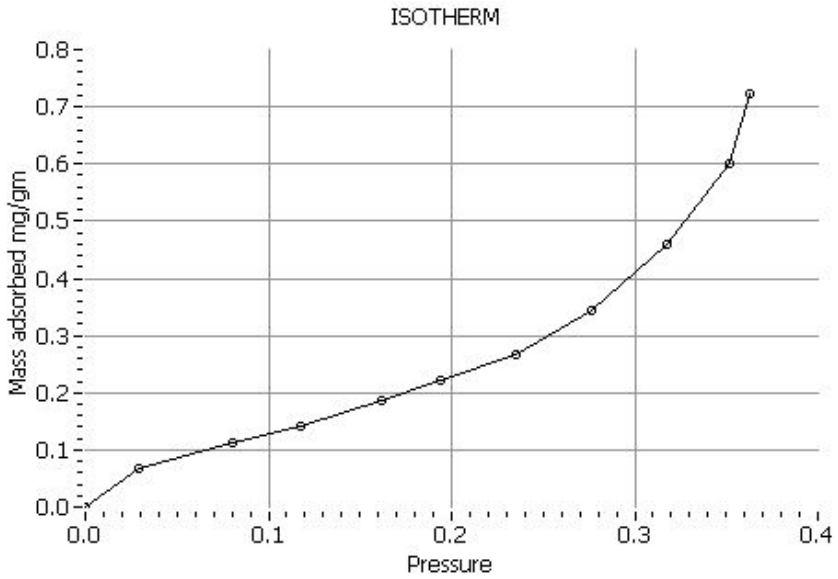

Figure 17. Typical Adsorbed Solvent Mass versus Vapor Pressure Isotherm.

The 10 stages of increasing vapor pressure and mass of solvent are used to calculate the specific surface area of the aggregate. The two-parameter BET (Brunauer, Emmett, and Teller) model is applied to the isotherm data to obtain the specific surface area of the aggregate sample for the three solvents adsorbed. According to the BET theory, adsorption can be represented by the following linear equation,

$$\frac{P}{n(P_O - P)} = \left(\frac{c-1}{n_m c}\right)\frac{P}{P_O} + \frac{1}{n_m c} \tag{32}$$

where, P_0 is the saturated vapor pressure of the solute, P is the vapor pressure, n is the specific amount adsorbed on the surface of the absorbent, n_m is the monolayer capacity of the adsorbed solute on the absorbent, and c is the parameter theoretically related to the net molar enthalpy of adsorption. The monolayer capacity of the adsorbed solute on the absorbent can be obtained from the slope and the intercept of the straight line that fits the plot *P/n(P-Po)* versus *P/Po* best, as illustrated in Figure 18.

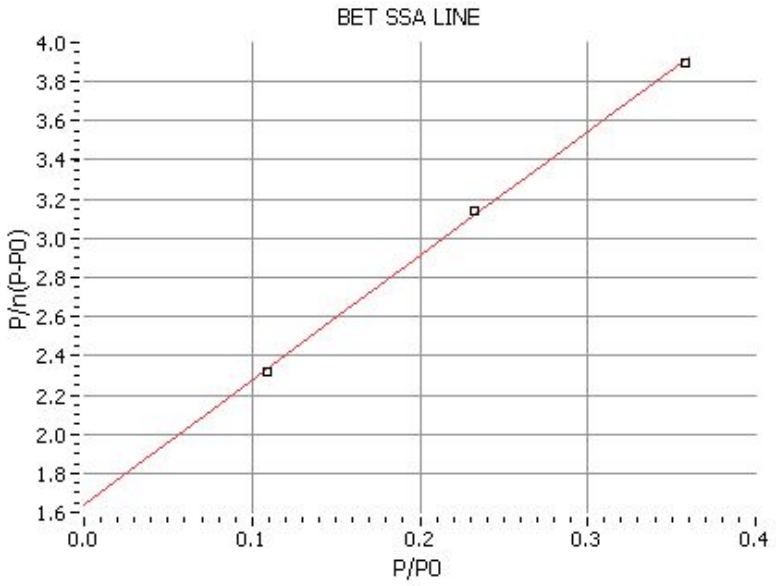

Figure 18. Plot for Determining Monolayer Capacity.

At the saturation vapor pressure, the spreading pressure is computed for all three solvents. With the components of surface energy for the three solvents known, the components of surface energy for the aggregate are then computed as described by Hefer (*42*) and in Appendix C.

Wilhelmy Plate

The asphalt surface energy is determined by dipping thin micro glass slides coated with thin asphalt into three pre-selected solvents with known surface energy components. Figure 19 shows the Dynamic Contact Angle (DCA) system comprising a data acquisition system and a Cahn balance used to measure the force data. Twelve glass slides (50 mm by 24 mm by 0.15 mm) are cleaned using acetone and distilled water. Once the glass slides are dried, the asphalt is heated to a liquid state at a temperature that depends on the asphalt grade. The glass plate is immersed into the liquid asphalt approximately 30 mm and then removed. The asphalt-covered plated is turned over, and while cooling the excess asphalt is allowed to drip off, creating a

smooth surface. The dimensions of the asphalt-covered plate are measured, and the plate is placed in the desiccator overnight.

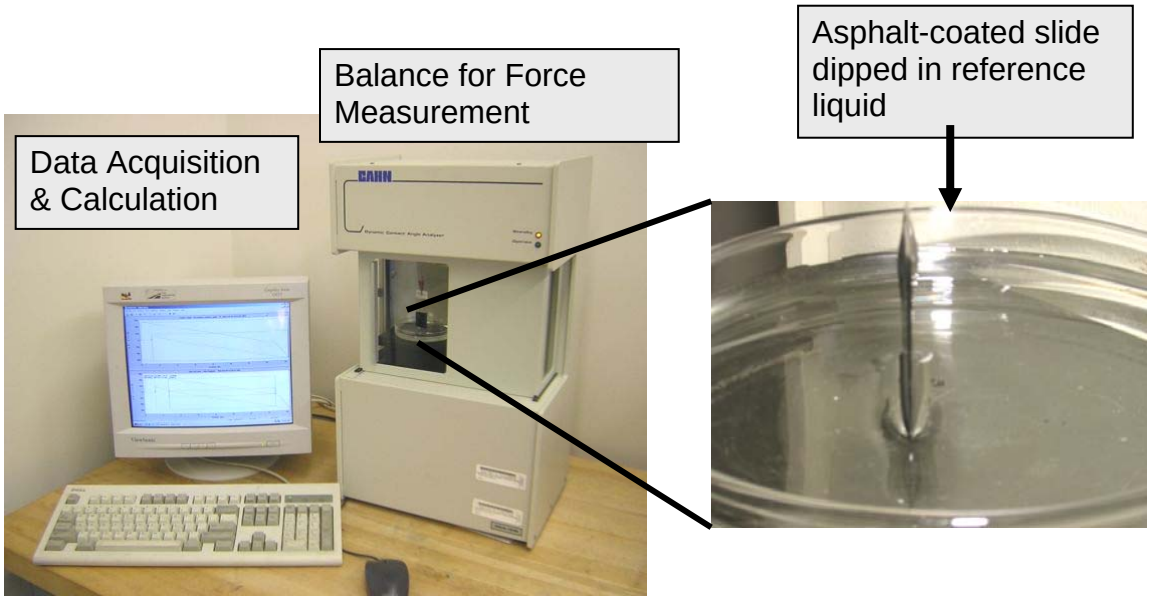

Figure 19. Dynamic Contact Angle System.

For each solvent, the contact angle is measured for three separate plates. The three solvents used in this project were water, glycerol, and methylene iodide. The asphalt-coated plate is attached to the Wilhelmy Plate device. The Whilhelmy plate immerses the plate into each solvent and then withdraws it. The contact angle measured during the immersion process is called the advancing contact angle, and the contact angle measured during the withdrawal process is known as the receding contact angle as illustrated in Figure 20.

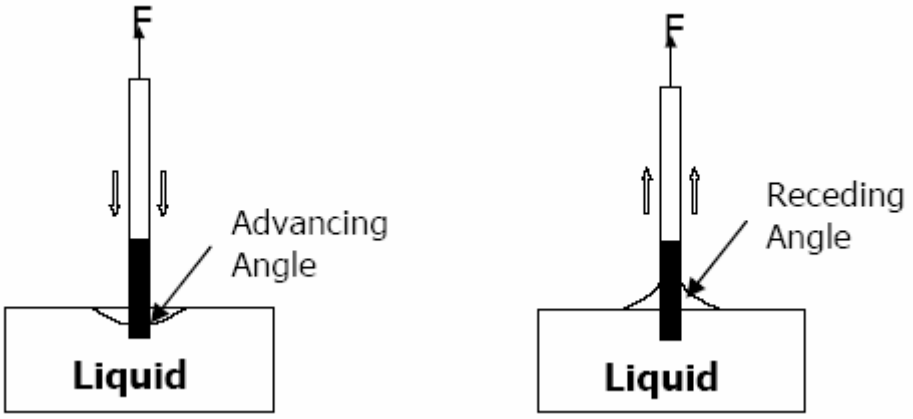

Figure 20. Schematic Illustration of Wilhelmy Plate Technique.

The surface energy determined from the advancing contact angle is the surface free energy of wetting and has been associated with the fracture healing process. The surface energy determined from the receding contact angle is the surface free energy of dewetting and has been associated with the fracture mechanism process (*41*). The Wilhelmy Plate measures the contact angle by constantly measuring the weight of the plate as it is immersed and withdrawn from the solvent. Before the plate is immersed, the dry plate mass is known. As the plate is immersed, the force applied to the plate is affected by the perimeter of the plate, surface energy of the solvent, contact angle between plate and solvent, and volume of immersed plate. Typical output from the DCA data acquisition system is show in Figure 21. The advancing contact angle is represented in the bottom portion of the hysteresis loop, while the receding contact angle is represented in the top portion. Knowing the contact angles between the solvents and asphalt, combined with the surface energy components of the solvents, the surface energy components of the asphalt can be computed as described by Hefer and also in Appendix D (*42*).

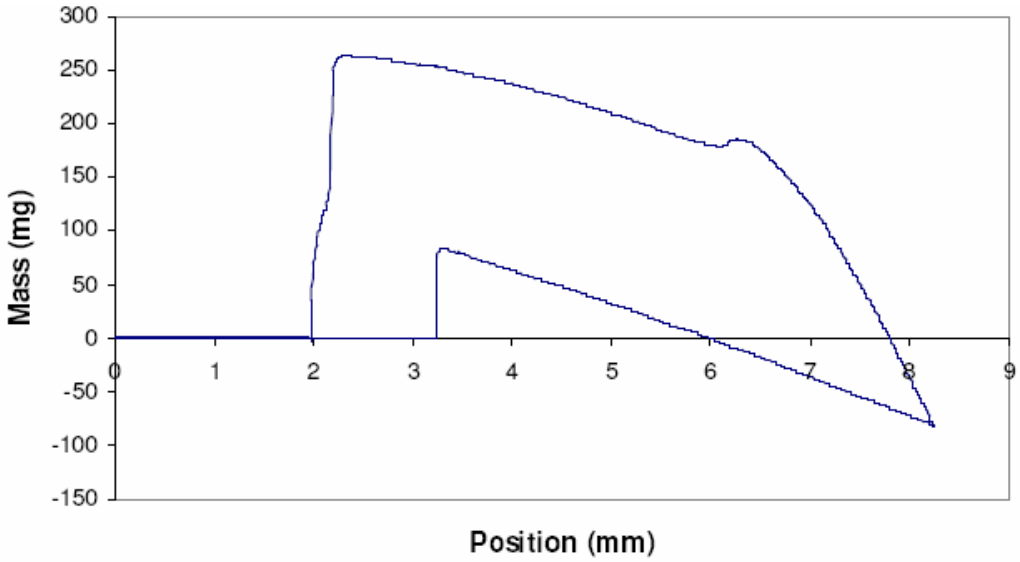

Figure 21. Typical Output from the DCA Data Acquisition System.

Dynamic Mechanical Analyzer (DMA)

DMA cylindrical specimens were prepared in this study using the binder mixed with the finer portion (minus 1.18 mm to pan) of the aggregate gradation. The DMA specimen aggregate gradation is proportioned according to the JMF as shown in Tables 2 and 3. Mixture 3 includes 69 percent quartzite screenings, 28 percent igneous screenings, and 3 percent hydrated lime by total weight of aggregate. Mixture 4 consists of 57 percent sandstone screenings, 38 percent igneous screenings, and 5 percent hydrated lime. Mixture 5 consists of 97 percent limestone screenings and 3 percent hydrated lime. Mixture 6 includes 68 percent sandstone screenings, 29 percent field sand, and 2 percent hydrated lime by total weight of aggregate. Mixture 7 consists of 72 percent natural sand and 28 percent limestone sand. Mixture 8 consists of 50 percent natural sand and 50 percent limestone sand.

Table 2. DMA Aggregate Gradations for Mixtures 3, 4, 5.

Sieve Size (mm)	Cumulative Percent Passing							
	Mix 3			Mix 4			Mix 5	
	Quartzite Screenings	Granite Donnafill	Hyd Lime	Sandstone Screenings	Granite Donnafill	Hyd Lime	Limestone Screenings	Hyd Lime
1.18	100.0	100.0	100.0	100.0	100.0	100.0	100.0	100.0
0.6	61.4	94.8	100.0	61.1	94.8	100.0	61.2	100.0
0.3	22.8	57.3	100.0	49.7	57.3	100.0	49.7	100.0
0.15	12.3	22.4	100.0	26.9	22.4	100.0	26.9	100.0
0.075	1.8	1.8	100.0	1.7	1.7	100.0	1.8	100.0

Table 3. DMA Aggregate Gradations for Mixtures 6, 7, 8.

Sieve #	Cumulative Percent Passing						
	Mix 6			Mix 7		Mix 8	
	Sandstone Screenings	Field Sand	Hyd Lime	Limestone Sand	Natural Sand	Limestone Sand	Natural Sand
1.18	100.0	100.0	100.0	100.0	100.0	100.0	100.0
0.6	-	-	-	60.1	64.0	60.1	64.0
0.425	40.2	98.5	100.0	-	-	-	-
0.3	-	-	-	25.4	23.3	25.4	23.3
0.18	18.0	28.8	100.0	-	-	-	-
0.15	-	-	-	6.3	2.9	6.3	2.9
0.075	1.8	1.8	100.0	1.8	1.8	1.8	1.8

The aggregate passing the 0.075 mm sieve is considered to be filler and is mixed with the pure binder at the pre-determined mixing temperature for the mixture. If the volume of filler is 10 percent of the binder volume, then 8 percent binder-filler mixture by mass of aggregate is mixed with the aggregate at the mixing temperature.

Two fabrication methods have been followed to fabricate cylindrical specimens 50 mm long and 12 mm diameter. The first method was developed by Kim (*32*) and is

illustrated in Figures 22-25. After the binder-filler is mixed with the aggregates, 15 gram samples of loose material are separated. Once cooled, 11.5 grams of the 15 gram samples are heated along with the specially fabricated mold in the oven to the pre-determined compaction temperature. After heating, the 11.5 grams are placed in the mold and compacted by applying static pressure. The mold and specimen are allowed to cool for 30 minutes before removing the specimen. The typical air void content of these specimens is 17 percent, as reported by Kim (*32*). Three hundred grams of aggregates are required to produce approximately 10 specimens.

Figure 22. Mixing Binder-Filler Mixture with Aggregates.

Figure 23. Completed Mixing.

Figure 24. Placing Mixture in Mold.

Figure 25. Completed DMA Specimen.

Initially during this study the researchers used this fabrication method. However, they found that this fabrication method does not compact the entire length of the specimen equally, leaving more air voids at the top. Because of this higher air void distribution, samples failed very close to the ends. Therefore, a new fabrication method was developed by researchers on this project. In this method, the filler is mixed with the pure binder in a can at the pre-determined mixing temperature. The binder-filler mixture is then mixed with the aggregates using a mechanical mixer, as is used to produce gyratory specimens at the mixing temperature. The loose mixture is then placed in the oven and aged at the proper aging temperature for 2 hours for short-term oven aging. The temperature is then changed to the compaction temperature for 1 hour.

The theoretical maximum specific gravity is determined for the mixtures used to prepare the DMA specimens. The loose mixture is placed in a 152 mm diameter gyratory mold and compacted using a SuperPave gyratory compactor to a target air void content of 11 percent and a height of 85 mm as illustrated in Figure 26. The sample is allowed to cool for 1 day. Each side of the specimen is trimmed about 17.5 mm to a sample height of 50 mm. Approximately 32 12 mm diameter DMA specimens are cored from the 152 mm diameter and 50 mm tall gyratory compacted sample as illustrated in Figure 27. Four thousand grams of aggregates are required to produce the 32 specimens. Of the 4000 grams, 500 grams are used for the theoretical maximum specific gravity determination.

Figure 26. Gyratory Compacted Specimen.

Figure 27. Cored Specimen.

It was evident that this new compaction method produced more uniformly compacted specimens. The air voids are easier to control because the theoretical maximum specific gravity is known, and sample preparation is much easier and less time consuming. Since these samples have higher compaction, they are stiffer and more uniform. This fabrication method, however, requires a large quantity of material compared to the previous method.

In order to use the DMA testing methodology to evaluate moisture damage, some DMA samples are tested in the dry condition, while others are preconditioned with moisture. Preconditioning is achieved following the method developed by Kim et al. (*43*). The first step is allowing moisture to penetrate the specimen by placing the specimen in distilled water and applying vacuum pressure to accelerate moisture permeation. The specimen remains under vacuum for 1 hour. As described by Kim, the average saturation level (volume of absorbed water to the volume of air voids) is approximately 125 percent, meaning some moisture may have diffused into the mastic.

DMA testing was performed using a Bohlin Instruments CVOR 200. The sample holders that came with the device required tightening of two screws on each end, which caused some misalignment. Therefore, sample holders and solid fixtures for the cylindrical samples were fabricated at the TTI machine shop. The new solid fixtures require tightening one set screw, which eliminated misalignment problems.

DMA testing begins with placing a DMA sample in the sample holder with Devcon 5 minute glue shown in Figure 28. The glue requires 20 minutes to stiffen. It is important to fill the sample holder with glue surrounding the specimen to ensure the fatigue cracking will occur in the center third of the specimen. The specimen is then mounted into the DMA chamber solid fixtures and time given to equilibrate to desired testing temperature of 25^{o}C as shown in Figures 29 and 30.

Figure 28. Specimen Placed in Sample Holders for DMA Testing.

Figure 29. Sample Mounted in DMA.

Figure 30. Temperature Equilibration.

A DMA specimen is subjected to sinusoidal torsional strain loading. The resulting stress is also sinusoidal but out of phase with strain with a magnitude equal to the phase angle as seen in Figure 31. In order to determine the linear viscoelastic material properties, dynamic modulus, and phase angle, a strain-controlled torsional cyclic test was conducted at a strain of 0.0065 percent, which is within the linear viscoelastic range, and at a frequency of 10 Hz. These properties were subsequently used to compute pseudostrain during the fatigue damage portion. In order to simulate fatigue damage, the same sample was then subjected to strain-controlled cyclic torsion at 0.3 percent strain at 10 Hz until failure for Mixtures 3 through 6. For Mixtures 7 and 8, fatigue damage torsional strain level was reduced to 0.2 percent because they were less

stiff than the other mixtures. Mixture 7 and 8 samples were initially tested at 0.3 percent strain; however, their fatigue lives were very short, they failed almost immediately. The shear strains are high enough to produce fatigue damage with time.

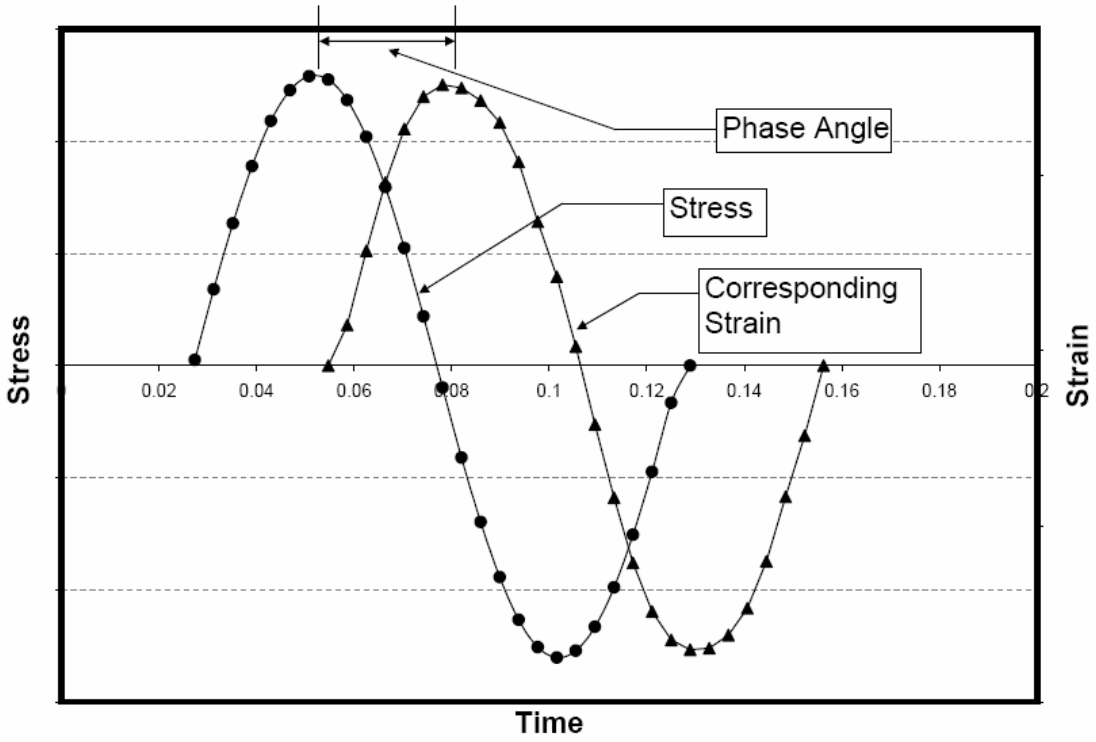

Figure 31. Typical DMA Sample Time Profile of Stress and Strain.

A detailed description for operating the CVOR 200 is provided in Appendix E, while a brief summary is provided herein. A summary data file provided by the software computes dynamic modulus, elastic modulus, viscous modulus, phase angle, complex viscosity, shear stress, strain, and normal force for each testing cycle. The raw data retrieved from the provided Bohlin software during each cycle are torque (T), and displacement (δ); a Fourier Transform (FT) fits the data and computes the previous properties. The software provides the user the ability to choose the number of cycles and the number of points per cycle to be used in the FT to output data to the summary file. Based on the experience during this study, the CVOR 200 is not capable of

performing FT for every cycle at high frequencies such as 10 Hz. For this reason, the researchers collected data every 5 cycles and used 128 points per those 5 cycles to perform the FT.

In order to use DMA testing to evaluate the rate of damage accumulation in asphalt binders and mastics, the researchers used the raw data to compute stress, strain, pseudostrain, dissipated pseudostrain energy, and pseudostiffness for each cycle. The stress and strain are computed by:

$$\sigma = T \times C_1 \tag{33}$$

$$\varepsilon = \delta \times C_2 \tag{34}$$

where, T is the applied torque, δ is the resulting displacement, and C_1 and C_2 are form factors provided by the Bohlin software related to the inertia of the solid fixtures used to mount the specimen. Pseudostrain, dissipated pseudostrain energy, and pseudostiffness are computed as described in the previous chapter. DMA data analysis is provided in the following chapter.

Dynamic Modulus

The dynamic modulus test procedure applies a sinusoidal axial compressive stress to an HMA specimen at different temperatures and loading frequencies. The dynamic modulus and phase angle are calculated using the measured applied stress and resulting recoverable strain responses from sinusoidal, stress-controlled loading. Dynamic modulus, expressed as E*, is calculated by dividing the peak-to-peak stress by the peak-to-peak strain. Phase angle (ϕ) is the lag time measured in degrees between applied stress and resulting strain. A master constructed using the dynamic modulus and phase angle values measured at different temperatures and frequencies characterizes both the rutting and fatigue performance of HMA mixtures.

This test is conducted according to AASHTO Test method TP 62-03 "Determining Dynamic Modulus of Hot-Mix Asphalt Concrete Mixtures (*44*)." The samples are 100 mm diameter, 152 mm high, compacted specimens. The samples are compacted to the desired air void content determined by AASHTO Test method T 312-

01 “Preparing and Determining the Density of Hot-Mix Asphalt Specimens by Means of the Superpave Gyratory Compactor (*45*).” The compaction temperature is determined according to the binder grade in the Mixing and Compaction Temperatures table in test method Tex 206-F: “Compacting Specimens Using Texas Gyratory Compactor (*46*).” Initially, the specimens are compacted to 152 mm diameter and 178 mm height. The final specimen (100 mm diameter and 152 mm height) is obtained by coring from the 152 mm diameter specimen and sawing the two ends. The final air void content of the cored specimens is maintained within 7 ± 0.5 percent. Six replicate specimens from each Mixture 3 through 8 were compacted.

In order to use the Dynamic Modulus testing methodology to evaluate moisture damage, three replicates were tested in the dry condition and three were preconditioned with moisture. Preconditioning samples with moisture was achieved following the AASHTO Test Method T283-02 “Resistance of Compacted Asphalt Mixtures to Moisture-Induced Damage (*47*).” The specimens were placed in distilled water with a vacuum with 13-67 kPa partial pressure for a short time to bring the degree of saturation to between 70 and 80 percent. The specimens were then placed in a water bath containing potable water at 60 ± 1^{o}C for 24 ± 1 hours. After the warm water bath, the specimens were placed in a water bath at 25 ± 1^{o}C for 2 ± 1 hours. The specimens were removed and tested.

Testing was performed on three dry and three wet replicates for each mixture, each with three linear variable differential transducers (LVDTs) for recording the strain. The LVDTs were fixed to the specimen using fastening clamps glued to the specimen surface. The studs were spaced 100 mm apart with about 25 mm from either face of the specimen. Each LVDT was placed at 120° from the other around the cylindrical surface. Each specimen was tested at six different frequencies of loading and four different temperatures. The loads selected were such that the total strain in the specimen would be 50 to 150 microstrains to keep sample deformation within the linear range. The specimens were brought to the required test temperature by placing them in an

environmental test chamber for a minimum of 2 hours for 21.1, 37.8, and 54.4°C and for a period of four hours for 4.4°C.

In order to minimize damage to the specimens, the test was conducted from the highest frequency and proceeded to the lowest frequency at each temperature and then started from the lowest temperature and proceeded to the highest level. Before application of axial load, two latex sheets were placed between each end of the specimen and loading platens to reduce the shearing stresses at the specimen ends.

The resulting strains were recorded using a data acquisition system and a desktop computer. The final values of the phase angle (ϕ) and modulus of elasticity ($|E^*|$) were calculated using the average of the results from the last five loading cycles. The master curve was plotted for each of the three replicates for both wet and dry conditions. Different shifting techniques can be used to construct the master curve on the basis of time-temperature superposition. In this project, a sigmoidal function was employed for construction of the master curve. Witczak et al. showed that for the wide range of temperatures for the compressive dynamic modulus testing data, using the sigmoidal fitting function fit the data well because it followed the physical form of the measured data (*48*). The master curve was plotted for each mixture using a sigmoidal function described as follows (*45*):

$$\log\left(|E^*|\right) = \delta + \frac{\alpha}{1 + e^{\beta + \gamma \log\left(\frac{1}{\omega_r}\right)}} \tag{35}$$

where, $|E^*|$ refers to dynamic modulus, ω_r is the frequency of loading at reference temperature, δ is the minimum modulus value, $\delta+\alpha$ is the maximum modulus value, and β and γ are shape parameters describing the shape of sigmoidal function. Equation (35) represents a curve which is flat at very high and very low values of log(t) and typically represents the behavior of a viscoelastic material. The four variables involved in the model α , δ, γ, and β, along with the shift factors for the other three temperature ranges, are derived simultaneously using a nonlinear regression analysis supported by the solver function in the Microsoft Excel spreadsheet. The reference temperature was selected

arbitrarily to be 21.1°C. The elastic modulus values for other temperatures were shifted to this value for plotting the master curve.

Aggregate Characterization Using Aggregate Imaging System

Researchers have developed the Aggregate Imaging System (AIMS) to capture images and analyze the shape of aggregates for form, angularity, and texture (*49*). AIMS uses a setup that consists of one camera and two different types of lighting schemes to capture images of aggregates at different resolutions, from which aggregate shape properties are measured using image analysis techniques as seen in Figure 32.

The system operates based on two modules: One for analyzing fine aggregates (smaller than 4.75 mm), where black and white images are captured, and another for analyzing coarse aggregates (larger than 4.75 mm) where both black and white images and gray images are captured. In the coarse module, gray images are used to analyze textures and black and white images are used to analyze angularity. Only one particle is captured per image in order to facilitate the quantification of form, which is based on three-dimensional (3-D) measurements.

The analysis starts by placing the aggregates on the sample tray with marked grid points with a distance of 50 mm in the x-direction and 40 mm in the y-direction from center to center. The camera and microscope move to each particle, capturing an image. Two scans are conducted for the coarse aggregate, one with backlighting and another with top lighting. Backlighting is used to capture black and white images for the analysis of angularity and the major (longest axis) and minor (shortest axis) axes on these two-dimensional images. Top lighting is used to capture gray images for texture analysis.

The texture scan starts by focusing the video microscope on a marked point on the lighting table while the backlighting is turned on. The location of the camera on the z-axis at this point is the reference point (set to zero coordinate). Then an aggregate particle is placed over the calibration point. With the top light on, the video microscope moves up automatically on the z-axis in order to focus on the aggregate surface. The z-

axis coordinate value on this new position is recorded. Since the video microscope has a fixed focal length, the difference between the z-axis coordinate at the new position and the reference position (zero) is equal to aggregate depth. This procedure is repeated for all particles. The particle depth is used along with the dimensions measured on black and white images to analyze particle shape or form (*46*).

Figure 32. Aggregate Imaging System.

The analysis of fine aggregates starts by spreading the particles randomly on the lighting table. Then the microscope assembly captures images of these particles while the bottom lighting is on.

In order characterize the aggregate properties in ways practitioners can use them, Masad has developed methods to analyze the captured images. The following methods are described in greater detail by Masad (*49*):

- Texture Analysis Using Wavelets (Texture Index),
- Angularity Analysis Using Gradient Method (Angularity Index), and
- Form Analysis Using Sphericity (Shape Index).

CHAPTER IV
RESULTS AND DATA ANALYSIS

INTRODUCTION

This chapter includes analysis of the DMA and surface energy measurements. The surface energy measurements are used to compute the cohesive and adhesive bond energies associated with fracture (dewetting) and healing (wetting). A new procedure was developed to analyze the DMA results based on the dissipated pseudostrain energy per unit volume of the intact material or the volume of material that is able to dissipate energy. The results are compared to the field performance of the mixes that are classified as "poor" or "good" performing mixes in terms of resistance to moisture damage. The analysis methods presented in this chapter can be used by engineers to properly select the combinations of aggregates and binders that enhance their resistance to moisture damage.

SURFACE ENERGY

The USD and Wilhelmy Plate (WP) tests determined the three surface energy components of aggregates and asphalts, respectively.

The USD measures spreading pressure of various probe liquids on an aggregate surface, which is then used to calculate surface energy components of the aggregates. Table 4 presents the spreading pressures of the probe vapors on the aggregates and the computed specific surface areas of the aggregates. Since surface energy is an intrinsic material property dictated by the type of mineral surface of the aggregate, it is reasonable to expect similar surface energy values for aggregates of similar mineralogy. In asphalt mixtures, it is common to have a few different aggregate types in the JMF. For the mixtures in this study with different aggregate mineralogys, the researchers tested each aggregate type between 4.75 mm and 2.36 mm separately. The aggregates for Mixtures 1 and 2 were the same, and the aggregates for Mixtures 4 and 6 were the same within this size category.

Table 5 summarizes the calculated surface energy components for the aggregates based on the spreading pressures. Table 6 summarizes the advancing contact angles for the asphalts, and Table 7 summarizes the calculated asphalt surface energy components based on the advancing contact angles.

Table 4. Specific Surface Areas and Spreading Pressures of Vapors on Aggregates.

Mix	Aggregate Type	SSA (m^2/g)	Spreading Pressures (erg/cm^2)		
			Hexane	MPK	Water
1 & 2	Granite	0.67	27.62	90.78	273.62
3	Quartzite	1.35	30.11	57.85	193.17
4 & 6	Light Sandstone	0.83	31.04	43.34	93.37
4 & 6	Dark Sandstone	1.00	31.85	59.13	138.38
5	Gravel	0.80	29.46	38.14	108.35
5	Limestone Screenings	0.49	29.67	70.65	209.76
7 & 8	Limestone	0.53	28.56	39.56	141.24
7 & 8	Gravel	4.76	31.68	57.48	192.98

Table 5. Surface Energy Components of Aggregates.

Mix	Aggregate Type	Surface Energy Components (erg/cm^2)				
		Γ	Γ^{LW}	Γ^{AB}	Γ^{+}	Γ^{-}
1 & 2	Granite	425.22	56.34	368.88	43.59	782.71
3	Quartzite	200.13	60.81	139.22	8.86	545.04
4 & 6	Light Sandstone	105.05	62.43	42.55	2.033	222.67
4 & 6	Dark Sandstone	167.88	63.96	103.93	8.52	316.92
5	Gravel	96.59	59.49	37.06	1.25	286.03
5	Limestone Screenings	265.47	59.88	205.59	18.88	561.15
7 & 8	Limestone	111.14	58.05	53.01	1.77	401.18
7 & 8	Gravel	193.21	63.42	129.74	7.74	546.37

Table 6. Contact Angle of Probe Liquids on Asphalt Slides for Wetting.

Mix	Contact Angle (°)					
	Diiodomethane		Ethylene Glycol		Water	
	Avg	CV (%)	Avg	CV (%)	Avg	CV (%)
1	68.66	0.13	88.45	0.11	100.10	0.09
2	86.14	0.01	86.87	0.01	99.35	0.02
3, 4, & 5	91.26	0.04	90.53	0.01	99.89	0.02
6	71.17	0.03	84.86	0.00	100.26	0.00
7	57.54	0.07	86.91	0.00	99.14	0.00
8	77.54	0.14	92.51	0.00	100.19	0.01

Avg: Average
CV: Coefficient of variation

Table 7. Surface Energy Components of Asphalts for Wetting.

Mix	Asphalt Grade	Surface Energy Components (erg/cm^2)				
		Γ	Γ^{LW}	Γ^{AB}	Γ^{+}	Γ-
1	76-22	24.32	23.61	0.63	0.01	1.32
2	76-22	17.65	14.44	3.16	1.32	1.85
3, 4, & 5	76-22	15.71	12.17	3.59	1.13	2.88
6	76-22	23.44	22.28	1.28	0.55	0.69
7	64-22	30.07	29.95	0.05	0.01	1.02
8	64-28	19.68	18.72	0.83	0.01	2.75

Once the surface energy of asphalts and aggregates are known, the adhesive bond strength with and without the presence of water can be calculated using Equations (9-16) shown in the previous chapter. Tables 8 and 9 show the calculated adhesive bond energies at the asphalt-aggregate interface in dry and wet conditions for both the wetting and dewetting angles. Table 10 shows the calculated cohesive bond energy for each asphalt.

Table 8. Adhesive Wetting Bond Energy under Both Dry and Wet Conditions.

Mix	Reported Performance	Aggregate	Adhesive Dry (erg/cm^2)			Adhesive Wet (erg/cm^2)		
			ΔG^a Dry	ΔG^{LW} Dry	ΔG^{AB} Dry	ΔG^a Wet	ΔG^{LW} Wet	ΔG^{AB} Wet
1	Pass Hamburg Requirement	Granite	140.61	57.10	83.51	-193.99	-4.91	-189.08
2	Fail Hamburg Requirement	Granite	104.72	72.97	31.75	-228.93	1.09	-230.02
3	Good	Quartzite	114.00	54.38	59.62	-139.43	-7.42	-132.01
4	Good	Light Sandstone	91.57	55.09	36.48	-61.99	-7.66	-54.34
4	Good	Dark Sandstone	103.38	55.75	47.63	-95.25	-7.88	-87.36
5	Good	Gravel	93.36	53.77	39.59	-75.20	-7.21	-68.00
5	Good	TXI Limestone	118.87	53.95	64.92	-151.14	-7.27	-143.87
6	Poor	Light Sandstone	99.61	74.51	25.10	-53.49	0.29	-53.78
6	Poor	Dark Sandstone	107.31	75.40	31.90	-90.86	0.30	-91.16
7	Poor	Limestone	87.49	83.42	4.07	-115.58	4.76	-120.34
7	Poor	Gravel	94.56	87.26	7.29	-160.22	5.33	-165.55
8	Poor	Limestone	81.27	66.00	15.27	-119.82	-1.98	-117.84
8	Poor	Gravel	90.92	69.04	21.89	-161.87	-2.22	-159.65

Table 9. Adhesive Dewetting Bond Energy under Both Dry and Wet Conditions.

Mix	Reported Performance	Aggregate	Adhesive Dry (erg/cm^2)	Adhesive Wet (erg/cm^2)
			ΔG^a Dry	ΔG^a Wet
1	Pass Hamburg Requirement	Granite	193.55	-179.21
2	Fail Hamburg Requirement	Granite	182.98	-196.53
3	Good	Quartzite	143.15	-143.88
4	Good	Light Sandstone	126.72	-60.450
4	Good	Dark Sandstone	139.30	-92.931
5	Good	Gravel	124.61	-77.558
5	Good	TXI Limestone	150.18	-153.43
6	Poor	Light Sandstone	158.77	-48.98
6	Poor	Dark Sandstone	180.56	-72.25
7	Poor	Limestone	168.42	-85.02
7	Poor	Gravel	193.61	-111.53
8	Poor	Limestone	151.84	-92.07
8	Poor	Gravel	173.04	-122.58

Table 10. Cohesive Bond Energy under Both Dry and Wet Conditions.

Mix	Asphalt Grade	Cohesive Bond Energy (erg/cm^2)	
		ΔG^c Dry	ΔG^c Wet
1	76-22	35.22	58.91
2	76-22	48.66	74.14
3, 4, & 5	76-22	31.49	56.47
6	76-22	46.88	72.88
7	64-22	60.15	81.95
8	64-28	39.32	65.12

Bond energy without the presence of water is positive, which means that energy must be supplied to the system to cause debonding between the asphalt and aggregate. However, in the presence of water, this energy is negative, which means that there is a release of free energy when water displaces asphalt from the asphalt-aggregate interface. Therefore, water damage is a thermodynamically favorable phenomenon. The greater the magnitude of the released free energy, the greater will be the drive for water to displace asphalt and cause debonding at the interface. It is important to note that the magnitudes of fracture and healing energies alone cannot be used as global indicators of moisture damage. This is because other mixture properties such as aggregate gradation, asphalt film thickness distribution, and ability of an asphalt film to hold and transfer moisture (diffusivity) can also influence the propensity of the mixture to undergo moisture damage. Nonetheless, the bond energy values can give an overall idea of poor combinations of aggregates and binder that could produce mixes susceptible to moisture damage. The remaining part of this section discusses some observations on the relationships between bond energies and rankings based on moisture damage, while a procedure that combines physical and chemical properties of asphalt mixes for evaluation of moisture damage is presented in the following section.

In order to use the calculated bond energies to compute moisture susceptibility and reduce the effects of varying mixture properties among the mixes such as aggregate gradations, asphalt film thicknesses, and specific surface area of the aggregates, the mixtures are ranked according to the wet condition surface energy value divided by the dry condition surface energy value. Tables 11 and 12 show the adhesive wet bond

Table 11. Mixture Rankings According to Adhesive Wetting Bond Energy under Both Dry and Wet Conditions.

Mix	Reported Performance	Aggregate	$\frac{\Delta G^{aW}}{\Delta G^{aD}}$
6	Poor	Light Sandstone	-0.53
4	Good	Light Sandstone	-0.67
5	Good	Gravel	-0.80
6	Poor	Dark Sandstone	-0.84
4	Good	Dark Sandstone	-0.92
3	Good	Quartzite	-1.22
5	Good	Limestone	-1.27
7	Poor	Limestone	-1.32
1	Pass Hamburg Requirement	Granite	-1.37
8	Poor	Limestone	-1.47
7	Poor	Gravel	-1.69
8	Poor	Gravel	-1.78
2	Fail Hamburg Requirement	Granite	-2.18

Table 12. Mixture Rankings According to Adhesive Dewetting Bond Energy under Both Dry and Wet Conditions.

Mix	Reported Performance	Aggregate	$\frac{\Delta G^{aW}}{\Delta G^{aD}}$
6	Poor	Light Sandstone	-0.30
6	Poor	Dark Sandstone	-0.40
4	Good	Light Sandstone	-0.47
7	Poor	Limestone	-0.50
7	Poor	Gravel	-0.57
8	Poor	Limestone	-0.60
5	Good	Gravel	-0.62
4	Good	Dark Sandstone	-0.66
8	Poor	Gravel	-0.70
1	Pass Hamburg Requirement	Granite	-0.92
3	Good	Quartzite	-1.00
5	Good	Limestone	-1.02
2	Fail Hamburg Requirement	Granite	-1.07

energy (ΔG^{aW}) divided by the adhesive dry bond energy (ΔG^{aD}) for both wetting and dewetting angles, with the best performer at the top of the table. As discussed previously, the total adhesive bond energy for the wetting angle has been correlated to healing ability of the mixture, while the dewetting angle has been correlated to fracture resistance of the mixture. The smaller the value of $\Delta G^{aW}/\Delta G^{aD}$, the smaller the magnitude of the released free energy will be which in turn reduces the drive for water to displace asphalt and cause debonding at the interface. Mixture 6 was designated at the beginning of this study by field engineers as a poor performer in the field. However the values in Tables 11 and 12 indicate that this mix should have good resistance to moisture damage because of its low reduction in resistance to fracture and low reduction in its healing capability with the presence of water. This finding is in agreement with the DMA and dynamic modulus test results presented later in this chapter. Therefore, it is very likely that reasons other than material properties caused Mixture 6 to be labeled as a poor performing mix. This is supported by observation on field cores that were taken in June 2004, which shows Mixture 6 to be "completely in tack with no rutting and visually in good shape"; however, cores taken on the same roadway at a different location describe it to be "severely stripped." After discussions with TxDOT, it was found that the second set of cores was from a different JMF than the materials tested in this study. Based on the results in Table 11, ratios higher than -1.2 seem to capture good combinations of aggregate and binder, while mixes with ratios less than -1.2 seem to exhibit problems in terms of moisture damage.

Mixtures 7 and 8 are clearly poor performing mixtures as related to adhesive bond energy. Mixture 7 performed better in the field than Mixture 8 because it contains less gravel than Mixture 8. As shown in Table 11, the gravel portion of Mixtures 7 and 8 performed poorer than the limestone portion of Mixtures 7 and 8. Mixtures 1 and 2 have the same aggregates but different asphalts. The results in Table 11 show clearly that the binder used in Mixture 1 healed better with the aggregates under wet conditions than the binder used in Mixture 2. As mentioned in the previous chapter, Mixture 1 passed the TxDOT requirements for rutting in the Hamburg device while Mixture 2

experienced more rutting and did not pass the Hamburg requirements. In general, the wetting bond energy, values in Table 11 agree with the ranking of the mixes more than do the dewetting bond energy values in Table 12.

Table 13 shows the cohesive wet bond energy divided by the cohesive dry bond energy, with the best performer at the top of the table. As discussed previously, the total cohesive bond energy relates to fracture and healing properties of the binder. The parameter, $\Delta G^{cW}/\Delta G^{cD}$, only evaluates binders and the increased work required for water to propagate as a crack. This parameter is not a direct measure of the moisture susceptibility of the mixture; however, it can provide details on the binders' ability to resist water cracks propagating to the aggregate interface. This demonstrates again why Mixture 1 binder performed better than the Mixture 2 binder.

Table 13. Mixture Rankings According to Cohesive Bond Energy in Both Dry and Wet Conditions.

Mix	Reported Performance	$\frac{\Delta G^{cW}}{\Delta G^{cD}}$
3, 4 , 5	Good	1.79
1	Pass Hamburg Requirement	1.67
8	Poor	1.65
6	Poor	1.55
2	Fail Hamburg Requirement	1.52
7	Poor	1.36

As discussed previously, the LW and AB components of surface energy obtained from the wetting contact angle have been correlated to healing. The LW component has been correlated inversely to short-term healing, while the AB component has been correlated directly to long-term healing. Table 14 shows the adhesive wet LW component bond energy divided by the adhesive dry LW component bond energy, with the best performer at the top of the table. In order to be a good short-term healer, the LW component should be close to zero and positive. For the negative value, the larger the value (less negative) the better; however, a positive value is always better than

negative. Table 15 shows the adhesive wet AB component bond energy divided by the adhesive dry AB component bond energy, with the best performer at the top of the table. In order to be a good long-term healer, the AB component should be as large as possible and positive. The results in Tables 14 and 15 show that the mixture rankings agree with long-term healing more than with short-term healing.

Table 14. Mixture Rankings According to Adhesive LW Component of Bond Energy in Both Dry and Wet Conditions.

Mix	Reported Performance	Aggregate	$\frac{\Delta G^{aLWW}}{\Delta G^{aLWD}}$
6	Poor	Light Sandstone	0.00
6	Poor	Dark Sandstone	0.00
2	Fail Hamburg Requirement	Granite	0.01
7	Poor	Limestone	0.05
7	Poor	Gravel	0.06
8	Poor	Limestone	-0.03
8	Poor	Gravel	-0.03
1	Pass Hamburg Requirement	Granite	-0.08
5	Good	Gravel	-0.13
5	Good	Limestone Screenings	-0.13
3	Good	Quartzite	-0.13
4	Good	Light Sandstone	-0.13
4	Good	Dark Sandstone	-0.14

Table 15. Mixture Rankings According to Adhesive AB Component of Bond Energy in Both Dry and Wet Conditions.

Mix	Reported Performance	Aggregate	$\frac{\Delta G^{aABW}}{\Delta G^{aABD}}$
4	Good	Light Sandstone	-1.48
5	Good	Gravel	-1.71
4	Good	Dark Sandstone	-1.83
6	Poor	Light Sandstone	-2.14
3	Good	Quartzite	-2.21
5	Good	Limestone Screenings	-2.21
1	Pass Hamburg Requirement	Granite	-2.26
6	Poor	Dark Sandstone	-2.85
2	Fail Hamburg Requirement	Granite	-7.24
8	Poor	Gravel	-7.29
8	Poor	Limestone	-7.71
7	Poor	Gravel	-22.70
7	Poor	Limestone	-29.53

DYNAMIC MECHANICAL ANALYSIS

The DMA was used to evaluate each mixture's ability to accumulate damage. The DMA applies a cyclic, torsional strain-controlled loading to cylindrical asphalt mastics until failure. For each mixture, a minimum of 10 samples were tested in both the wet and dry conditions.

Linear Viscoelastic Properties (LVE)

LVE properties were determined with a cyclic loading strain amplitude equal to 0.0065 percent during the low-strain portion of the testing protocol and are presented in Tables 16 and 17. Mixture 5 has the highest dry LVE dynamic modulus of 242×10^6 Pa, with the lowest dry LVE phase angle of 19.2°. Mixture 8 has the lowest dry LVE dynamic modulus of 108.4×10^6 Pa, with the highest dry LVE phase angle of 33.5°. These parameters are not used to determine moisture susceptibility.

Table 16. DMA Linear Viscoelastic Dynamic Modulus in Both Dry and Wet Conditions.

Mix	LVE Modulus (G*) (Pa)	
	Dry (× 10^6)	Wet (× 10^6)
3	177.9	174.6
4	188.9	143.5
5	242.0	206.0
6	163.3	146.7
7	158.1	190.8
8	108.4	134.2

Table 17. DMA Linear Viscoelastic Phase Angle in Both Dry and Wet Conditions.

Mix	LVE Phase Angle (δ) (°)	
	Dry	Wet
3	24.0	24.1
4	22.9	29.0
5	19.2	26.3
6	30.5	33.7
7	26.6	22.8
8	33.5	29.9

Empirical Parameters for Moisture Damage Evaluation

Researchers used a number of parameters to analyze the data. Fatigue life has been used by a number of researchers in the past to assess the asphalt mastic and mix resistance to fatigue damage (*28-32*). Consequently, the first parameter is the number of cycles at failure or fatigue life (N_f) shown in Figure 33. Figure 33 illustrates a typical plot of N×G'/G and G'/G versus number of load cycles used to determine fatigue life for each sample.

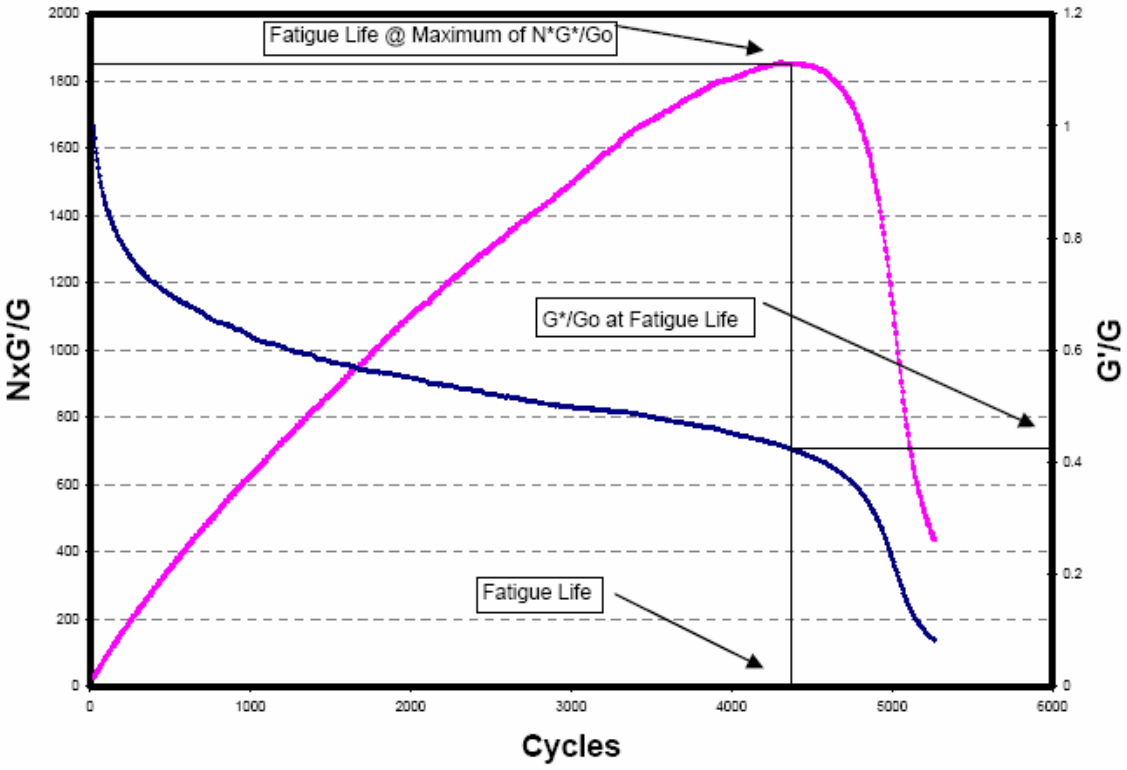

Figure 33. Typical Plot of N×G'/G and G'/G versus Number of Load Cycles.

As discussed in the previous chapter, the experimental plan included applying a strain amplitude of 0.3 percent to cause damage to the specimens. However, researchers found that Mixtures 7 and 8 could not sustain this level of strain, and they decided to reduce the strain amplitude to 0.2 percent for Mixtures 7 and 8. It can be seen later in Equation (51) that the slope of W_R – Ln (N) is a function of the square of the pseudostrain. Therefore, the slope at 0.3 percent strain can be taken to be 2.25 i.e. $[0.3/0.2]^2$ times the slope at 0.2 percent strain. The fatigue life at 0.3 percent strain can also be estimated from fatigue life at 0.2 percent strain under the assumption that the material dissipates the same total energy at both the 0.2 percent and 0.3 percent strain levels:

$$W_R @ N_f\Big|_{\varepsilon=0.3\%} = W_R @ N_f\Big|_{\varepsilon=0.2\%} \tag{36}$$

$$\int_{1}^{N_f} \frac{\partial W_R}{\partial N} dN + W_R @ N_1 \Big|_{\varepsilon=0.3\%} = \int_{1}^{N_f} \frac{\partial W_R}{\partial N} dN + W_R @ N_1 \Big|_{\varepsilon=0.2\%} \quad (37)$$

It is reasonable to assume that the difference in W_R in the first cycle between the two strain levels is negligible compared with the total W_R. Therefore, Equation (37) becomes Equation (38) after solving the integration:

$$\frac{\partial W_R}{\partial \ln N} ln\, N_f \Big|_{\varepsilon=0.3\%} = \frac{\partial W_R}{\partial \ln N} ln\, N_f \Big|_{\varepsilon=0.2\%} \quad (38)$$

Equation (38) can be used to calculate N_f at 0.3 percent strain for Mixtures 7 and 8. Table 18 provides the average fatigue life in both the wet and dry condition, along with the moisture damage parameter wet N_f/Dry N_f. The values in brackets are the ones measured at 0.2 percent for Mixtures 7 and 8. The higher the wet/dry ratio, the better the mixture performs, as the wet fatigue life is closer to the dry fatigue life. Mixture 4 has the highest ratio of 0.9, while Mixture 3 has the lowest at 0.08.

Table 18. Mixture Rankings According to Average Fatigue Life in Both Dry and Wet Conditions.

Mix	Reported Performance	Average Fatigue Life (N_f)		$\frac{\text{Wet } N_f}{\text{Dry } N_f}$
		Dry	Wet	
3	Good	25,205	2,083	0.08
4	Good	16,349	14,671	0.90
5	Good	13,628	5,330	0.39
6	Poor	13,541	5,603	0.41
7	Poor	3,159 (6,521)	803 (1,633)	0.25
8	Poor	8,767 (18,253)	2,231 (4,590)	0.25

This parameter correlates very well with the reported field performance and surface energy parameters, except for Mixture 3. Mixture 3 had the highest dry fatigue life; however, it had the lowest wet fatigue life. A possible reason for this poor resistance to moisture damage is the high angularity of the Mixture 3 quartzite particles as compared to those used in the other mixtures. Particles retained on the 0.3 mm sieve were analyzed for angularity using AIMS and are reported in Figure 34. Mixture 3 quartzite

has the highest angularity at 4396, while the Mixture 5 limestone is the least angular at 3048.

The Mixture 3 quartzite particles are 20 percent more angular than the next highest angular aggregate. This high aggregate angularity affect the n and E_1, as shown in Equation (49). It is believed that the high angularity of the aggregates in Mixture 3 contributed to the reduction in the resistance to moisture damage in the DMA.

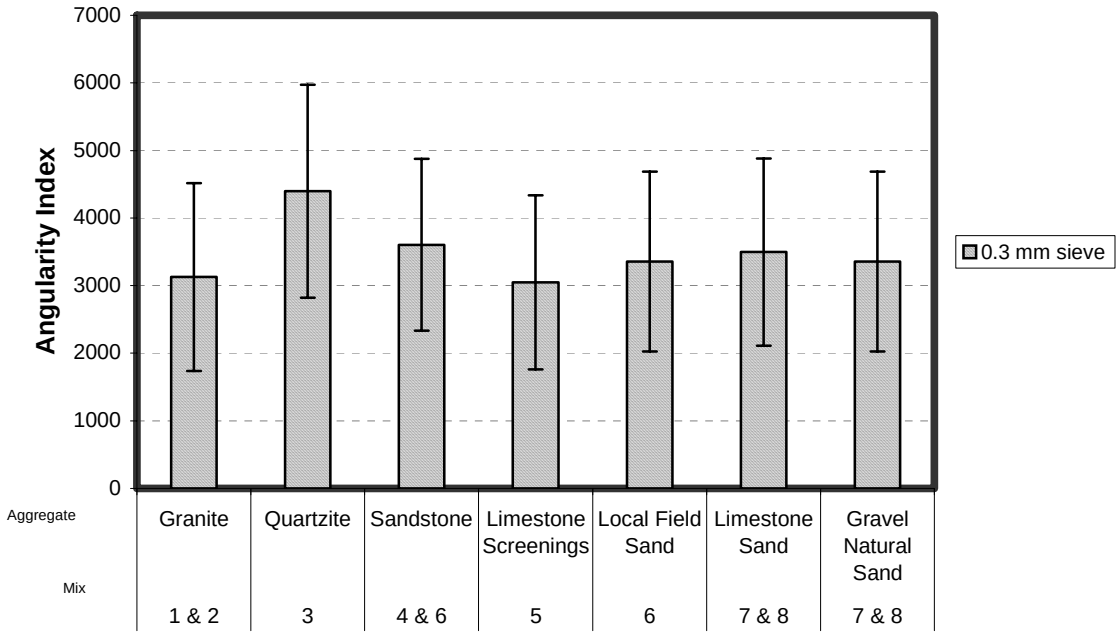

Figure 34. Fine Aggregate Angularity Index.

The second parameter is the ratio of the dynamic modulus at failure to the initial dynamic modulus. Table 19 shows the reduction in dynamic modulus at the fatigue life. This parameter captures the amount the mastic dynamic modulus can decrease while still accumulating damage. Typically the higher LVE dynamic modulus, the higher the reduced modulus at failure, and this is demonstrated in these data. Mixture 5 has the highest dry G'/G at 0.549 and the highest LVE dynamic modulus. Mixture 7 has the lowest dry reduced dynamic modulus at 0.387, yet the highest wet value of 0.672. Since

the Mixture 3 dry value is 0.448 and wet value is 0.608, the wet samples clearly failed prematurely, supporting the effect of high angularity as the cause. The lower the moisture damage parameter of Wet/Dry, the better the mixture resistance to moisture damage. Based on this parameter, Mixture 4 had the lowest value of 0.91 and Mixture 7 had the highest value of 1.74. The results in Table 19 indicate that the 50 percent reduction in stiffness, which is commonly taken as the threshold of damage, does not represent all materials.

Table 19. Mixture Rankings According to Reduction in Dynamic Modulus (G'/G) at Fatigue Life in Both Dry and Wet Conditions.

Mix	Reported Performance	G'/G at Fatigue Life		Wet / Dry
		Dry	Wet	
3	Good	0.44	0.60	1.36
4	Good	0.46	0.42	0.91
5	Good	0.54	0.62	1.14
6	Poor	0.37	0.40	1.08
7	Poor	0.38	0.67	1.74
8	Poor	0.43	0.49	1.16

Mechanistic Approach for Moisture Damage Evaluation

In addition to these parameters, a comprehensive evaluation of mixtures has been developed based on crack growth using Paris law. Paris law can be written in terms of the J integral of the dissipated pseudostrain energy as follows:

$$\frac{d\bar{r}}{dN} = A[J_R]^n \tag{39}$$

where, $\bar{r}$ is the average crack radius in the specimen, J_R is the J-integral, which is the pseudostrain energy release rate per unit crack area. J_R is defined in Equation (40):

$$J_R = \frac{\frac{\partial W_R}{\partial N}}{\frac{\partial (c.s.a)}{\partial N}} \tag{40}$$

where, W_R is the dissipated pseudostrain energy per unit volume of the intact material or the volume of the material that is capable of dissipating energy, c.s.a is the crack surface area, which is equal to $2\pi\bar{r}^2$ for a circular crack with radius equal to $\bar{r}$. W_R is estimated as the area in the hysteresis loop in the stress–pseudostrain domain divided by the volume of the intact material. This volume of intact material can be estimated using Equations (30) and (31) provided at the end of Chapter II, which relate the ratio of damaged modulus to initial modulus (G'/G) for cohesive and adhesive failures, respectively. The ratio of the damaged modulus to the initial modulus is a good estimate of the volume of the material that is intact and capable of dissipating energy during loading. G'/G is numerically equal to the pseudostiffness at a certain number of cycles to the initial pseudostiffness (C'/C). This ratio is the same as C(S), which is defined in Equation (25) of Chapter II. Therefore, W_R is defined in Equation (41) as the area of the hysteresis loop divided by C'/C or G'/G.

$$W_R = \frac{DPSE}{\frac{C'}{C}} \tag{41}$$

Integration of Equation (39) yields the following expression for the crack size as a function of loading cycles:

$$\bar{r}(N) = \left(\frac{2n+1}{n+1}\right)^{\frac{n+1}{2n+1}} \left(\frac{A}{(4\pi M)^n}\right)^{\frac{1}{2n+1}} \left(\int_{N=0}^{N} \left(\frac{\partial W_R}{\partial N}\right)^{\frac{n}{n+1}} dN\right)^{\frac{n+1}{2n+1}} \tag{42}$$

where, M is the number of cracks in a specimen. Based on the work of Schapery and Lytton, n is equal to 1/m for strain-controlled testing, where m is the exponent of time in the power law equation of the relaxation modulus as follows (*20, 50*):

$$E(t) = E_\infty + E_1 t^{-m} \tag{43}$$

Lytton et al. found that A can be expressed as follows (*50*):

$$A = k\left[\frac{E_R}{E_1 \Delta G_f - E_1 E_\infty E_R J_R}\right]^n \left(\frac{1}{\sigma_t^2 I_1}\right)^n \int_0^{\Delta t} (w(t))^n dt \tag{44}$$

where, k is a constant for a each material but varies only slightly between different materials, w(t) is a function that describes the shape of applied load as a function of time, σ_t is the tensile strength of the material, and I_1 is a parameter that describes the shape of the stress–strain curve under tensile stress. In this study, all specimens were subjected to the same sinusoidal loading function, so w(t) is the same for all dry and wet specimens. The term with E_∞ in Equation (41) is very small compared with the term $E_1\Delta G_f$ and hence can be ignored. In this study, E_R is computed by Equation (45):

$$E_R = \frac{\sigma_{\max}}{\varepsilon_{\max}} \tag{45}$$

where, σ_{max} is the maximum stress in the first cycle and ε_{max} is the maximum strain in the first cycle. Equation (44) can be written as:

$$A = K\left[\frac{E_R}{E_1\Delta G_f}\right]^n \tag{46}$$

where, K is a constant for each material that is inversely proportional to the square of the tensile strength of the asphalt mixes. σ_t and I_1 were not evaluated in this study and they are incorporated in the K parameter. In evaluating A, ΔG_f will be taken as the adhesive bond energy since most moisture damage is associated with adhesive failure. During this study, it was determined that W_R – Ln (N) is a linear relationship. Therefore, $\frac{\partial W_R}{\partial \ln N}$ is a constant for each specimen, which will be denoted "b." Therefore, Equation (42) can be written as:

$$\bar{r}(N) = K^{\frac{1}{2N+1}}(2n+1)^{\frac{n+1}{2n+1}}\left(\frac{A}{(4\pi M)^n}\right)^{\frac{n}{2n+1}} b^{\frac{n}{2n+1}} N_f^{\frac{1}{2n+1}} \tag{47}$$

$$\bar{r}(N) = K^{\frac{1}{2n+1}}(2n+1)^{\frac{n+1}{2n+1}}\left(\frac{E_R}{4\pi M E_1 \Delta G_f}\right)^{\frac{n}{2n+1}} b^{\frac{n}{2n+1}} N^{\frac{1}{2n+1}} \tag{48}$$

The number of cracks in a specimen is unknown. However, the influence of M cracks can be substituted for by an equivalent crack with radius equal to r. Hence, M can be

taken to be equal to 1. The focus will be on comparing the following term among the different mixes:

$$R = \frac{r(N)}{K^{\frac{1}{2n+1}}} = \left[(2n+1)^{n+1} \left(\frac{E_R b}{4\pi E_1 \Delta G_f} \right)^n N \right]^{\frac{1}{2n+1}} \quad (49)$$

Using the R parameter, which incorporates σ_t, is a conservative approach in estimating the change in crack growth under wet conditions compared to dry conditions. Wet specimens are expected to have less tensile strength, and the ratio $r(N)_{wet}/r(N)_{dry}$ is expected to be even higher than the ratio R_{wet}/R_{dry}.

These E_1 and m values used in Equation (49) are provided in Table 20 and were determined by performing a constant strain (within LVE range) relaxation test on each DMA mixture in both wet and dry conditions.

Table 20. Average E_1 and m Values.

Mixture	Conditioning	Average E_1 (Pa)	Average m
3	Dry	65,857,013	0.38
	Wet	36,736,124	0.26
4	Dry	40,916,094	0.34
	Wet	27,628,760	0.30
5	Dry	79,386,355	0.31
	Wet	57,642,775	0.23
6	Dry	23,879,412	0.42
	Wet	20,383,069	0.38
7	Dry	30,064,608	0.54
	Wet	34,080,074	0.37
8	Dry	12,091,724	0.45
	Wet	18,026,203	0.45

Equation (49) combines mix physical, chemical, and mechanical properties to calculate crack growth in dry and wet specimens. The bond energy used in Equation

(49) represents the "partial wet" condition. The dry bond energy values in Table 8 represent the condition where no moisture is present in the mix. However, the wet dry energy values represent the conditions where moisture is present at 100 percent of the aggregate-binder interface. During the wet test in DMA, water penetrates to more areas of the aggregate-binder interface and reduces the effective bond strength (partial wet bond energy). The value of the partial wet adhesive bond energy can be defined as a function of the ratio of the dynamic modulus under wet conditions to dynamic modulus under dry conditions, and by linear interpolation between the dry and wet bond energy values as follows (43):

$$\Delta G_{pw}^{a} = \frac{\left(\frac{G'}{G}\right)_{w}}{\left(\frac{G'}{G}\right)_{D}} \Delta G_{d}^{a} = \Delta G_{d}^{a}(1-P) + \Delta G_{w}^{a} P \qquad (50)$$

where, $\left(\frac{G'}{G}\right)_{w}$ is normalized dynamic modulus under wet condition at i th cycle, $\left(\frac{G'}{G}\right)_{D}$ is normalized pseudostiffness under dry condition at i th cycle, ΔG_{pw}^{a} is adhesive bond strength between asphalt and aggregate under partial wet condition, ΔG_{d}^{a} is adhesive bond strength between asphalt and aggregate under dry condition, ΔG_{w}^{a} is adhesive bond strength between asphalt and aggregate under wet condition, and P_i is percentage of surface area of the aggregate that is replaced by water in the mixture.

Table 21 provides the values of the slope (b) of dissipated pseudostrain energy per unit volume or Wr versus Ln (N), while Figure 35 illustrates a typical plot of W_R versus Ln (N). The slope of the dissipated pseudostrain energy per unit volume versus number of load cycles represents rate of damage accumulating in the specimen. The lower the Wr slope, the slower it will reach the fatigue life and stop accumulating damage. Since Mixtures 3 through 6 were tested at 0.3 percent strain and Mixtures 7 and 8 were tested at 0.2 percent strain, Equation (38) can be used to calculate b at 0.3 percent strain for Mixtures 7 and 8.

Table 21. Mixture Rankings According to Slope of DPSE (Wr) versus Ln (N) in Both Dry and Wet Conditions.

Mix	Slope of DPSE (W_r) vs. Ln (N)		Wet / Dry
	Dry	Wet	
3	136.3	141.6	1.04
4	129.6	130.7	1.01
5	145.7	105.5	0.72
6	117.1	143.9	1.23
7	150.3 (66.8)	171.2(76.1)	1.14
8	74.5(33.1)	180.5(80.2)	2.42

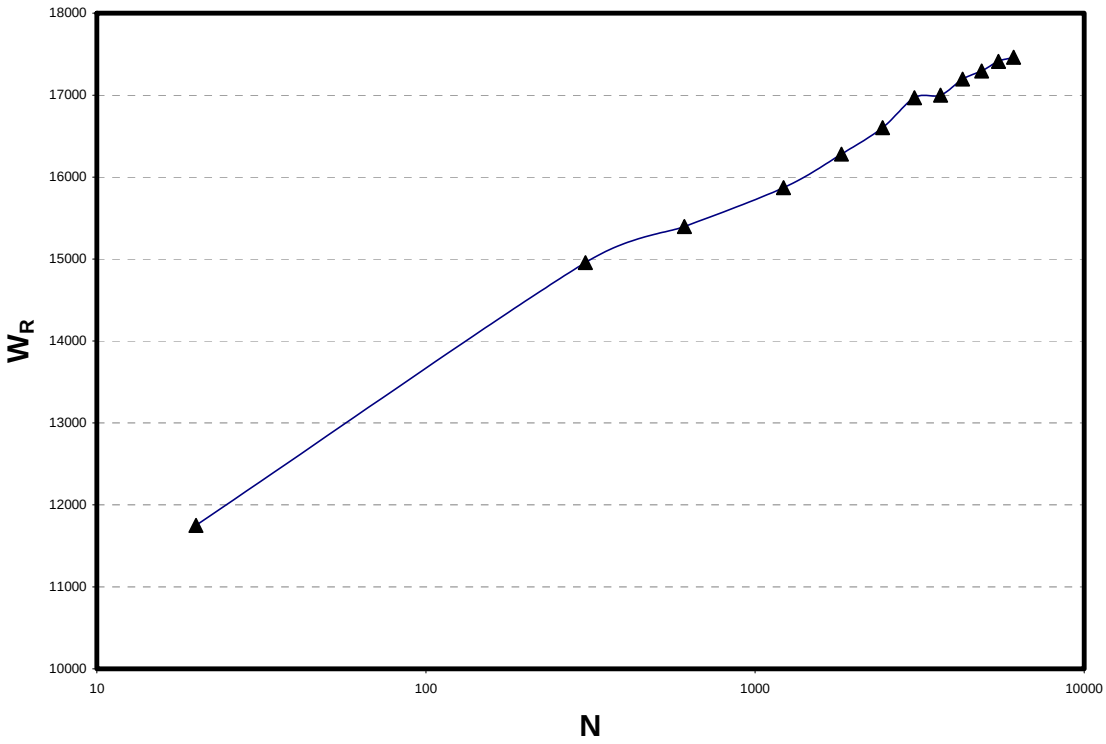

Figure 35. Typical Plot of Wr versus Ln (N).

Figures 36 and 37 show the results of using Equation (49) to evaluate each mixture in both wet and dry conditions using the mix chemical properties represented by the bond energy and physical and mechanical properties which are represented by the viscoelastic parameters E_1 and m (or n). It is evident that cracks propagate at a faster rate as the bond strength decreases in the moisture-conditioned samples. Since the binder type for Mixtures 3, 4, and 5 were the same, the adhesive bond strengths were similar, the difference in performance for Mixture 3 has to be due to the high angularity of the aggregate.

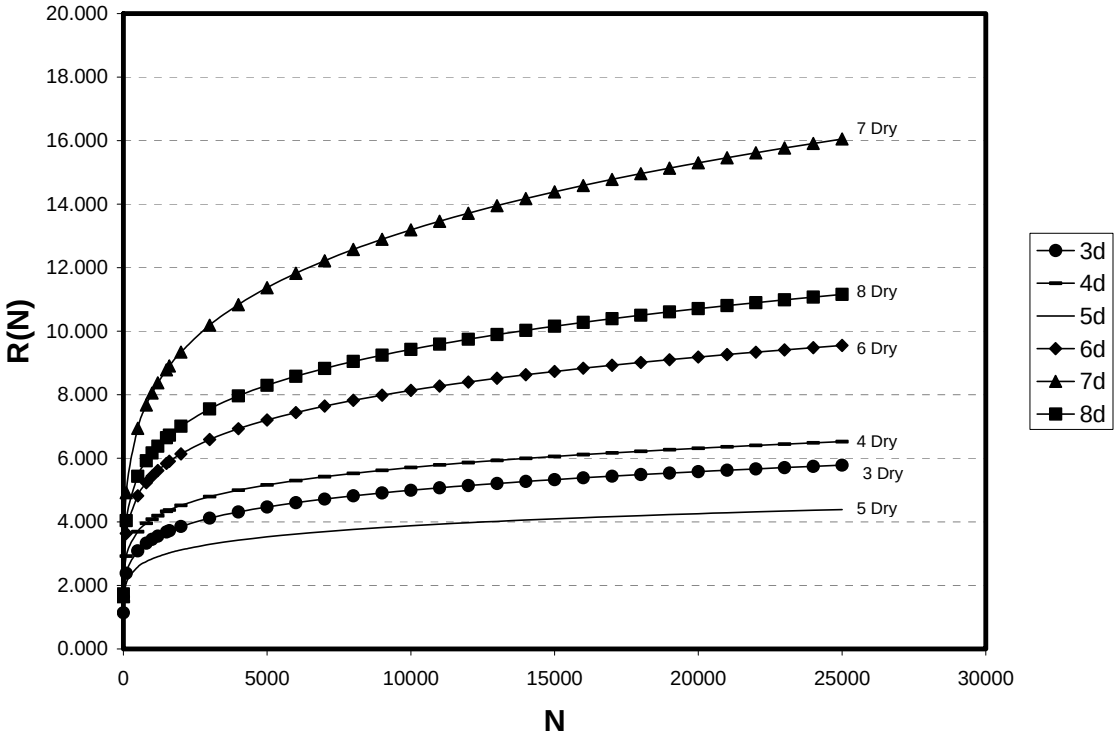

Figure 36. Plot of R(N) versus N for Dry Samples.

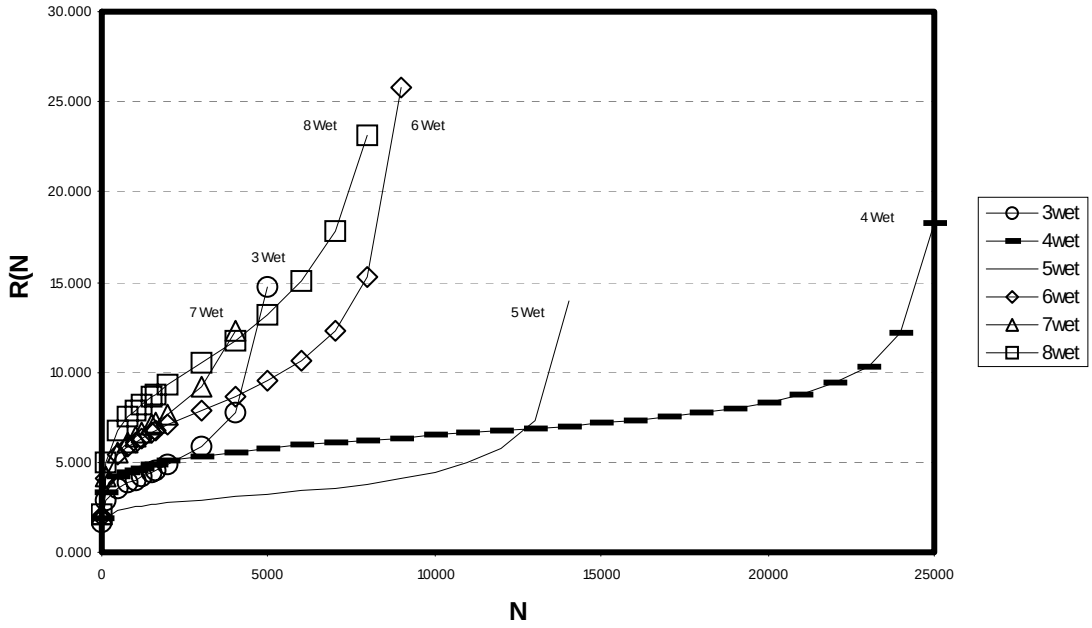

Figure 37. Plot of R(N) versus N for Wet Samples.

Sources of Dissipated Energy in DMA

During this study, Masad and Lytton developed a new method for decomposing DPSE into fracture energy and energy associated with permanent deformation. Under controlled-strain cyclic loading, a specimen accumulates permanent deformation in the first quarter of the loading cycle and eliminates this permanent deformation during the second quarter of the cycle to bring the specimen back to zero strain. This process is repeated in the third and fourth quarters of the loading cycle. This phenomenon leads to changes in the "apparent" lag between stress and strain. The word apparent is used here to differentiate between the lag angle in linear viscoelastic deformation and the lag caused by specimen damage. If the apparent lag is the same throughout the cycle, then DPSE can be described by the following equation:

$$W_R = \pi C' \varepsilon_{Ro}^2 \sin\left(\delta - \delta_{LVE}\right) / \left(C'/C\right) = \pi C \varepsilon_{Ro}^2 \sin\left(\delta - \delta_{LVE}\right) \quad (51)$$

However, the actual area inside the hysteresis loop is larger than the energy calculated using Equation (51). This confirms that δ is not the same throughout the loading cycle. Therefore, W_R can be expressed as follows:

$$W_R = W_{R1} + W_{R2} \tag{52}$$

$$W_{R1} = \pi C \varepsilon_{Ro}^2 \sin(\delta - \delta_{LVE}) \tag{53}$$

W_{R2} is the energy caused by the nonuniformity of the apparent lag angle due to permanent deformation. Figure 38 illustrates this by plotting W_R, W_{R1}, and W_{R2} and shows how permanent deformation energy is separated from fracture energy for each load cycle.

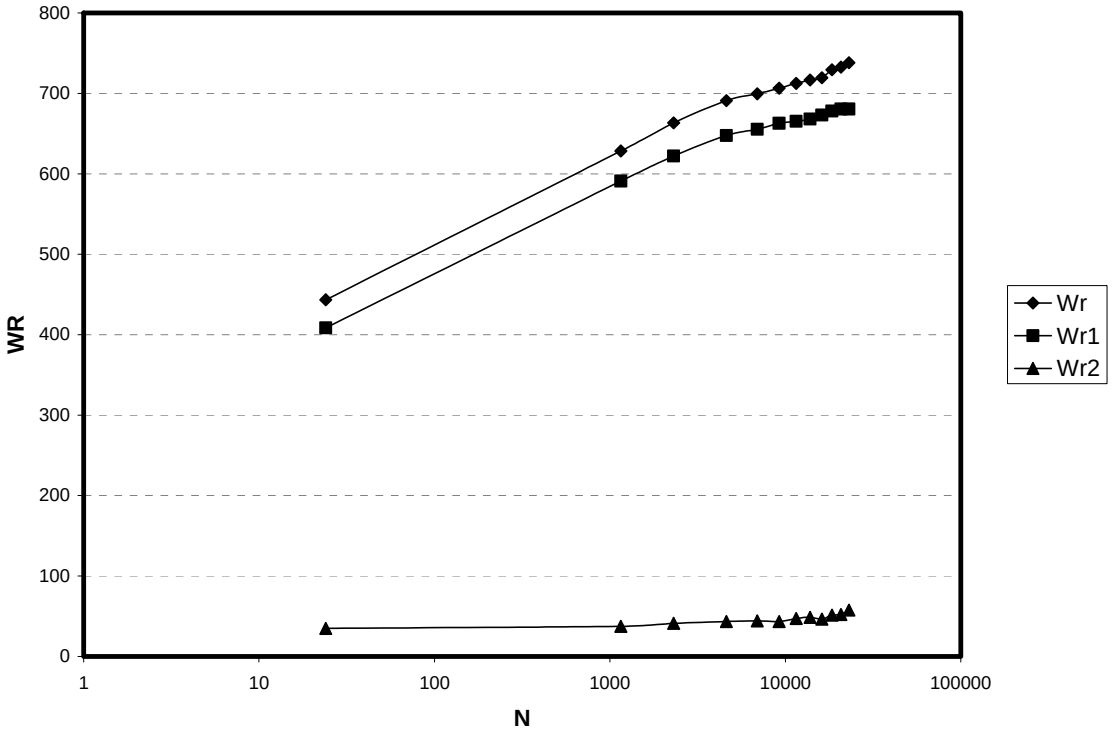

Figure 38. Typical Plot of W_R versus N Separating W_{R1} and W_{R2}.

Tables 22 and 23 present the data collected for the slope of phase angle and dynamic modulus versus Ln (N). The results in Tables 22 and 23 indicate that moisture damage

cannot be captured by changes in the phase angle or modulus only. As shown in Equation (52), a considerable amount of damage is attributed to W_{R2}, which reflects the nonuniformity of δ throughout loading due to the nonuniformity of the accumulation of permanent deformation during loading.

Table 22. Mixture Rankings According to Slope of Phase Angle versus Ln (N) in Both Dry and Wet Conditions.

Mix	Reported Performance	Slope of Phase Angle vs. Ln (N)		Wet / Dry
		Dry	Wet	
3	Good	1.69	1.56	0.92
4	Good	1.49	1.62	1.08
5	Good	1.58	1.02	0.64
6	Poor	1.26	1.60	1.27
7	Poor	2.05	1.85	0.90
8	Poor	1.23	1.99	1.62

Table 23. Mixture Rankings According to Slope of Dynamic Modulus (G*) versus Ln (N) in Both Dry and Wet Conditions.

Mix	Reported Performance	Slope of Modulus (G*) vs. Ln (N)		Wet / Dry
		Dry	Wet	
3	Good	-0.10	-0.10	1.03
4	Good	-0.09	-0.10	1.11
5	Good	-0.09	-0.08	0.89
6	Poor	-0.10	-0.11	1.16
7	Poor	-0.12	-0.10	0.87
8	Poor	0.09	0.11	1.29

HMA DYNAMIC MODULUS

The dynamic modulus test offers two main parameters: complex modulus and phase angle. According to the test protocol followed in this project, tests on each specimen yielded 24 (4 temperature × 6 frequency) complex moduli and phase angles. Complex modulus and phase angle of a given mixture and moisture conditioning were obtained by averaging results from three specimens.

Each set of dynamic modulus values obtained from different frequencies at different temperatures was converted into one single master curve. Master curves for each mixture are documented in Appendix F. Appendix F also provides the loading conditions (stress, temperature, and frequency) to keep the strain levels within the linear viscoelastic range between 50 and 150 microstrain. Table 24 shows the dynamic modulus values at the selected frequency of 10 Hz and temperature of 44.4°C for each specimen tested. Since the aim of this project is to test for moisture susceptibility, the researchers selected E*wet/E*dry as a moisture susceptibility parameter. The higher the value, the less susceptible the mix is to moisture.

Table 24. Average Dynamic Modulus Values at 10 Hz and 4.4°C for Both Wet and Dry Conditions.

Mix	Reported Performance	E* Dry Average (Pa)	E* Wet Average (Pa)	$\frac{E^*Wet}{E^*Dry}$
3	Good	18,348	15,660	0.853
4	Good	16,767	14,013	0.835
5	Good	19,067	16,627	0.872
6	Poor	17,747	15,333	0.864
7	Poor	12,494	8,389	0.671
8	Poor	11,429	8,169	0.714

As shown in Table 24, dynamic modulus ranks Mixtures 3, 4, 5, and 6 as good performers with comparable performance in terms of moisture susceptibility, while Mixtures 7 and 8 are clearly poor performers. These rankings are also comparable to the surface energy rankings for adhesive bond energy for both wet and dry conditions.

AGGREGATE CHARACTERIZATION

Aggregate images were captured and analyzed using AIMS. The image analysis was conducted on aggregates retained on a 0.3 mm sieve to represent fine aggregates and material retained on the 4.75 mm sieve to represent the coarse aggregates. Researchers analyzed the coarse aggregate images for the average values (index) and

standard deviations of angularity, shape, and texture, while the fine aggregates were analyzed for angularity. The data are shown in Figures 39 through 41.

For the aggregates retained on the 4.75 mm sieve, Mixture 1 and 2 granite aggregates have the highest angularity at 2595, while the Mixture 7 and 8 gravels are the least angular at 1860. Aggregates were also classified based on shape using the sphericity index. The lower the index, the more flat and elongated are the particles. For the aggregates retained on the 4.75 mm sieve, Mixture 5 gravel has the highest sphericity at 0.712, while Mixture 3 quartzite is the least spherical at 0.585. For the aggregates retained on the 4.75 mm sieve, Mixture 1 and 2 granite aggregates have the highest texture index at 251, while the Mixture 7 and 8 gravels have the least texture at 73.

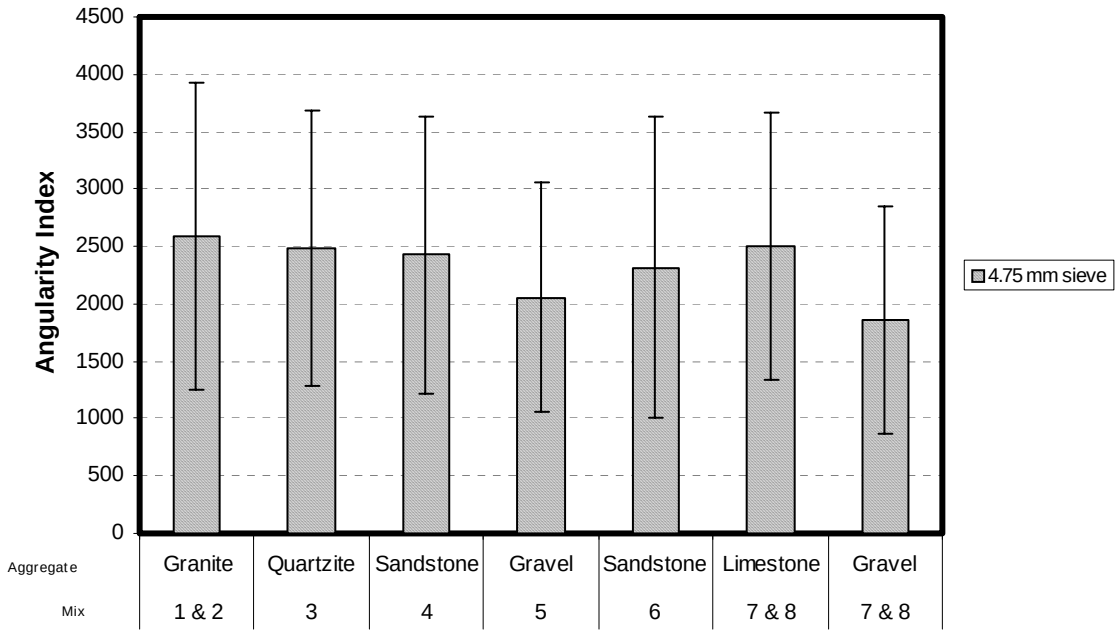

Figure 39. Coarse Aggregate Angularity Index.

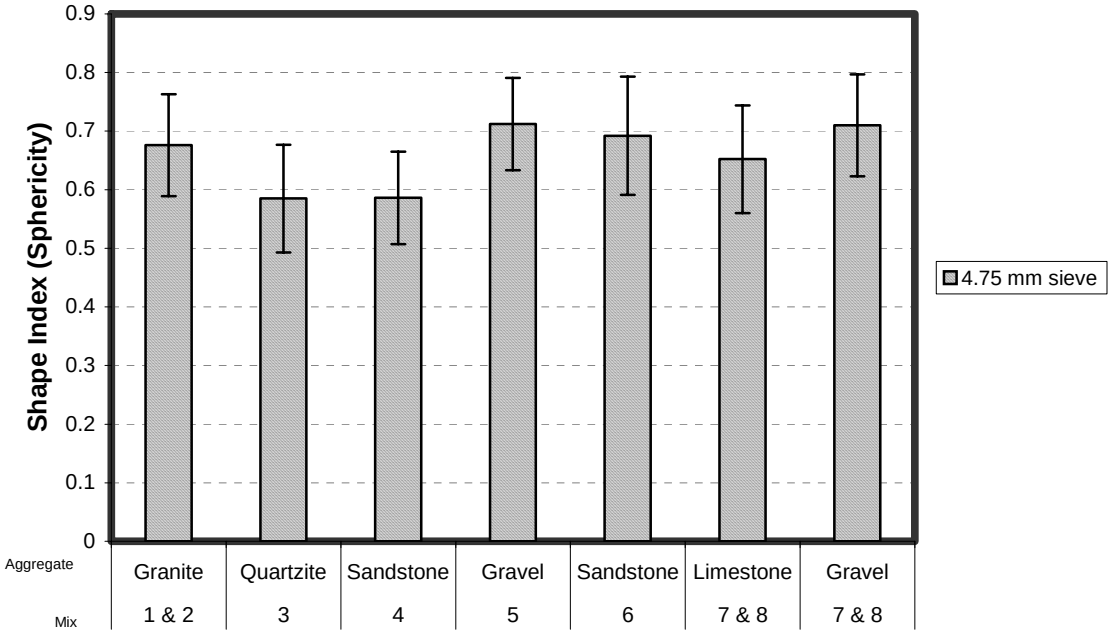

Figure 40. Coarse Aggregate Shape Index.

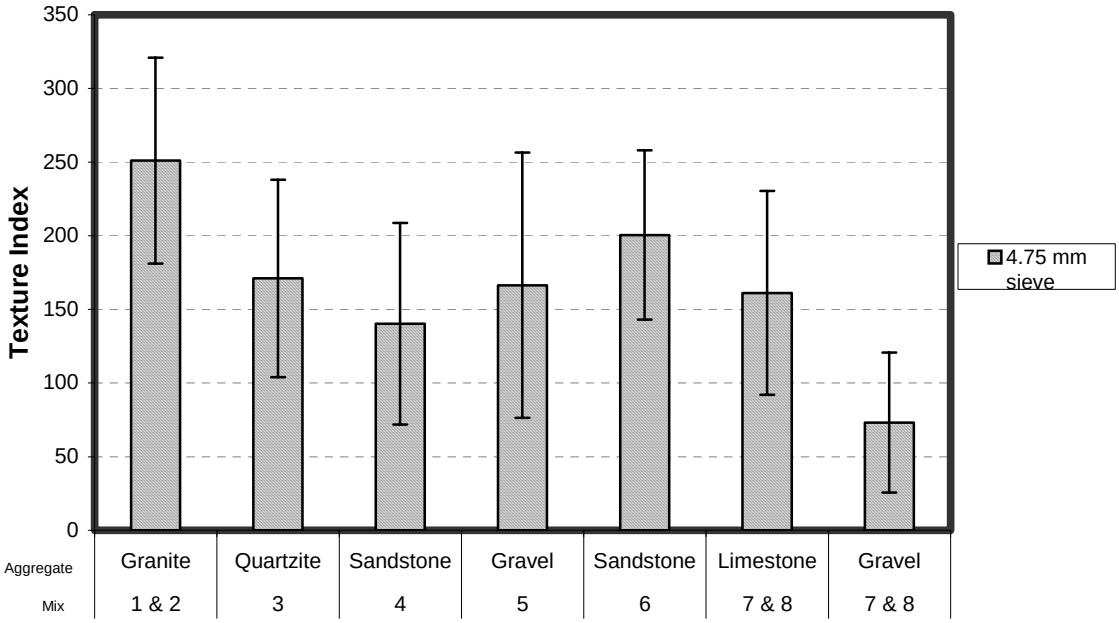

Figure 41. Coarse Aggregate Texture Index.

CHAPTER V
CONCLUSIONS AND RECOMMENDATIONS

Moisture damage in asphalt mixes has become a prevalent problem for most highway agencies. Many state agencies have decided moisture damage in asphalt pavements can be reduced by developing a reliable test to predict moisture susceptibility. This research focused on developing an approach to evaluate the susceptibility of aggregates and asphalts to moisture damage by understanding the micro-mechanisms that influence the adhesive bond between aggregates and asphalt and the cohesive strength and durability of the asphalt. The developed approach was used to evaluate six asphalt mixtures from Texas and Ohio that have performed either well or poorly in the field. The results were compared to actual reported field performance and further used to predict which combinations of asphalt and aggregate will produce superior in-service performance. A summary of the work accomplished in this study and main findings is presented in this chapter along with procedures that can be used to select the optimum combinations of aggregates and binders that will reduce moisture susceptibility.

Surface energy of aggregates was measured using the Universal Sorption Device (USD), while surface energy of binder was measured using the Wilhelmy Plate. Practical procedures for measuring surface energy using these two devices were developed and included in the appendices of this report. The ratio of the adhesive bond energy under wet condition to the adhesive bond energy under dry condition ($\Delta G^{aW}/\Delta G^{aD}$) can be used to identify possible problematic combinations of aggregates and binder. Based on the wetting bond energy, a ratio ($\Delta G^{aW}/\Delta G^{aD}$) higher than -1.2 seems to separate the good from the poor combinations of materials based on resistance to moisture damage.

This study developed an experimental protocol to evaluate the susceptibility of asphalt mixes to moisture damage using the Dynamic Mechanical Analyzer (DMA). The protocol includes sample preparation, testing method, and data analysis. The ratio of the number of cycles to failure under wet conditions to the number of cycles to failure

under dry condition $N_{f(wet)}/N_{f(dry)}$ indicated that Mixtures 7 and 8 have poor resistance to moisture damage while Mixtures 4 and 5 have good resistance to moisture damage. Mixture 6 was originally considered to have poor resistance to moisture damage, but it was shown by the $N_{f(wet)}/N_{f(dry)}$ to exhibit good resistance. Consulting with the field engineers revealed that the moisture damage in this mixture was not consistent throughout the pavement section and can be attributed to construction issues that are not related to material properties. Based on the $N_{f(wet)}/N_{f(dry)}$ ratio, Mixture 3 is at risk of exhibiting moisture-related damage.

The ratio of shear modulus at failure to initial shear modulus (G'/G) showed that mixes with poor resistance to moisture damage failed at higher ratios than the mixes with good resistance to moisture damage. The results indicate that failure cannot be defined by a fixed value for the reduction in stiffness as is typically done in evaluating fatigue failure by 50 percent reduction in stiffness.

Analysis of the DMA results showed that the actual dissipated pseudostrain energy (DPSE) should be calculated as the area of the hysteresis loop divided by the volume of intact material that is capable of transferring stresses. It has been shown using the principles of micromechanics that the volume of intact material can be represented by the ratio of shear stiffness at any cycle to the original shear stiffness. Also, it was found that the DPSE or W_R cannot be calculated by the equation that assumes damage to be represented by changes in viscoelastic properties only (W_{R1}). The accumulation of permanent deformation is not uniform throughout loading, and this leads to nonuniform values for δ during a loading cycle. The apparent δ value provided by DMA is quantified at the peak of the loading cycle.

A comprehensive methodology based on Paris law was developed in this study to estimate the crack growth as a function of number of cycles. This methodology considers the fact that moisture damage is a function of different chemical and physical properties. This methodology incorporates chemical properties of the mix (bond energy), mechanical properties (compliance and the rate of accumulation of DPSE), and the tensile strength of the mix. The mechanical properties are influenced by the physical

properties of the mix constituents such as aggregate gradation and shape and film thickness. This methodology clearly captures the influence of moisture on crack growth. It is also capable of separating the good-performing mixes from the poor-performing mixes.

The dynamic modulus master curve for each mixture for both wet and dry conditions was determined by applying a sinusoidal axial compressive stress to an HMA specimen at different temperatures and loading frequencies. The parameter relating laboratory testing and field performance moisture susceptibility best was E*wet/E*dry. These rankings were also comparable to the bond energy rankings for adhesive bond energy for both wet and dry conditions.

FUTURE RESEARCH

While conducting the laboratory testing and data analysis, the following issues surfaced that suggested further research or improvement:

- Establish a relationship between aggregate mineralogy and surface energy. This relationship can be used to determine the surface energy of an aggregate once its mineralogy is determined. A composite model is needed to obtain the aggregate surface energy from the mineral's surface energy and volumetric concentration.
- Future studies in DMA need to use a higher percentage of binder than that used in this study. In some cases, the specimens used in this study were too stiff for the DMA to load to the desired strain level.
- The experimental and analysis methods used in this study need to be applied to wide variations of materials to better establish the relationship between bond energy and DMA results.
- The analysis methods presented in this study should be applied to asphalt mixes to verify the findings from the DMA testing of asphalt mastics.

REFERENCES

1. *Our Nation's Highways: Selected Facts and Figures 2000*, Publication No. FHWA-PL-011012. Office of Highway Policy Information, Federal Highway Administration, U.S. Department of Transportation, Washington, D.C., 2000.

2. Hicks, R.G. NCHRP *Synthesis of Highway Practice 175: Moisture Damage in Asphalt Concrete.* Transportation Research Board, National Research Council, Washington, D.C., Oct. 1991, 90 pp.

3. Fromm, H.J. The Mechanisms of Asphalt Stripping from Aggregate Surfaces. *Proceedings, Association of Asphalt Paving Technologists*, Vol. 43, 1974, pp. 191-223.

4. Taylor, M.A., and N.P. Khosla. Stripping of Asphalt Pavements: State of the Art. *Transportation Research Record 911*, 1983, pp. 150-158.

5. Liu, M.J., and T.W. Kennedy. *Field Evaluation of Stripping and Moisture Damage in Asphalt Pavements Treated with Lime and Anti-Stripping Agents*. Center for Transportation Research, Research Report 441-2F, Austin, Texas 1991.

6. Thelen, E. Surface Energy and Adhesion Properties of Asphalt-Aggregate Systems. *Highway Research Record Bulletin 192*, Highway Research Board, National Research Council, Washington, D.C., 1958, pp. 63-74.

7. Majidzadeh, K., and F.N. Brovold. *Effect of Water on Bitumen-Aggregate Mixtures.* Report CE-1, University of Florida, Gainsville, Florida, Sept. 1966.

8. Scott, J.A.N. Adhesion and Disbonding Mechanisms of Asphalt Used in Highway Construction and Maintenance. *Proceedings, Association of Asphalt Paving Technologists*, Vol. 47, 1978, pp. 19-48.

9. Castelblanco, A., E. Masad, and B. Birgisson. HMA Moisture Damage as a Function of Air Void Size Distribution, Pore Pressure and Bond Energy. *Journal of Testing and Evaluation*, ASTM, submitted for publication, October 2004.

10. Lottman, R.P. Predicting Moisture-Induced Damage to Asphaltic Concrete-Field Evaluation. *NCHRP Report 246*, Transportation Research Board, National Research Council, Washington, D.C., 1982.

11. *Resistance of Compacted Asphalt Mixtures to Moisture-Induced Damage*, Test Method T283-02. AASHTO, Part II-Methods of Sampling and Testing, Washington, D.C., 2003.

12. Marek, C.R., and M. Herrin. Tensile Behavior and Failure Characteristics of Asphalt Cements in Thin Films. *Proceedings, Association of Asphalt Paving Technologists*, Vol. 37, 1968, pp. 386-421.

13. R.L. Lytton. *Adhesive Fracture in Asphalt Concrete Mixtures*. In J. Youtcheff (Ed.), submitted for publication, 2004.

14. A.V. Pocius. *Adhesion and Adhesives Technology*. Hanser/Gardner Publications, Inc., Columbus, Ohio 1997.

15. McBain, J.W., and D.G. Hopkins. On Adhesives and Adhesive Action. *Journal of Physical Chemistry*, Vol. 29, 1925, p. 294.

16. McBain, J.W., and D.G. Hopkins. *Adhesives and Adhesive Action.* Appendix IV, Second Report of the Adhesive Research Committee, London: Dept. of Scientific and Industrial Research, 1929.

17. Masad, E. *The Development of a Computer Controlled Image Analysis System for Measuring Aggregate Shape Properties*. National Cooperative Highway Research Program NCHRP-IDEA Project 77 Final Report, Transportation Research Board, National Research Council, Washington, D.C., 2003.

18. Masad, E., D.N. Little, and R. Sukhwani. Sensitivity of HMA Performance to Aggregate Shape Measured Using Conventional and Image Analysis Procedures. *Journal of Materials in Civil Engineering,* American Society of Civil Engineers, 2004.

19. Masad, E., L. Tashman, D.N. Little, and H. Zbib. Viscoplastic Modeling of Asphalt Mixes with the Effects of Anisotropy, Damage and Aggregate Characteristics. *International Journal of Road Materials and Pavement Designs,* Vol. 5, No. 4, 2004, pp. 477-498.

20. Schapery, R.A. Correspondence Principles and a Generalized J Integral for Large Deformation and Fracture Analysis of Viscoelastic Media. *International Journal of Fracture*, Vol. 25, 1984, pp.194-223.

21. Hefer, A.W., D.N. Little, and R.L. Lytton. A Synthesis of Theories and Mechanisms of Bitumen-Aggregate Adhesion Including Recent Advances in Quantifying the Effects of Water. *Submitted for Publication in Association of Asphalt Paving Technologist*.

22. Fowkes, F.M., Attractive Forces at Interfaces. *Industrial Engineering & Chemistry*, Vol. 56 (12), 1964, pp. 40-52.

23. Van Oss, C.J., M.K. Chaudhury, and R.J. Good. Interfacial Lifshitz-van der Waals and Polar Interactions in Macroscopic Systems. *Chemical Review*, Vol. 88, 1988, p. 927.

24. Good, R.J., and C.J. Van Oss. The Modern Theory of Contact Angles and the Hydrogen Bond Component of Surface Energies. In M.E. Schrader and G. Loeb (Eds.), *Modern Approach to Wettability: Theory and Applications*, Plenum Press, New York, 1991, pp. 1-27.

25. Lytton, R.L. Characterizing Asphalt Pavements for Performance. *Transportation Research Record 1723*, Transportation Research Board, National Research Council, Washington, D.C., 2000, pp. 5-16.

26. Cheng, D., D.N. Little, R.L. Lytton, and J. Holste. Use of Surface Free Energy Properties of the Asphalt-Aggregate System to Predict Moisture Damage Potential. *Journal of the Association of Asphalt Paving Technologists*, Vol. 71, 2002, pp. 59-88.

27. Al-Omari, A., L. Tashman, E. Masad, A. Cooley, and T. Harman. Proposed Methodology for Predicting HMA Permeability. *Journal of the Association of Asphalt Paving Technologists*, Vol. 71, 2002, pp. 30-58.

28. Hicks, R.G., F.N. Finn, C.L. Monismith, and R.B. Leahy. Validation of SHRP Binder Specification through Mix Testing. *Journal of the Association of Asphalt Paving Technologists*, Vol. 62, 1993, pp. 565-614.

29. Rowe, G.M. Performance of Asphalt Mixtures in the Trapezoidal Fatigue Test. *Journal of the Association of Asphalt Paving Technologists*, Vol. 62, 1993, pp. 344-384.

30. Rowe, G.M., and M.G. Bouldin. Improved Techniques to Evaluate Fatigue Resistance of Asphaltic Mixes. *Proc., 2nd Enraphalt and Eurobitume Congress*, Barcelona, 2000.

31. Reese, R. Properties of Aged Asphalt Binder Related to Asphalt Concrete Life. *Journal of the Association of Asphalt Paving Technologists*, Vol. 66, 1997, pp. 604-632.

32. Kim, Y. R.. *Mechanistic Fatigue Characterization and Damage Modeling of Asphalt Mixtures.* Ph.D. Dissertation, Texas A&M University, College Station, Texas, 2003.

33. Kim, Y.R., D.N. Little, and R.L. Lytton. Fatigue and Healing Characterization of Asphalt Mixtures. *Journal of Materials in Civil Engineering*, American Society of Civil Engineers, Vol. 15, No. 1, 2003, pp 75-83.

34. Song, I., D.N. Little, E. Masad, and R.L. Lytton. Comprehensive Evaluation of Damage in Asphalt Mastics Using X-ray CT, Continuum Mechanics, and Micromechanics. *Submitted for Publication in Association of Asphalt Paving Technologists*.

35. Kim, Y.R., D.N. Little, and I. Song. Effect of Mineral Fillers on Fatigue Resistance and Fundamental Material Characteristics: Mechanistic Evaluation. T*ransportation Research Record 1832*, Transportation Research Board, National Research Council, Washington, D.C., 2003, pp. 1-8.

36. Kim, Y.R., H.J. Lee, and D.N. Little. Fatigue Characterization of Asphalt Concrete Using Viscoelasticity and Continuum Damage Theory. *Journal of the Association of Asphalt Paving Technologists*, Vol. 66, 1997, pp. 520-569.

37. Si, Z. *Characterization of Microdamage and Healing of Asphalt Concrete Mixtures*. Ph.D. Dissertation, Texas A&M University, College Station, Texas, 2001

38. Chowdhury, A., A. Bhasin, and J.W. Button. *As-Built Properties of Test Pavements on IH-20 in Atlanta District*. Texas Department of Transportation, FHWA/TX-034203-2, College Station, Texas March 2003

39. Miles Garrison, Personal Communication, 2004.

40. District 3 Pavement Performance Team. *Summary Report*. Ohio Department of Transportation, Columbus, Ohio, February 27, 2003.

41. Cheng, D. *Surface Free Energy of Asphalt-Aggregate System and Performance Analysis of Asphalt Concrete Based on Surface Free Energy*. Ph.D. Dissertation, Texas A&M University, College Station, Texas, 2002.

42. Hefer, A.W. *Adhesion in Bitumen-Aggregate Systems and Quantification of the Effects of Water on the Adhesive Bond.* Ph.D. Dissertation, Texas A&M University, College Station, Texas, 2004.

43. Kim, Y.R., D.N. Little, and R.L. Lytton. Effect of Moisture Damage on Material Properties and Fatigue Resistance of Asphalt Mixtures. *Annual Meeting of Transportation Research Board*, Washington, D.C., 2004.

44. *Determining Dynamic Modulus of Hot-Mix Asphalt Concrete Mixtures*, Test Method TP 62-03. AASHTO, Part II-Methods of Sampling and Testing, Washington, D.C., 2003.

45. *Preparing and Determining the Density of Hot-Mix Asphalt Specimens by Means of the Superpave Gyratory Compactor*, Test Method T 312-01. AASHTO, Part II-Methods of Sampling and Testing, Washington, D.C., 2003.

46. *Compacting Specimens Using Texas Gyratory Compactor*, Test Method Tex 206-F. Texas Department of Transportation, Bituminous Test Procedures Manual, Chapter 8, Austin, Texas, 2004.

47. *Resistance of Compacted Asphalt Mixtures to Moisture-Induced Damage*, Test Method T 283-02. AASHTO, Part II-Methods of Sampling and Testing, Washington, D.C., 2003.

48. Witczak, M.W., K. Kaloush, T.K. Pellinen, M. El-Basyouny, and H. Von Quintus. Simple Performance Test for Superpave Mix Design. *NCHRP Report 465*, National Cooperative Highway Research Program, Washington, D.C. 2002.

49. Masad, E.A. *Aggregate Imaging System (AIMS): Basics and Applications*. Texas Department of Transportation, FHWA/TX-05/5-1707-01-1, Austin, Texas, November 2004.

50. Lytton, R.L., J. Uzan, E.G. Fernando, R. Roque, D. Hiltmen, and S. Stoffels. Development and Validation of Performance Prediction Models and Specifications for Asphalt Binders and Paving Mixtures. *SHRP Report No. A-357*, Strategic Highway Research Program, National Research Council, Washington, D.C., 1993.

APPENDIX A

INTRODUCTION

Surface energy of solids is of great importance for many industrial and engineering applications, from pharmaceutical research to the paper-making industry. The surface free energy of a solid surface gives a direct measure of intermolecular interactions at interfaces and has a strong influence on wetting, adsorption, and adhesion behavior. Adhesion to solid surfaces can be desirable or undesirable depending on the context. Surface free energy is thus of interest in many areas. In the areas of paints, coating, adhesives, and certain biotechnology applications good adhesion to substrates is required. In contrast, there are many areas where adhesion is undesirable, especially fouling or biofilm on solid surfaces (Zhao et al. 2004). It is also an important factor in oil recovery because it is the key parameter in determining wettability, which controls the distribution of fluids in reservoir porous media. (Medout-Marere et al. 1998).

Now, it is widely accepted that adhesion is controlled by several interfacial interaction forces. The summation of these interfacial interactions is the thermodynamic work of adhesion or the interfacial interaction energy, which quantifies the energy available for adhesion based on the energetic properties of two interacting surfaces (Brant and Childress 2004). Although surface free energy applications have been used in many engineering applications for some years with great success, its application in Civil Engineering materials, especially in the area of asphalt concrete materials, is very new. Surface energies play a vital role in adhesion and in understanding theories of adhesion. Even small changes in their values can cause large changes in practical measured adhesion (Packham 1996).

BACKGROUND

The atoms at the external surface of a liquid or solid are in a very different environment compared to those atoms buried inside the material. This difference arises from the asymmetrical environment; in the bulk material, each atom is surrounded by

similar atoms, while those at the surface see this only on one side of the interface. In addition, the various influencing factors exerted by the environment act only on the outermost atoms. These atoms, as a consequence, have a different distribution from those inside, causing a different energy at the surface, which is what one wants to measure.

When two condensed materials are in intimate contact across an interface, the surface atoms of each are able to interact across the interface. Any understanding of the interfacial free energy or the interfacial tension ultimately rests on an accurate understanding of the types of interactions which exist across the interface. Part of this interaction is electrodynamic (i.e., pertaining to van der Waals interactions) and has been recognized for a century or more. Recognition of other types of interaction has occurred more recently, the major one involving the noncovalent sharing of electrons across the interface. This noncovalent bonding is part of the Lewis acid-base (AB) description, which is widespread in modern chemistry.

Until the middle 1980s, van der Waals attractions and electrostatic repulsions were considered the only two forces acting between particles, even when immersed in a polar liquid such as water. The three kinds of van der Waals forces are dispersion (or van der Waals – London), induction (or van der Waals – Debye), and orientation (or van der Waals – Keesom) forces. However, although the existence of these forces was well known, there was difficulty explaining the distinctions between apolar and polar forces with the van der Waals interactions alone. Chaudhury (1984) applied Lifshitz' theory to macroscopic-scale colloid interactions and established for the first time a clear distinction between apolar, Lifshitz–Van der Waals (LW), and polar, electron-acceptor and electron-donor, or Lewis acid-base (AB) interactions. Once this distinction had become obvious, it quickly found its place in surface science applications (van Oss et al. 1987). The interfacial interactions between materials are now mainly composed of both apolar (LW) and polar (AB) interactions and may also include electrostatic (EL) interactions (van Oss et al. 1988).

While for EL contributions the measurement methodology is an electrokinetic one, for LW and AB interactions together the methods of choice remain the determination of contact angles, with the Wihelmy plate apparatus, of appropriate, relatively high-energy liquids, apolar (e.g., diiodomethane) as well as polar (e.g., water, glycerol, formamide), and the determination of vapor pressure isotherms with the Universal Sorption Device (USD) of appropriate liquids of nHexane, MPK, and water, deposited on solid surfaces.

The net interfacial interaction is formulated as the value of ΔG, and the sign indicates whether there is a net attraction (negative sign) or a net repulsion (positive sign), according to the usual convention of chemical thermodynamics. Interfacial interaction energies between various identical or different materials, taking place in water, are given as ΔG_{1w1}^{IF} and ΔG_{1w2}^{IF}, respectively. These represent either hydrophobic attraction (when $\Delta G^{IF} < 0$) or hydrophilic repulsion (when $\Delta G^{IF} > 0$). Compared with AB interactions occurring in water, Lifshitz-van der Waals (LW) interactions provide only a minor contribution to the interfacial free energies, ΔG_{1w1}^{IF} or ΔG_{1w2}^{IF}, as do electrostatic interactions (EL), which, however, for practical reasons are considered separately from interfacial (IF) interactions (Giese and van Oss 2002).

van der Waals first observed that there are noncovalent interactions between uncharged atoms and molecules. For two atoms or molecules (i) separated by a short distance in vacuum, the dispersion interaction can be expressed as:

$$A_{ii} = \pi^2 q_i^2 \beta_{ii} \tag{A-1}$$

where, A is the Hamaker constant, q is the number of atoms per unit volume, and β is a constant. When two or more different materials interact, the total Hamaker constant is determined by a geometric rule:

$$A_{ij} = \sqrt{A_{ii} A_{jj}} \tag{A-2}$$

For two atoms of the same material, 1, in medium 3 (e.g., two individual aggregate particles in liquid water) the combining rule gives:

$$A_{131} = \left(\sqrt{A_{11}} - \sqrt{A_{33}}\right)^2 \text{ or } A_{131} = A_{11} + A_{33} - 2A_{13} \qquad \text{(A-3)}$$

Here the two aggregate or clay particles (1) are interacting through liquid water (3). For two different materials (1 and 2), in medium 3:

$$A_{132} = \left(\sqrt{A_{11}} - \sqrt{A_{33}}\right)\left(\sqrt{A_{22}} - \sqrt{A_{33}}\right) \text{ or } A_{132} = A_{12} + A_{33} - A_{13} - A_{23} \qquad \text{(A-4)}$$

Here the subscript 1 may represent aggregates and subscript 2 may denote asphalt interacting in liquid water. For the case where a material is embedded in another material, the Hamaker constant, A_{131}, always is positive (or zero); for two different materials, the Hamaker constant, A_{132}, can be negative, i.e., when:

$A_{11} > A_{33} > A_{22}$ and when: $A_{11} < A_{33} < A_{22}$

All of these considerations initially only applied to van der Waals – London interactions, using the Hamaker constant combining rules. The surface thermodynamic approach for obtaining Equations (3) and (4) is essentially the same as Hamaker's approach, as long as Equation (2) is valid (Giese and van Oss 2002).

Lifshitz approached the problem of the van der Waals interaction by examining the macroscopic properties of materials, as opposed to the Hamaker treatment of summing individual atomic interactions (Rytov 1959). This gives an approximate expression for the free energy of interaction between two different (1 and 2) semi-infinite surfaces separated by a third material (3). Following Lifshitz, Chaudhury (1984) showed that three types of van der Waals forces can be treated in the same manner so that they can be lumped together as a single term, the "apolar" term.

The surface tension (γ_i), i.e., the surface free energy per unit area, of a liquid in vacuum is equal to one-half the free energy of cohesion (ΔG_{ii}), and is opposite in sign (Good 1967):

$$\gamma_i = -\frac{1}{2}\Delta G_{ii} \tag{A-5}$$

For solids, Equation (4) is equally true, but solids differ from liquids in that ΔG_{ii} is not their free energy of cohesion, just the free energy available for interacting with liquids (Giese et al. 1996). If the contributors to ΔG_{ii} are independent, as is commonly assumed, then it follows that the surface tension is composed of independent contributors, each of which can be treated separately (Fowkes 1963). For purely Lifshitz – van der Waals interactions (LW), the interfacial LW component of the surface tension for two materials, 1 and 2, can be obtained from the LW surface tension components of each by application of the Good-Grifalco-Fowkes combining rule:

$$\gamma_{12}^{LW} = \left(\sqrt{\gamma_1^{LW}} - \sqrt{\gamma_2^{LW}}\right)^2 \text{ or } \gamma_{12}^{LW} = \gamma_1^{LW} + \gamma_2^{LW} - 2\sqrt{\gamma_1^{LW}\gamma_2^{LW}} \tag{A-6}$$

The apolar component of the free energy of cohesion of material 1 is:

$$\Delta G_{11}^{LW} = -2\gamma_1^{LW} \tag{A-7}$$

and the free energy of interaction between two materials is related to the surface tensions of these materials by the Dupre equation:

$$\Delta G_{12}^{LW} = \gamma_{12}^{LW} - \gamma_1^{LW} - \gamma_2^{LW} \tag{A-8}$$

For two similar materials (1) immersed in a liquid (2), the relation is:

$$\Delta G_{121}^{LW} = -2\gamma_{12}^{LW} \tag{A-9}$$

and two different materials (1 and 2) immersed in a liquid (3) are related to the interfacial tensions by:

$$\Delta G_{132}^{LW} = \gamma_{12}^{LW} - \gamma_{13}^{LW} - \gamma_{23}^{LW} \tag{A-10}$$

The free energy of interaction between materials 1 and 2 is related by:

$$\Delta G_{12}^{LW} = -2\sqrt{\gamma_1^{LW}\gamma_2^{LW}} \tag{A-11}$$

Using Eqs. 6 and 8 to expand the interfacial surface tensions in Eq. (10) gives:

$$\Delta G_{132}^{LW} = -\gamma_3^{LW} - 2\sqrt{\gamma_1^{LW}\gamma_2^{LW}} + 2\sqrt{\gamma_1^{LW}\gamma_3^{LW}} + 2\sqrt{\gamma_2^{LW}\gamma_3^{LW}} \tag{A-12}$$

It follows from Eq. (12) that:

$$\Delta G_{132}^{LW} = \Delta G_{33}^{LW} + \Delta G_{12}^{LW} - \Delta G_{13}^{LW} - \Delta G_{23}^{LW} \tag{A-13}$$

which is the confirmation of the Hamaker combining rule (Eq. 4) obtained by a surface thermodynamic approach, based on the applicability of the geometric mean combining rule to LW interactions.

For some time it was thought that the Keesom dipole-dipole interactions should be treated separately from the Debye and London interactions (Giese and van Oss 2002). Because of the dipolar nature of the Keesom phenomenon, the term “polar” was applied to these interactions, in contrast to the “apolar” Debye and London interactions. This distinction between all three apolar electrodynamics forced a search for the true polar

interactions. After Chaudhury (1984) showed that three apolar electrodynamic forces are simply additive and should be treated as a single term, the LW interactions, it became possible to examine the nature of the polar (Lewis) properties of surfaces as an entirely separate phenomenon from their electrodynamic (LW) properties.

In aqueous media, and especially for solid surfaces that are rich in oxygen such as silicate minerals, the principal polar interaction is hydrogen bonding, involving donors and acceptors. Moreover, polar surface interactions are restricted to hydrogen bonding, so that the polar concept has been extended to include all electron-donating and electron-accepting phenomena.

The polar and apolar components of the free energies of interaction are additive (van Oss et al. 1997):

$$\Delta G = \Delta G^{LW} + \Delta G^{AB} \tag{A-14}$$

it follows that:

$$\gamma_i = \gamma_i^{LW} + \gamma_i^{AB} \tag{A-15}$$

Because the electron-donating and the electron-accepting sites at a surface or interface are different and play different roles in the interfacial interactions, the polar properties of a surface are inherently asymmetrical and must be described by two parameters (van Oss et al. 1997). This is very different from the LW interactions where, for example, (Eq. 11):

$$\Delta G_{ij}^{LW} = -2\sqrt{\gamma_i^{LW}\gamma_j^{LW}} \tag{A-16}$$

Such a simple combining rule is not applicable to AB interactions (Giese and van Oss 2002). For the AB interactions the free energy of interaction between two materials, *i* and *j* is:

$$\Delta G_{ij}^{AB} = -2\sqrt{\gamma_i^- \gamma_j^+} - 2\sqrt{\gamma_j^- \gamma_i^+} \tag{A-17}$$

where, the electron-donor parameter is designated as γ^- and the electron-acceptor parameter is designated as γ^+.

The polar component of the surface tension of compound, *i*, then is:

$$\gamma_i^{AB} = 2\sqrt{\gamma_i^+ \gamma_i^-} \tag{A-18}$$

The Dupre equation is also applicable to polar interactions (van Oss et al. 1997):

$$\Delta G_{ij}^{AB} = \gamma_{ij}^{AB} - \gamma_i^{AB} - \gamma_j^{AB} \tag{A-19}$$

so that the AB component of the interfacial tension can be written as:

$$\gamma_{ij}^{AB} = \Delta G_{ij}^{AB} + \gamma_i^{AB} + \gamma_j^{AB} \tag{A-20}$$

and, substituting the value for ΔG_{ij}^{AB} from Eq. (17) and the values for γ^{AB} from Eq. (18), gives:

$$\gamma_{ij}^{AB} = 2\left(\sqrt{\gamma_i^- \gamma_i^+} + \sqrt{\gamma_j^- \gamma_i^+} - \sqrt{\gamma_i^- \gamma_j^+} - \sqrt{\gamma_j^- \gamma_i^+}\right) \tag{A-21}$$

or

$$\gamma_{ij}^{AB} = 2\left(\sqrt{\gamma_i^+} - \sqrt{\gamma_j^+}\right)\left(\sqrt{\gamma_i^-} - \sqrt{\gamma_j^-}\right)$$

Examination of the expression for the AB component of the interfacial tension (Eq. 21) shows that γ_{ij}^{AB} is not restricted to positive values or zero, as is the case for γ_{ij}^{LW}. Rather, γ_{ij}^{AB} will be negative when either:

$$\gamma_i^+ > \gamma_j^+ \text{ and } \gamma_i^- < \gamma_j^-$$

or

$$\gamma_i^+ < \gamma_j^+ \text{ and } \gamma_i^- > \gamma_j^-$$

Since the AB and LW components of the interfacial tension are additive, the total expression for the interfacial tension between two materials is:

$$\gamma_{ij} = \left(\sqrt{\gamma_i^{LW}} - \sqrt{\gamma_j^{LW}}\right)^2 + 2\left(\sqrt{\gamma_i^-\gamma_i^+} + \sqrt{\gamma_j^-\gamma_j^+} - \sqrt{\gamma_i^-\gamma_j^+} - \sqrt{\gamma_j^-\gamma_i^+}\right) \qquad \text{(A-22)}$$

The values of the surface tension components and parameters of an unknown solid are determined by measuring contact angles of liquid drops on the solid and solving Young's equation. For this to work, the surface tension components and parameters of the test liquids must be known. This presupposes that one knows these values for a group of high-energy liquids (i.e., those which will form finite contact angles on solid surfaces of interest). The values for the liquids can be obtained in a number of ways. For example, the total surface tension, γ, of the liquid can be derived from the shape of a pendant drop (Adamson 1990). For apolar liquids (e.g., alkanes), this measurement gives the LW component, γ^{LW}, which completely characterizes the properties of the liquid. However, for polar liquids the situation is more complex. Here,

similarly, the total surface tension can be obtained directly: for water, as an example, γ_w = 72.8 mJ/m^2. The LW component can be obtained by contact angle measurements of the liquid on a low-energy, apolar solid such as Teflon (Giese and van Oss 2002). For water, γ_w^{LW} = 21.8 mJ/m^2 so that, by difference, the AB component is found to be γ_w^{AB} = 51 mJ/m^2. However, there is no way to determine the values of both polar parameters from γ^{AB} as seen from Eq. (18). It is convenient to set $\gamma_w^+ = \gamma_w^-$ = 25.5 mJ/m^2 at 20^{o}C. While this choice is arbitrary, it has no effect on the values of, e.g., γ_{12}^{AB}, ΔG_{12}^{AB}, ΔG_{131}^{AB} and ΔG_{132}^{AB}, which are the values of interest (van Oss 2002).

The Dupre equation for three materials (of which at least one, i.e., #3, must be a liquid) gives us:

$$\Delta G_{132} = \gamma_{12} - \gamma_{13} - \gamma_{23} \tag{A-23}$$

Expanding this in terms of the AB and LW components gives:

$$\begin{aligned}\Delta G_{132} = {} & \sqrt{\gamma_1^{LW}\gamma_3^{LW}} + \sqrt{\gamma_2^{LW}\gamma_3^{LW}} - \sqrt{\gamma_1^{LW}\gamma_2^{LW}} - \gamma_3^{LW} + \\ & 2\sqrt{\gamma_3^+}\left(\sqrt{\gamma_1^-} + \sqrt{\gamma_2^-} - \sqrt{\gamma_3^-}\right) + \\ & 2\sqrt{\gamma_3^-}\left(\sqrt{\gamma_1^+} + \sqrt{\gamma_2^+} - \sqrt{\gamma_3^+}\right) - \\ & 2\sqrt{\gamma_1^+\gamma_2^-} - 2\sqrt{\gamma_1^-\gamma_2^+}\end{aligned} \tag{A-24}$$

Similarly, the interaction energy between two identical materials, 1, immersed in liquid 3 gives:

$$\begin{aligned}\Delta G_{131} &= -2\gamma_{13} \\ &= -2\left(\sqrt{\gamma_1^{LW}} - \sqrt{\gamma_3^{LW}}\right)^2 - 4\left(\sqrt{\gamma_1^+\gamma_1^-} + \sqrt{\gamma_3^+\gamma_3^-} - \sqrt{\gamma_1^+\gamma_3^-} - \sqrt{\gamma_3^+\gamma_1^-}\right)\end{aligned} \tag{A-25}$$

and the interaction between two different materials, 1 and 2, in vacuum is:

$$\Delta G_{12} = -2\left(\sqrt{\gamma_1^{LW}\gamma_2^{LW}} + \sqrt{\gamma_1^+\gamma_2^-} + \sqrt{\gamma_2^+\gamma_1^-}\right) \quad \text{(A-26)}$$

It is clear from Eq. (26) that the sign of the interaction energy between any two materials in vacuum is always negative (according to the usual sign convention of chemical thermodynamics), i.e., there is an attraction between them, and cannot be zero because γ^{LW} for all materials is finite and positive.

The above discussion concerning the interaction energy (ΔG_{132} and ΔG_{121}) between particles immersed in a liquid still is incomplete if these particles carry an electrostatic charge, in which case an additional term must be added which expresses the electrostatic contribution, termed EL, to the total interaction energy, expressed in general terms (Giese and van Oss 2002):

$$\Delta G = \Delta G^{LW} + \Delta G^{AB} + \Delta G^{EL} \quad \text{(A-27)}$$

The inclusion of the EL contribution may be important when the particles are silicate minerals immersed in water. The existence of a charge at the surface of the solid, which is the potential of the particle, ψ_o, and it is this quantity that is the basis for the interaction energy calculation. The ψ_o potential can be calculated from the ζ-potential as:

$$\Psi_o = \zeta(1 + z/a)e^{\kappa z} \quad \text{(A-28)}$$

where, z is the distance from the surface to the slipping plane, a is the radius of the particle, and κ is the inverse thickness of the diffuse double layer. When, in addition to ΔG_{1w2}^{IF}, the electrostatic interaction energy must be taken into account, the value of ψ_o is then obtained from the values $\psi_{o(1)}$ and $\psi_{o(2)}$ by means of the geometric mean combining rule (Giese and van Oss 2002):

$$\psi_{o(12)} = \sqrt{\psi_{o(1)}\psi_{o(2)}} \tag{A-29}$$

Thus far the discussion has dealt with the interfacial interactions between condensed media at contact. The net interfacial interaction is formulated as the value of ΔG, and the sign indicates whether there is a net attraction (negative sign) or a net repulsion (positive sign), according to the usual convention of chemical thermodynamics. To date only contact angle analysis is capable of yielding the actual surface or interfacial properties at the precise surface of solids (van Oss et al. 1987). Contact angle (θ) measurement, first described by Thomas Young in 1805, remains at present the most accurate method for determining the interaction energy between a liquid (L) and a solid (S) at the minimum equilibrium distance between the liquid and the solid at the interface between the two:

$$\gamma_L \cos\theta = \gamma_S - \gamma_{SL} \tag{A-30}$$

where, γ_{SL} represents the interfacial tension between the liquid and the solid.

In Eq. (30), γ_L (usually) and cosθ are known and γ_S and γ_{SL} are the unknowns. Using two different liquids gives rise to two equations with three unknowns (i.e., γ_S, γ_{SL1}, and γ_{SL2}) where the subscripts 1 and 2 refer to the two equations (i.e., the two different liquids). Thus, Eq. (30), in the form given above, is not practically usable. However, in conjunction with the Dupre equation in the following form:

$$\Delta G_{SL} = \gamma_{SL} - \gamma_S - \gamma_L \tag{A-31}$$

Equation (30) then becomes:

$$(1 + \cos\theta)\gamma_L = -\Delta G_{SL} \tag{A-32}$$

which is known as the Young-Dupre equation. Equation (32) has only one unknown; ΔG_{SL}. Combining Eqs. (30) and (31) with Eq. (32), one obtains:

$$(1+\cos\theta)\gamma_L = 2\left(\sqrt{\gamma_S^{LW}\gamma_L^{LW}} + \sqrt{\gamma_S^+\gamma_L^-} + \sqrt{\gamma_S^-\gamma_L^+}\right) \qquad \text{(A-33)}$$

which is the complete Young-Dupre equation, applicable to apolar as well as to polar systems (van Oss 1994). Cosθ is a measure of the equilibrium between the energy of cohesion between the molecules of liquid *L* and the energy of adhesion between liquid *L* and solid *S*. Thus, the measured contact angle between *L* and *S* permits the use of the liquid-solid interaction as a force balance. It should be noted that Eq. (33) contains three unknowns, i.e., γ_S^{LW}, γ_S^+, and γ_S^- (assuming that the values for γ_L^{LW}, γ_L^+, and γ_L^- are known). To obtain the three γ-component values for the solid, *S*, it is therefore necessary to measure contact angles with three different liquids, of which at least two must be polar. It should be emphasized that to obtain finite, measurable contact angles γ_L must be greater than γ_S. When $\gamma_L < \gamma_S$, the liquid forms no contact angle on the solid but spreads and wets it completely.

For Lewis acid-base (or for that matter for covalent) interactions, the cohesive energy holding the solid together is not measurable by the contact angle approach. By contact angle measurements with polar liquids one determines the excess γ_S^+ or, in most cases, the excess γ_S^- value of a dry surface. When, as is generally the case, in the polar part of the cohesion of a solid, when all the electron-acceptors (γ^+) are bound to an equivalent number of electron-donors (γ^-), there tends to be a sizable number of unbound electron-donors (γ^-) left over (van Oss et al. 1997). This excess γ^- is the only polar entity that can be measured via the contact angle approach on dry solid surfaces. It is also the only γ^- by which the solid can interact with other polar entities, solid or liquid. Thus, for any solid, γ_S is best defined as the value of $\gamma_S^{LW} + 2\sqrt{\gamma_S^+\gamma_S^-}$ that is obtained by contact angle determination. As a dry solid generally only gives either a γ_S^+ or γ_S^-, its $\gamma_S = \gamma_S^{LW}$.

When both γ_S^+ and γ_S^- values are found for a solid surface, it is wet, usually with water. It is only in polar liquids that electron-acceptors (γ_L^+) and electron-donors (γ_L^-) can co-exist (van Oss et al. 1997).

The Young equation is held to be valid for contact angles measured as the advancing angle, i.e., the angle the drop makes when it has just ceased across the solid surface (e.g., for at most a few seconds [Chaudhury 1984]). Only the advancing contact angle has significance when used to obtain γ-values by means of the Young-Dupre equation, because only an advancing drop encounters a new uncontaminated surface (Giese and van Oss 2002). Even when one of the two parameters (γ^+ or γ^-) is zero (as is the rule with dry solid surfaces), that fact plays an important role in determining whether particles of a solid or solute, immersed in a polar liquid, will attract or repel each other. Dry polar solid surfaces are monopolar. This monopolarity is usually in favor of electron-donicity (van Oss et al. 1997).

When solids show a non-negligible γ^+-value (e.g., by contact angle measurements) in conjunction with a sizable γ^-, one must immediately suspect the presence of residual liquid on the surface of the solid, which usually is residual water of hydration (van Oss et al. 1997). The cohesive and adhesive parts of the total interaction energy may be described as:

$$\Delta G_{1w1}^{IF} = \overbrace{-2\gamma_1^{LW}}^{cohesion} \overbrace{-2\gamma_w^{LW}}^{cohesion} \overbrace{+4\sqrt{\gamma_1^{LW}\gamma_w^{LW}}}^{adhesion} \overbrace{-4\sqrt{\gamma_1^+\gamma_1^-}}^{cohesion} \underbrace{-4\sqrt{\gamma_w^+\gamma_w^-}}_{cohesion} \underbrace{+4\sqrt{\gamma_1^+\gamma_w^-}}_{adhesion} \underbrace{+4\sqrt{\gamma_w^+\gamma_1^-}}_{adhesion} \quad \text{(A-34)}$$

where, the subscript, w, stands for water and subscript, 1, denotes the particle immersed in water. ΔG_{1w1}^{IF} is the interfacial free energy of interaction between two molecules or particles, 1, in water. It can be seen that the cohesive terms are all negative (i.e., attractive) while the adhesive terms are all positive (i.e., repulsive) according to the

usual convention of chemical thermodynamics. Thus, attraction prevails when the total of the cohesive terms is larger than the total of the adhesive terms.

The following are the principal rules for obtaining optimal accuracy and reproducibility in determining the apolar and the polar surface tension components and parameters of solid materials by contact angle measurements (van Oss 2002). To obtain the three surface tension components and parameters, γ_S^{LW}, γ_S^+, and γ_S^-, for polar surfaces, s, one must use the Young-Dupre equation three times, with three different liquids, of which two must be polar, as well as significantly different in their polar properties. It is useful also to employ one high-energy apolar liquid, for which the best choice is diiodomethane (DIM) (or called methylene iodide). Although DIM possesses a tiny degree of electron-accepticity to the extent of $\gamma_{DIM} \approx 0.01$ mJ/m^2, this may be neglected in virtually all cases. The high surface tension of DIM ($\gamma_{DIM} = 50.8$ mJ/m^2 at 20^{o}C) allows it to be used for measuring γ_S^{LW} of practically all mineral surfaces. The main precaution to be taken with DIM is to keep it in complete darkness at all times and discard it when it turns pink. Because of the use of DIM as a probe for the apolar surface tension component (γ_S^{LW}) of solid materials, the advancing contact angle obtained with DIM usually does not significantly diminish with time (which often is in contrast with polar contact angle liquids) so that in calculating the values for γ_S^{LW}, γ_S^+, and γ_S^- there is an advantage to determine the value for γ_S^{LW} with DIM as the first step, and then to use the value for γ_S^{LW} thus obtained to insert into the two remaining equations for subsequent determination of γ_S^+ and γ_S^-.

After using DIM as the first liquid to measure contact angles on a given surface for the determination of γ_S^{LW}, the choice of the polar contact angle liquids becomes important. It should be realized that one can really only use two different categories of polar liquids. The first category comprises only water, while all the other usable polar liquids (e.g., glycerol, formamide, ethylene glycol) together represent the second category (van Oss 2002). This is because water has relatively high and rather similar

values for both γ_W^+ and γ_W^- (which for practical standardization purposes are both assumed to be equal to 25.5 mJ/m^2 at 20^{o}C). The γ_L^+/γ_L^- ratios (R) for the other three major polar contact angle liquids differ greatly from the (assumed) value of $R_W = 1.0$ for water (w), the R for all the others being more that 10 times smaller than R_W. It is therefore very important for any determination of γ_S^+ and γ_S^- to use combinations of two liquids that differ substantially in their γ_L^+/γ_L^- ratios, which in practice means that one must always only use contact angle liquid pairs such as water + glycerol, water + formamide, or water + ethylene glycol. Any departure from this rule leads to unreliable results (van Oss 2002).

Contact angle measurements on porous, irregular-shape materials are extremely difficult. This has led to an introduction of more sophisticated approaches that allow for a study of thermodynamic and kinetic information. Inverse Gas Chromatography (IGC) and the Universal Sorption Device (USD) are among the most commonly used methods. These methods are based on isotherm determination, by which the measurement of surface area and thus surface free energy components are possible. The IGC and USD are usually considered as dynamic sorption techniques, where the stationary phase is the sample under investigation while a substance in the mobile phase acts as a probe molecule. An empty column is filled with the porous material (adsorbent) under investigation and the probe molecule (adsorbate) in the mobile phase covers the surface of the adsorbent. In this process, the probe is a gas or a vapor interacting with the solid sample. After the injection of the probe molecule, adsorption takes place at the sample surface in the column, followed by desorption. These interactions cause retention on the surface of the material.

The IGC and USD systems consist of high temperature and high pressure and very sensitive electronic balance systems with a precision of at least 0.0001 mg, which is necessary for adsorption studies. In the IGC method the acid-base component is assumed as a single polar term, ignoring the two separate terms (γ^+ and γ^-) of the AB

interactions (Thielmann 2004). However, the USD method uses the latest acid-base approach developed by Chaudhury (1984).

In the USD method a set of three probe liquids are usually used for measuring spreading pressure π_e on the surface of solids. The probe liquids are apolar nHexane, monopolar methyl propyl ketone, and bipolar water. In Dupre equation (Eqs. 8 and 19), γ_1 and γ_2 refer, respectively, to phase 1 and 2 measurements in vacuum. The spreading pressure is defined as the difference in the free energy of adhesion between the measurements made in vacuum and when the measurements are made in the presence of vapor. Thus the spreading pressure represents reduction of the surface energy of the material in vacuum by adsorption of the vapor at the material surface:

$$\pi_e = \frac{RT}{A}\int_0^{P_0}\frac{n}{P}dP \tag{A-35}$$

where, P_o is the saturated vapor pressure of the adsorbate, n is the specific amount adsorbed on the surface of the adsorbent, A is the specific surface area of the adsorbent, R is the universal gas constant, and T is the temperature.

The Brunauer-Emmett-Teller (BET) model is applied to the isotherm data to obtain the specific surface area of the solid material:

$$\frac{P}{n(P_o - P)} = \frac{1}{n_m c} + \left(\frac{c-1}{n_m c}\right)\frac{P}{P_o} \tag{A-36}$$

where, n and n_m are the amount adsorbed and the monolayer capacity per unit mass of adsorbent and c is a parameter theoretically related to the net molar enthalpy of adsorption. The value of n_m is obtained from the plot of $P/n(P\text{-}P_o)$ versus P/P_o over the pressure (P/P_o) range from 0 to 0.4.

The specific surface area (A) of the solid is then calculated by:

$$A = \left(\frac{n_m N_o}{M} \right) \alpha \tag{A-37}$$

where, α is the projected area of a single molecule, which is computed by the hexagonal close-packing model:

$$\alpha = 1.091 \left(\frac{M}{N_o \rho} \right)^{2/3} \tag{A-38}$$

where ρ is the density of the adsorbed molecule in liquid at the adsorption conditions, M is its molecular weight, and N_o is Avagadro's number.

The work of adhesion of liquid on a solid usually can be expressed in terms of the surface tension of the liquid and the equilibrium spreading pressure of adsorbed vapor on the solid surface by (Fowkes 1963):

$$G_A = \pi_e + 2\gamma_l \tag{A-39}$$

This yields the following general result:

$$\pi_e + 2\gamma_l = 2\sqrt{\gamma_s^{LW} \gamma_l^{LW}} + 2\sqrt{\gamma_s^+ \gamma_l^-} + 2\sqrt{\gamma_s^- \gamma_l^+} \tag{A-40}$$

These equations lead to a method for measuring and calculating the specific surface free energy and its acid-base components.

The apolar component of the surface free energy of a solid can be determined by measuring the π_e of an apolar liquid on the surface of the solid and using following equation:

$$\gamma_s^{LW} = \frac{\left(\pi_e + 2\gamma_l\right)^2}{4\gamma_l^{LW}} \tag{A-41}$$

To solve for γ^+_s and γ^-_s we need to choose another two bipolar liquids or one monopolar liquid and one bipolar liquid or two monopolar liquids with opposite polarity, which have had known values of γ_l, γ^{LW}_l, γ^+_l, and γ^-_l, then measure the values of their π_e, respectively. For example, if we choose one monopolar basic liquid and one bipolar liquid, the values of γ^+_s and γ^-_s can be computed by:

$$\gamma_s^+ = \frac{\left(\pi_e + 2\gamma_{lm} - 2\sqrt{\gamma_s^{LW}\gamma_{lm}^{LW}}\right)^2}{4\gamma_{lm}^-} \tag{A-42}$$

$$\gamma_s^- = \frac{\left(\pi_e + 2\gamma_{lb} - 2\sqrt{\gamma_s^{LW}\gamma_{lb}^{LW}} - 2\sqrt{\gamma_s^+\gamma_{lb}^-}\right)^2}{4\gamma_{lb}^-} \tag{A-43}$$

where, γ_{lm}, γ_{lm}^{LW}, and γ_{lm}^- are surface tension, apolar component, and basic component of the monopolar basic liquid and γ_{lb}, γ_{lb}^{LW}, γ_{lb}^-, and γ_{lb}^+ are the surface tension, apolar component, basic component, and acidic component of the bipolar liquid. Finally, the value of γ_s can be obtained by the following relationship:

$$\gamma_s = \gamma_s^{LW} + 2\sqrt{\gamma_s^+\gamma_s^-} \tag{A-44}$$

In addition to the determination of surface free energies or work of adhesion or bond strength by the LW-AB type approaches, there are contact mechanics experiments which use the surface forces apparatus (e.g., atomic force microscopy [AFM] type devices). The results of these tests are usually analyzed by the Johnson-Kendall-Roberts (JKR) or the Derjaguin-Muller-Toporov (DMT) equations. However, there is still

debate among researchers whether the work of adhesion as calculated by contact angle measurements can be related to the results from the mechanical pull-off tests (Packham 1996). The surface force apparatus (SFA) was first developed by Tabor, Winterton, and Israelachvili for direct measurement of van der Waals forces between molecularly smooth sheets of mica. The apparatus uses crossed cylinders of molecularly smooth cleaved mica between which forces may be measured with a sensitivity of 10^{-8} N. This is achieved by sensitive detection of small movements in force-measuring springs capable of a distance resolution of 0.1 nm. The basic experiment by which surface forces apparatus is used to deduce surface energy values involves bringing the two surfaces into contact and observing either the load necessary to cause them to separate or the relationship between the radius of the contact zone and the applied load. AFM is capable of solid surface characterization at microscopic scales. It can also be used to determine surface tension of solids from pull-off force measurements (Drelich et al. 2004). Two techniques based on either contact angle for macroscopic surfaces or adhesion force measurements for microscopic surfaces by AFM have been under intensive development by researchers in recent years.

If two elastic bodies come into contact, the size of the area of contact will depend on the load and the elastic moduli of the bodies. A whole range of problems of this kind was treated by Hertz in the nineteenth century (Drelich et al. 2004). The Hertz approach is still widely applied to such problems in engineering. However, Hertz did not take surface forces into account. The adhesion forces between the two bodies in contact cause an increase in contact area. Johnson et al. (1971) allowed for surface forces and produced the following JKR equation for two elastic spheres of radii R_1 and R_2 in contact:

$$a^3 = \left\{F + 3\pi R G_{12} + \sqrt{[6\pi R G_{12} F + (3\pi R G_{12}]^2}\right\} R/K \qquad \text{(A-45)}$$

where, a is the radius of the area of contact, $R = R_1R_2/(R_1 + R_2)$, F is the normal load, and K is an elastic constant. Johnson et al. (1971) identified the critical adhesion or "pull-off" force as:

$$F_s = -1.5\pi RG_{12} \tag{A-46}$$

The other most commonly referred theory of adhesion which predicts a different pull-off force from that of Equation (46) is the DMT equation by Derjaguin et al. (1975):

$$F_s = -2\pi RG_{12} \tag{A-47}$$

The DMT theory accounts for the effect of surface forces just outside the area of contact. Israelachvili (1992) points out that the "true" pull-off force probably lies between the values predicted by Equations (46) and (47).

The equilibrium work of adhesion is defined by the Gibbs free energy change per unit area of interacting interface surfaces and is expressed by the Dupre equation, as given above. If one of the interacting surfaces is replaced with a spherical particle, such as the probe tip systems used in AFM, the relation between the work of adhesion and adhesion (pull-off) force can be described by the DMT and JKR models. However, Drelich et al. (2004) point out that many practical systems deviate from the idealized models as the DMT and JKR. In reality, particles and/or substrates deform elastically, viscoelastically, and/or plastically under applied load during adhesion, and particle-substrate analysis requires more accurate contact mechanics models that include a physical deformation component. Two contact mechanics models derived by Johnson et al. (1971) and Derjaguin et al. (1975) are frequently used by researchers to interpret the pull-off forces measured by the AFM technique. In general, both JKR and DMT models apply to particle-substrate systems where the following assumptions are met (Packham 1996): (i) deformations of materials are purely elastic, described by classical continuum elasticity theory, (ii) materials are isotropic, (iii) both Young's modulus and Poisson's ratio of materials remain constant during deformation, (iv) the contact diamater between

particle and substrate is small compared to the diameter of particle, and (v) no chemical bonds are formed during adhesion.

The difference between the JKR and DMT models occurs in assuming the nature of forces acting between particle and substrate. Johnson et al. (1971) assumed in their model that attractive forces act only inside the particle-substrate contact area, whereas Derjaguin et al. (1975) included long-range surface forces operating outside the particle-substrate contact area. Drelich et al. (2004) state that the DMT model is more appropriate for systems with hard materials having low surface energy and small radii of probe curvature. The JKR model applies better to softer materials with higher surface energy and larger probes. Drelich et al. (2004) also point out that this generalization does not bring researchers any closer to selecting the appropriate model and the selection is not always straightforward.

Maugis (1992) analyzed both the JKR and DMT models and suggested that the transition between these models can be predicted from the dimensionless parameter λ defined as:

$$\lambda = \frac{2.06}{z_o}\sqrt[3]{\frac{RG_A^2}{\pi K^2}} \tag{A-48}$$

where, z_o is the equilibrium separation distance between the probe and substrate, R is the radius of the probe, G_A is the work of adhesion, and K is the reduced elastic modulus for the particle-substrate system where:

$$\frac{1}{K} = \frac{3}{4}\left(\frac{1-\nu_p^2}{E_p} + \frac{1-\nu_s^2}{E_s}\right) \tag{A-49}$$

where, ν is the Poisson ratio, E is Young's modulus, and p and s stand for probe (particle) and substrate, respectively. For $\lambda \geq 5$ the JKR model applies, whereas the DMT model is more appropriate for systems with $\lambda \leq 0.1$.

REFERENCES

Adamson, A.W. (1990). *Physical Chemistry of Surfaces*. Wiley-Interscience, New York.

Brant, J.A. and Childress, A.E. (2004). Colloid adhesion to hydrophilic membrane surfaces. *Journal of Membrane Science*, 241, 235-248.

Chaudhury, M.K. (1984). Short range and long range forces in collod and macroscopic systems. Ph.D. Thesis, SUNY at Buffalo.

Derjaguin, B.V., Muller, V.M., and Toporov, Y.P. (1975),. Effect of Contact Deformations on the Adhesion of Particles, *Journal of Colloid and Interface Science*, 53, (2), 314-326.

Drelich, J., Tormoen, G.W., and Beach, E.R. (2004). Determination of solid surface tension from particle-substrate pull-off forces measured with the atomic force microscope. *Journal of Colloid and Interface Science*, 290, 484-497.

Fowkes, F.M. (1963). Additivity of intermolecular forces at interfaces. I. Determination of the contribution to surface and interfacial tensions of dispersion forces in various liquids. *Journal of Physical Chemistry*, 67, 2538-2541.

Giese, R.F., and van Oss, C.J. (2002). *Colloid and Surface Properties of Clays and Related Minerals*. Surfactant Science Series, 105, Mercer Dekker, Inc.

Giese, R.F., Wu, W., and van Oss, C.J. (1996). Surface and electrokinetic properties of clays and other mineral particles, untreated with organic or inorganic cations. *Journal of Dispersion Science and Technology*, 17, 527-547.

Israelachvili, J.N. (1992). *Intermolecular and Surface Forces*. 2nd Edition, Academic Press, New York.

Johnson, K.L., Kendall, K., and Roberts, A.D. (1971). *Proceedings Royal Society*, 95.

Maugis, D. (1992). Adhesion of Spheres: The JKR-DMT Transition Using a Dugdale Model, *Journal of Colloid and Interface Science*, 150, 243-269.

Medout-Marere, V., Malandrini, H., Zoungrana, T., Douillard, J.M., and Partyka, S. (1998). Thermodynamic investigation of surface minerals. *Journal of Petroleum Science and Engineering*, 20, 223-231.

Packham, D.E. (1996). Work of adhesion: contact angles and contact mechanics. *International Journal of Adhesion and Adhesives*, 16 (2), 121-128.

Rytov, S.M. (1959). Theory of electric fluctuations and thermal radiation, *Electronics Research Directorate*, AFCRL, Bedford, MA.

Thielmann, F. (2004). Introduction into the characterization of porous materials by inverse gas chromatography. *Journal of Chromatography A*, 1037, 115-123.

van Oss, C.J. (1994). *Interfacial Forces in Aqueous Media*. Mercer Dekker, New York.

van Oss, C.J. (2002). Use of the combined Lifshitz-van der Waals and Lewis acid-base approaches in determining the apolar and polar contributions to surface and interfacial tensions and free energies. *Journal of Adhesion Science and Technology*, 16 (6), 669-677.

van Oss, C.J., Chaudhury, M.K., and Good, R.J. (1987). Monopolar surfaces. *Journal of Protein Chemistry*, 5, 385-405.

van Oss, C.J., Chaudhury, M.K., and Good, R.J. (1988). Interfacial Lifshitz-van der Waals and polar interactions in macroscopic systems. *Chemistry Review*, 88, 927-941.

van Oss, C.J., Giese, R.F., and Wu, W. (1997). On the predominant electron donicity of polar solid surfaces. *Journal of Adhesion Science and Technology*, 63, 71-88.

Zhao, Q., Liu, Y., and Abel, E.W. (2005). Surface free energies of electroless Ni-P based composite coatings. *Applied Surface Science*. 240, (1-4), 441-451.

APPENDIX B

MIXTURE GRADATIONS

Table B-1. Mixture 1 Gradation.

Sieve Size (mm)	5/8 Chips	MM D-Rock	MM D-Sand	Dolomitic Limestone Mineral Filler	Texas TY A Lime
	49%	31%	8%	11%	1%
	% Passing	**% Passing**	**% Passing**	**% Passing**	**% Passing**
50.8	100.00	100.00	100.00	100.00	100.00
37.5	100.00	100.00	100.00	100.00	100.00
25.4	100.00	100.00	100.00	100.00	100.00
19.5	100.00	100.00	100.00	100.00	100.00
12.7	88.60	100.00	100.00	100.00	100.00
9.5	55.30	86.50	100.00	100.00	100.00
4.75	2.00	29.70	100.00	100.00	100.00
2.36	1.00	4.00	85.80	100.00	100.00
1.18	0.80	3.10	60.30	100.00	100.00
0.6	0.70	2.30	41.30	100.00	100.00
0.3	0.60	2.10	28.20	99.60	100.00
0.075	0.40	1.20	12.70	66.10	100.00
Binder Source	Koch PG 76-22				
Optimum % Binder	6.3				

Table B-2. Mixture 2 Gradation.

Sieve Size (mm)	5/8 Chips	MM D-Rock	MM D-Sand	Dolomitic Limestone Mineral Filler	Texas TY A Lime
	49%	31%	8%	11%	1%
	% Passing	**% Passing**	**% Passing**	**% Passing**	**% Passing**
50.8	100.00	100.00	100.00	100.00	100.00
37.5	100.00	100.00	100.00	100.00	100.00
25.4	100.00	100.00	100.00	100.00	100.00
19.5	100.00	100.00	100.00	100.00	100.00
12.7	88.60	100.00	100.00	100.00	100.00
9.5	55.30	86.50	100.00	100.00	100.00
4.75	2.00	29.70	100.00	100.00	100.00
2.36	1.00	4.00	85.80	100.00	100.00
1.18	0.80	3.10	60.30	100.00	100.00
0.6	0.70	2.30	41.30	100.00	100.00
0.3	0.60	2.10	28.20	99.60	100.00
0.075	0.40	1.20	12.70	66.10	100.00
Binder Source	Valero PG 76-22				
Optimum % Binder	6.3				

Table B-3. Mixture 3 Gradation.

Sieve Size (mm)	MM C-Rock	MM D-Rock	MM Screenings	ARK Granite Donnafill	Texas TY A Lime
	18%	46%	25%	10%	1%
	% Passing	**% Passing**	**% Passing**	**% Passing**	**% Passing**
50.8	100.00	100.00	100.00	100.00	100.00
37.5	100.00	100.00	100.00	100.00	100.00
25.4	100.00	100.00	100.00	100.00	100.00
19.5	100.00	100.00	100.00	100.00	100.00
12.7	65.00	100.00	100.00	100.00	100.00
9.5	24.00	90.00	100.00	100.00	100.00
4.75	3.00	20.00	99.00	100.00	100.00
2.36	1.00	3.00	75.00	100.00	100.00
1.18	0.50	2.00	36.00	100.00	100.00
0.6	0.40	1.50	25.00	96.00	100.00
0.3	0.30	1.00	14.00	67.00	100.00
0.15	0.20	0.80	11.00	40.00	100.00
0.075	0.10	0.50	8.00	24.00	100.00
Binder Source	Wright PG 76-22				
Optimum % Binder	5.1				

Table B-4. Mixture 4 Gradation.

Sieve Size (mm)	MER C-Rock	MER D-Rock	MER Screenings	ARK Granite Donnafill	Texas TY A Lime
	22%	57%	12%	8%	1%
	% Passing	**% Passing**	**% Passing**	**% Passing**	**% Passing**
50.8	100.00	100.00	100.00	100.00	100.00
37.5	100.00	100.00	100.00	100.00	100.00
25.4	100.00	100.00	100.00	100.00	100.00
19.5	100.00	100.00	100.00	100.00	100.00
12.7	64.00	100.00	100.00	100.00	100.00
9.5	17.00	96.00	100.00	100.00	100.00
4.75	1.00	49.00	99.00	100.00	100.00
2.36	0.80	20.00	72.00	100.00	100.00
1.18	0.50	12.00	54.00	100.00	100.00
0.6	0.40	10.00	37.00	96.00	100.00
0.3	0.30	8.00	32.00	67.00	100.00
0.15	0.20	6.00	22.00	40.00	100.00
0.075	0.10	4.00	11.00	24.00	100.00
Binder Source	Wright PG 76-22				
Optimum % Binder	5.1				

Table B-5. Mixture 5 Gradation.

Sieve Size (mm)	Hanson C-Rock	Hanson D-Rock	TXI Screenings	Texas TY A Lime
	12%	55%	32%	1%
	% Passing	**% Passing**	**% Passing**	**% Passing**
50.8	100.00	100.00	100.00	100.00
37.5	100.00	100.00	100.00	100.00
25.4	100.00	100.00	100.00	100.00
19.5	100.00	100.00	100.00	100.00
12.7	64.00	100.00	100.00	100.00
9.5	17.00	96.00	100.00	100.00
4.75	1.00	49.00	99.00	100.00
2.36	0.80	20.00	72.00	100.00
1.18	0.50	12.00	54.00	100.00
0.6	0.40	10.00	37.00	100.00
0.3	0.30	8.00	32.00	100.00
0.15	0.20	6.00	22.00	100.00
0.075	0.10	4.00	11.00	100.00
Binder Source	Wright PG 76-22			
Optimum % Binder	5.0			

Table B-6. Mixture 6 Gradation.

Sieve Size (mm)	MER C-Rock	MER D-Rock	MER Pile #2	MER Screenings	Local Field Sand	Texas TY A Lime
	19%	16%	24%	28%	12%	1%
	% Passing	% Passing	% Passing	% Passing	% Passing	% Passing
37.5	100.00	100.00	100.00	100.00	100.00	100.00
25.4	100.00	100.00	100.00	100.00	100.00	100.00
22.4	100.00	100.00	100.00	100.00	100.00	100.00
9.5	20.70	92.80	99.60	100.00	100.00	100.00
4.75	1.00	30.20	62.30	100.00	99.70	100.00
2.00	0.60	5.10	7.70	76.00	99.00	100.00
0.425	0.60	2.90	4.20	32.20	97.70	100.00
0.18	0.60	2.50	3.40	16.00	35.90	100.00
0.075	0.50	1.60	2.20	4.10	11.90	90.00
Binder Source	Lion PG 76-22					
Optimum % Binder	5.1					

Table B-7. Mixture 7 Gradation.

Sieve Size (mm)	#8 Limestone	# 8 Gravel	Limestone Sand	Natural Sand
	27.50%	27.50%	12.50%	32.50%
	% Passing	% Passing	% Passing	% Passing
50.8	100.00	100.00	100.00	100.00
37.5	100.00	100.00	100.00	100.00
25.4	100.00	100.00	100.00	100.00
19.5	100.00	100.00	100.00	100.00
12.7	100.00	100.00	100.00	100.00
9.5	88.00	95.00	100.00	100.00
4.75	18.00	20.00	100.00	100.00
2.36	2.00	2.00	90.00	92.00
1.18	2.00	2.00	63.00	67.00
0.6	2.00	2.00	40.00	44.00
0.3	2.00	2.00	20.00	18.00
0.15	2.00	2.00	9.00	5.00
0.075	2.00	2.00	6.40	4.30
Binder Source	Tri-State PG 64-22			
Optimum % Binder	5.4			

Table B-8. Mixture 8 Gradation.

Sieve Size (mm)	#8 Gravel	Natural Sand	Limestone Sand
	65%	18%	17.50%
	% Passing	% Passing	% Passing
50.8	100.00	100.00	100.00
37.5	100.00	100.00	100.00
25.4	100.00	100.00	100.00
19.5	100.00	100.00	100.00
12.7	100.00	100.00	100.00
9.5	95.00	100.00	100.00
4.75	20.00	100.00	100.00
2.36	2.00	92.00	90.00
1.18	2.00	67.00	63.00
0.6	2.00	44.00	40.00
0.3	2.00	18.00	20.00
0.15	2.00	5.00	9.00
0.075	2.00	4.30	6.40
Binder Source	Marathon/Ashland PG 64-28		
Optimum % Binder	5.0		

APPENDIX C
THEORETICAL BASIS AND TEST PROCEDURES FOR THE UNIVERSAL SORPTION DEVICE

Universal Sorption Device

Theoretical Background

Surface energy of aggregates is calculated using spreading pressures of three probe vapors on the aggregate surface. The spreading pressure is calculated from an isotherm which is a plot of the mass of vapor adsorbed on the aggregate surface versus the partial vapor pressure of the probe. The USD that was used in this research project has indigenously developed software that carries out all necessary calculations to provide specific surface area of the aggregate and spreading pressure of any given vapor on the aggregate surface. Data generated by the USD for various vapors is compiled in a template Excel spreadsheet that calculates the surface energy components of the aggregate. The following theoretical background is for information only and, as mentioned earlier, most of the calculations are built into the test software.

Work of adhesion based on total surface of the probe vapor and its spreading pressure on the aggregate is given by:

$$W_a = \pi_e + 2\Gamma_l^T \qquad \text{(C-1)}$$

where,

W_a is the work of adhesion,

π_e is spreading pressure at saturation vapor pressure of the solvent, and

Γ^T_l is the total surface energy of the probe vapor.

The work of adhesion is also related to the surface energy of the solid and probe vapor as follows:

$$W_a = 2\sqrt{\Gamma_s^{LW}\Gamma_l^{LW}} + 2\sqrt{\Gamma_s^{+}\Gamma_l^{-}} + 2\sqrt{\Gamma_s^{-}\Gamma_l^{+}} \quad \text{(C-2)}$$

where,

W_a is the work of adhesion,

Γ is the surface energy,

subscript s refers to aggregate,

subscript l refers to probe vapor,

superscript LW refers to the Lifshitz-van der Waals or dispersive component,

superscript + refers to the acid component, and

superscript – refers to the base component.

From the above two relations the following equality can be established,

$$\pi_e + 2\Gamma_l^T = 2\sqrt{\Gamma_s^{LW}\Gamma_l^{LW}} + 2\sqrt{\Gamma_s^{+}\Gamma_l^{-}} + 2\sqrt{\Gamma_s^{-}\Gamma_l^{+}} \quad \text{(C-3)}$$

where the various terms are as described earlier.

The adsorbed mass of a vapor on the aggregate surface is related to the spreading pressure using Gibbs equation as follows:

$$\pi_e = \frac{RT}{A}\int_0^{p_0}\frac{n}{P}dP \quad \text{(C-4)}$$

where,

π_e is spreading pressure at saturation vapor pressure of the solvent,

R is universal gas constant,

T is absolute temperature, and

A is specific surface area of absorbent,

P is the vapor pressure of the probe vapor, and

n is the mass of the adsorbed vapor on the aggregate surface.

Spreading pressures of three probe vapors (nHexane, methyl propyl ketone, and water) with known surface energy values will generate a set of three linear equations based on Equation (C-3) which can be solved to obtain the three surface energy components of the aggregates.

Description of Test Equipment:

A process and instrumentation diagram of the latest test setup is shown in Figure C-1. This setup was developed as a part of the ongoing NCHRP project 9-37, "Using Surface Energy Measurements to Select Materials for Asphalt Pavements."

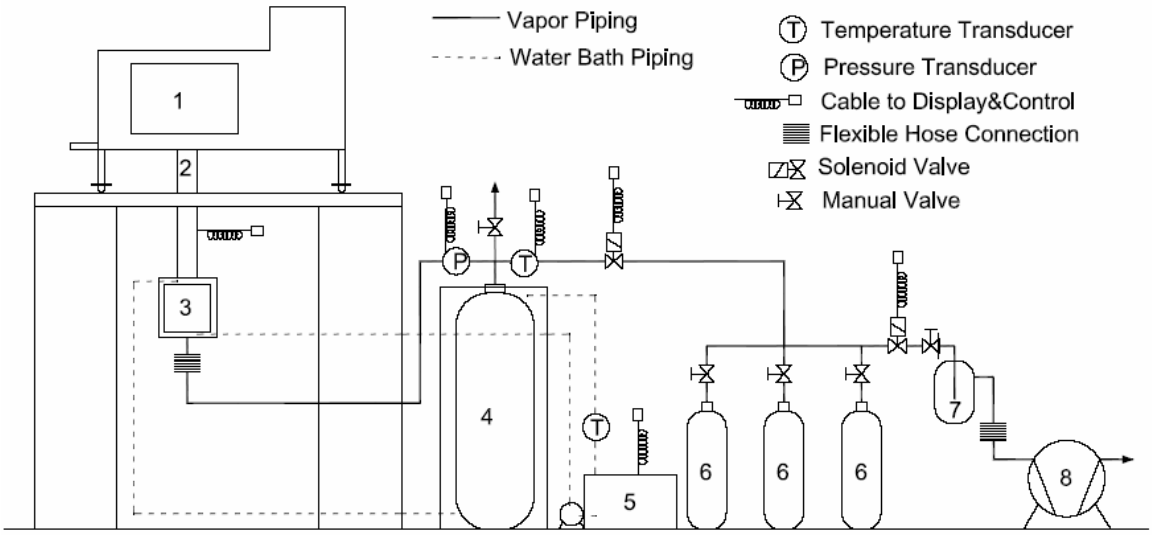

Figure C-1. Layout of Universal Sorption Device System.

1. Microbalance
2. Magnetic suspension
3. Sample cell
4. Buffer tank
5. Water bath
6. Probe vapor containers
7. Knock out tank
8. Vacuum pump

The mass of probe vapor that is adsorbed on to the aggregate surface is measured using a magnetic suspension balance. The aggregate sample itself is in an air-tight cell

beneath the balance. The advantage of a magnetic suspension balance is that it uses magnetic force to measure the sample mass and is therefore physically separate from the microbalance. The test is conducted at a temperature of 25°C. A water bath circulates water through a jacket of tubing that encloses the main sample cell and the buffer tank. The amount of vapor to be allowed during the test procedure is controlled using solenoid valve with feedback control.

Sample Preparation:

About 25 grams of sample is required for each test. The sample is put through a cleaning process and heated in a conventional oven at 120°C for about 4 to 6 hours. The sample is then allowed to cool in a dessicator with anhydrous calcium sulfate crystals that prevent adsorption of moisture on the aggregate surface.

Test Procedure:

See Universal Sorption Device Operating Procedures Manual.

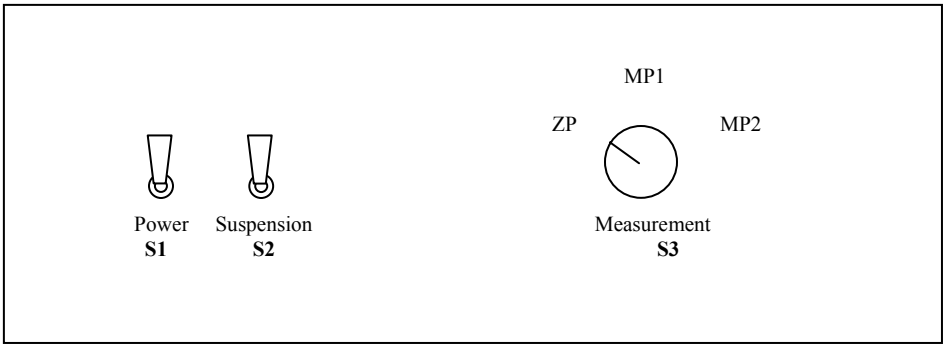

VALVE LOCATIONS

Figure C-2. Suspension Control.

VFV = Vapor flow valve
Three valves (one for each vapor) located at the bottom of the main control tower

VV = Venting Valve
Located near the buffer tank

VSV = Vacuum safety valve
Located next to vacuum pump to provide additional isolation of the pump and system

Cleaning Process
1) Water
2) Methanol
3) Hexane
4) Methanol

Drying Process
1) Place in oven for minimum 4 hours
2) Place in desiccator for cooling

Order of Solvents for Testing:
1) nHexane
2) MPK
3) Water

A: LOADING A NEW SAMPLE

FIRST ensure that all vapor flow valves (VFV) are CLOSED.

If the pressure in the system is below atmospheric, OPEN venting valve (VV) to allow air to get into the system.

Ensure that the vacuum pump is OFF by pulling plug and turn off water bath.

Place the jacket holder below the cell and remove the temperature jacket by removing the bolts below the cell.

Remove the six bolts holding the cell in a clockwise or anticlockwise fashion, gently loosening one bolt after another. Once all bolts are reasonably loose, hold the cell gently with one hand and remove the remaining bolts with the other hand.

Lower the cell gently on the jacket.

Start degassing software and execute Step C.

Put on gloves.

Remove the sample holder and rinse it with acetone and air dry it.

Pull aggregates out of desiccator, place the aggregates in the sample holder, and hang the sample holder back on the hook in the cell.

Execute Step B

Use a new O-ring, place it in on the cell, and raise the cell slowly back into its place.

Use the six bolts and gently tightening the bolts moving in one direction (raise the jacket to see if you got the alignment right).

DO NOT overtighten the bolts.

Raise the jacket and lock it using the bolt below the cell.

Remove the jacket holder.

Re-execute Step B.

Execute Step D.

B: **AFTER LOADING THE SAMPLE**

STEP 1.1
Open Set Balance Manual Software.

Switch on the power for the suspension system (S1).

Switch on the suspension (S2).

Wait for about 1 ½ minutes or until the balance reading looks stable, whichever comes first.

The balance should read about 11grams; if not, please consult troubleshooting manual.

Change S3 to MP1 and wait for about 1 ½ minutes or until the balance reading looks stable, whichever comes first.

The balance should read about 30 to 40 grams (11+ mass of aggregates you have added, which is about 25 grams). If this is the case go to step 1.2; if not go to step 1.3.

STEP 1.2
Change S3 from MP1 to ZP and wait for about 30 seconds.

The balance will return to a reading of about 11 grams.

Switch off suspension (S2).

You have successfully loaded the sample; everything else will be computer controlled from here on.

Let the power switch (S1) remain on for computer control.

Close Set Balance Manual Software.

Go back to Step A.

STEP 1.3
At MP1 if the mass is not 30 grams and the balance still shows a value of about 11 grams, the balance is very much off center. In such a case do the following steps:

Change S3 to ZP and wait for about 30 seconds. The suspension control will shut it self off.

Switch off suspension (S2) even though the light might be off on its own and wait for a few seconds.

Switch off the main power (S1) and wait for a few seconds.

Go to STEP 1.1: Switch on the main power (S1) .. etc.. (Note repeat process till you reach STEP 1.2).

C: DEGASSING

Start the vacuum pump.

Open the degassing software to start degassing process. The appropriate valves will open to enable degassing.

Ensure that the venting valve (VV) is CLOSED.

Ensure that the vacuum safety valve (VSV) is OPEN.

Ensure that the water bath is on and running with both the pump and compressor switched ON.

Degassing takes roughly 4 hours to complete.

Go back to Step A.

It is recommended that the balance be roughly centered at this time and the balance can be set for final centering after degassing is complete using a timer (see D).

Once degassing is complete the temperature will be close to 30°C and pressure typically -0.0050 psi. (Currently there is a linear offset of +0.0050 in pressure and -4.5°C in temperature). If this is not the case consult troubleshooting.

D: CENTERING THE BALANCE

The magnetic suspension balance weighs the sample when it is in magnetic suspension (hence the name!). To ensure that the suspension assembly is aligned and centered carry out the following steps:

Ensure that all lights on suspension control are OFF except the LED for S1.

Start the Auto Centering Balance software.

It is recommended that the fist one or two cycles be carried out using the "Read Unstable" mode. Once the balance starts showing steady readings the mode can be changed to "Stable only."

Set time to 4.00 hours.

Press start.

Start water pump.

Centering is achieved when consistent mass readings are observed.

At the end of 4 hours, check for degassing to be completed.

Clean aggregates and place in oven.

E: STARTING A NEW TEST AFTER DEGASSING

Ensure that balance was centered before starting the test (D).

All lights on the suspension control except for the power light must be OFF at this time. If this is not the case consult troubleshooting suspension balance section.

Start “USD Test” software.

Enter the required parameters in the software for the test.

Click on Run Test Button on the top right corner.

Open VFV for selected solvent.

Close VSV.

Turn off vacuum pump by pulling plug.

F: AFTER THE TEST IS COMPLETE

All lights on the suspension control except for the power light must be OFF at this time. If this is not the case consult troubleshooting suspension balance section.

Ensure that all vapor flow valves (VFV) are CLOSED (MPK, nHexane, Water, as the case may be).

OPEN venting valve (VV).

Go to A.

BOOTING THE COMPUTER AND GENERAL PRECAUTIONS

While rebooting the computer the following precautions must be taken:

Suspension and all electronics must be OFF.

Only when the computer is fully booted and ready switch on all the devices.

Other Precautions:

While manually controlling the suspension system DO NOT switch off the power when in MP1 or MP2. When the suspension is in MP1 or MP2 the permanent magnet at top of the suspension is very close to the electromagnet at bottom of the balance. Switching OFF the unit without lowering using ZP will cause this permanent magnet to shoot up and get stuck in the top. Refer to troubleshooting in such an eventuality.

APPENDIX D
THEORETICAL BASIS AND TEST PROCEDURES FOR THE WILHELMY PLATE METHOD

Wilhelmy Plate Method

Theoretical Background:

Surface energy components of asphalt are calculated using the contact angles of different probe liquids on the asphalt surface. The Wilhelmy Plate (WP) method is used measures the contact angle of a liquid on an aggregate surface. The WP method is based on kinetic force equilibrium when a very thin plate, suspended from a highly accurate balance, is immersed or withdrawn from a liquid solvent at very slow and constant speed. The contact angles that develop between the asphalt-coated glass plate and solvent liquids are measured. The dynamic contact angle between the asphalt coated plate and the probe liquid measured during the immersion process is called the advancing contact angle.

The basic principles of this method that are used to obtain the contact angles and the surface energy components of semi-liquid asphalt are summarized in the following paragraphs. When a plate is suspended in air, Equation (D-1) is valid:

$$F = Wt_{plate} + Wt_{asphalt} - V.\rho_{air}.g \qquad \text{(D-1)}$$

where,

F is the force measured with the Cahn Balance of the DCA (Figure D-1), which is also the force required to hold the plate,

Wt_{plate} and $Wt_{asphalt}$ are the weight of the glass plate and weight of the coated asphalt film, respectively,

V is the volume of the asphalt plate,

ρ_{air} is the density of the air, and

g is the local acceleration of gravity.

When a plate is partially immersed in a fluid, the balance measures the force using Equation (D-2):

$$F = Wt_{plate} + Wt_{asphalt} + P_t\Gamma_L \cos\theta - V_{im}\rho_L g - (V - V_{im})\rho_{air} g \quad \text{(D-2)}$$

where,

P_t is the perimeter of the asphalt coated plate,

Γ_L is the total surface energy of the liquid,

θ is the dynamic contact angle between the asphalt and the liquid, and

V_{im} is the volume of the immersed plate.

By subtracting Equation (D-1) from Equation (D-2), Equation (D-3) is obtained:

$$\Delta F = P_t\Gamma_L \cos\theta - V_{im}\rho_L g + V_{im}\rho_{air} g \quad \text{(D-3)}$$

Equation (D-4) is obtained by rearranging terms in Equation (D-3), and the contact angle can be calculated from all the parameters on the right hand side, which are determined during the test.

$$\cos\theta = \frac{\Delta F + V_{im}(\rho_L - \rho_{air})g}{P_t\Gamma_L} \quad \text{(D-4)}$$

The Good-van Oss-Chaudhury (20) Equation (D-5), is used to relate contact angle to surface energy components.

$$\Gamma_l(1 + \cos\theta) = 2\sqrt{\Gamma_s^{LW}\Gamma_l^{LW}} + 2\sqrt{\Gamma_s^-\Gamma_l^+} + 2\sqrt{\Gamma_s^-\Gamma_l^-} \quad \text{(D-5)}$$

where, Γ_l, Γ_l^+, and Γ_l^- are the surface free energy components of the liquid.

Description of Test Equipment:

Dynamic Contact Angle (DCA) equipment from Cahn was used for this test. Figure D-1 shows a schematic of the test.

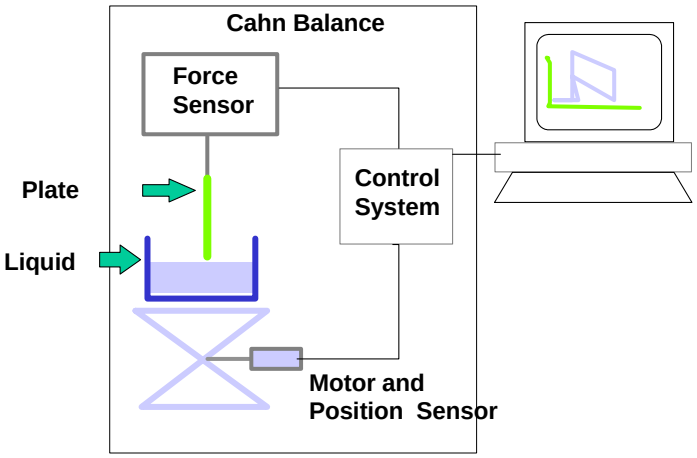

Figure D-1. The Cahn Dynamic Contact Angle Analyzer.

On the left side is the Wilhelmy Plate sample chamber in which the asphalt-coated glass plate is suspended from the Cahn Balance, and on the right is the data acquisition and processing system using the DCA software. The DCA software directly acquires data from the Cahn balance and automatically calculates the advancing and receding contact angles.

A typical output of the DCA is shown in Figure D-2. The advancing stage is represented by the bottom part of the hysteresis loop. When the plate advances to the liquid surface and touches it, a meniscus forms and the force increases substantially. As the plate is immersed, the advancing angle builds up with a corresponding decrease in slope due to buoyancy. As the direction of travel is reversed, the receding angle is measured and again, a slope due to buoyancy is observed. As mentioned earlier, this force due to buoyancy is accounted for in the equations for determining the contact angle.

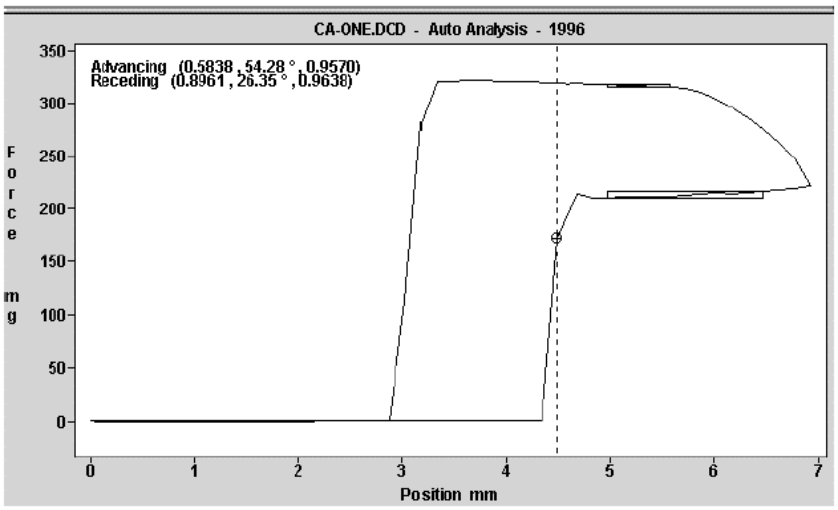

Figure D-2. Cahn Dynamic Contact Angle Analyzer Output.

Sample Preparation:

Glass slides (50 mm by 24 mm by 0.15 mm thick) provide a substrate for preparing the asphalt slides. The glass slides are rinsed with distilled water and acetone prior to use. The asphalt is heated in a small container at 90° to 135°C depending on the viscosity of the asphalt for about 2 hours in a conventional oven. Once the asphalt is ready for preparing slides it is placed over a hot plate set at sufficiently high temperature to prevent cooling of the asphalt. The glass slides are then dipped for about half their length in asphalt. Excess asphalt is allowed to drain from the slide. The slide may be held upside down for a few seconds to allow the formation of a smooth thin film over it. At least three slides per probe liquid are prepared. A minimum of three probe liquids (water, methyleneiodide, and ethylene glycol) are required, but more than three probes are generally recommended for this test procedure. Once the slides are prepared they are stored in a vacuum dessicator for about 24 hours prior to testing to remove any adsorbed moisture. The dimensions of the test slide are measured and recorded.

Test Procedure:

A fresh sample of the probe liquid (99 percent+ purity) is taken in a 50mL glass beaker and placed on the balance base. The asphalt slide is suspended from the top hook

of the balance. The WinDCA software is used to control the test and acquire and analyze the data and provide the contact angles. Once the contact angles are obtained, the surface energy components can be calculated using the equations described earlier. Researchers at Texas Transportation Institute have developed software, CASE, as a part of the ongoing NCHRP 9-37 project. This software is useful for selecting appropriate probe liquids for the WP test and also calculating the surface energy components from contact angle data.

APPENDIX E
OPERATIONAL PROCEDURES FOR DMA TESTING AND BOHLIN INSTRUMENTS SOFTWARE

1) Open software to "Login Screen." There is not a password required, so click "OK."

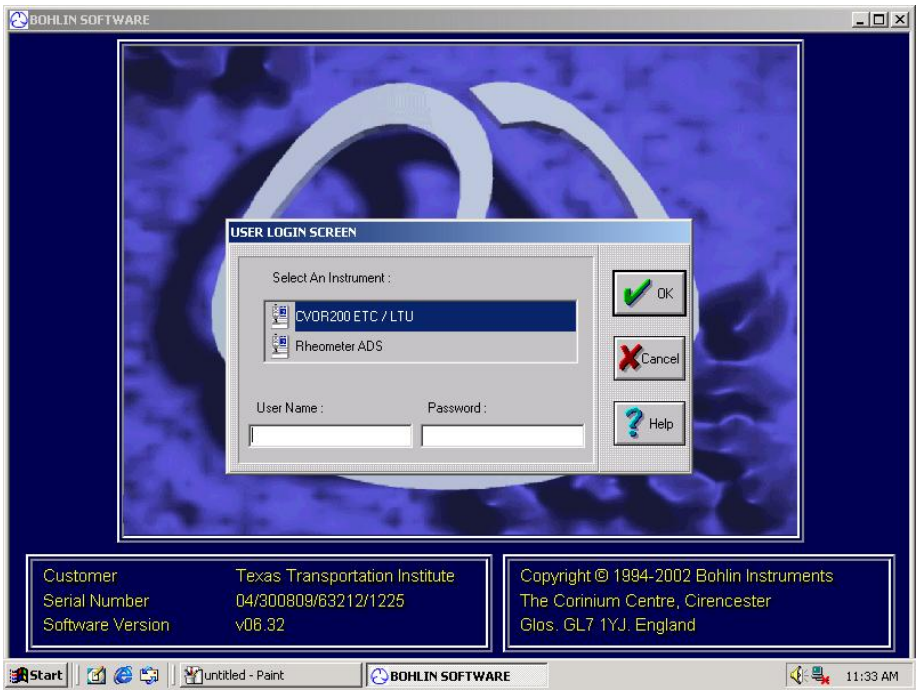

2) The main standard test screen will come up. Click on “Oscillation.”

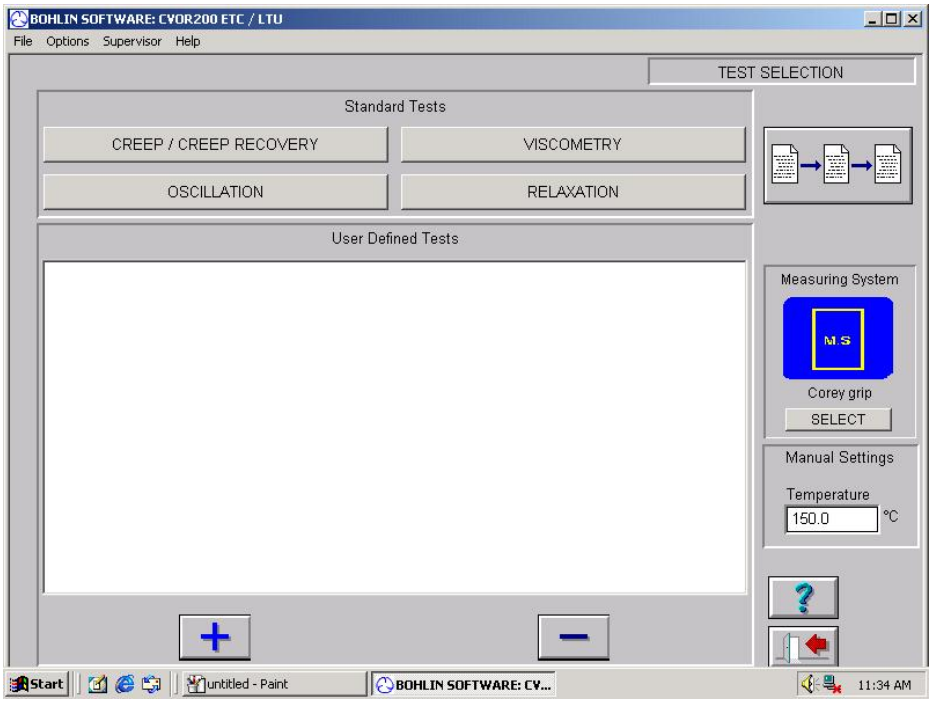

3) The Main Oscillation screen will appear.

   a. To set the Oscillation Test Parameters, click on the center button with oscillation squiggly line.

   b. To set the Measuring system, click on select button below "Measuring System."

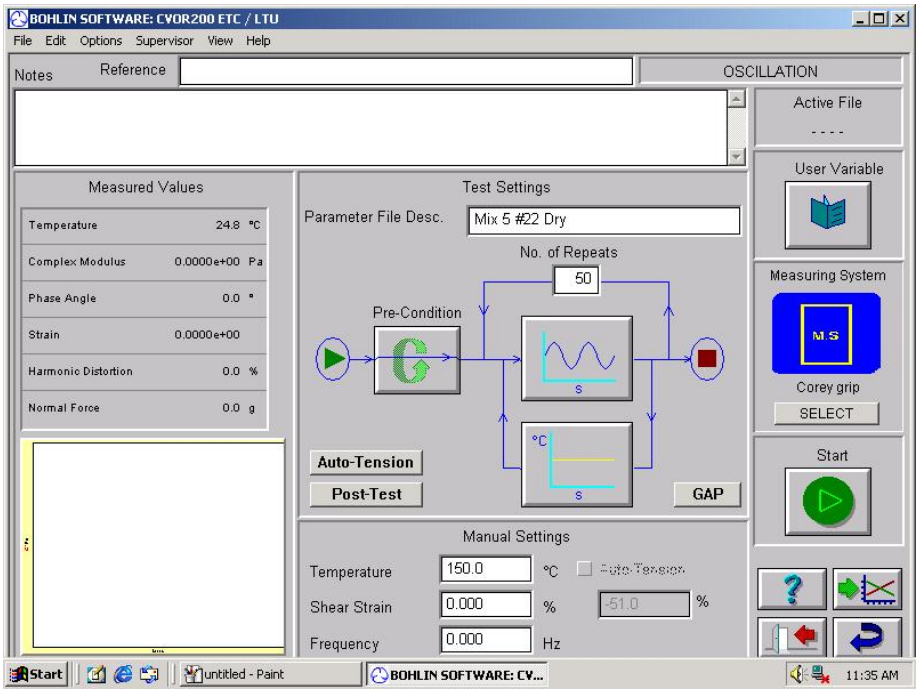

4) Set the Oscillation Test Parameters:

   a. Type in the desired frequency.

   b. Type in the desired strain level.

      i. This parameter will change depending whether testing for linear viscoelastic parameters (Low Strain) or fatigue damage parameters (High Strain).

   c. Set the # of cycles desired to run the Fourier Transform over to obtain a data point in the periods box.

   d. Set the desired # of points per # of cycles for the Fourier Transform in the points box.

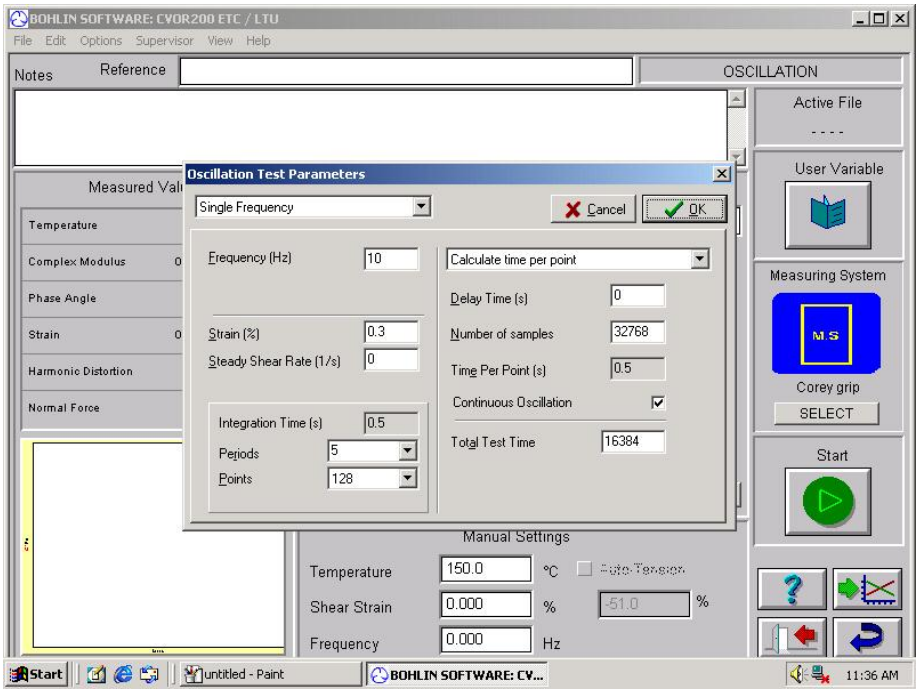

5) Once the Oscillation Test Parameters are set, click on “Options” then “Oscillation.”

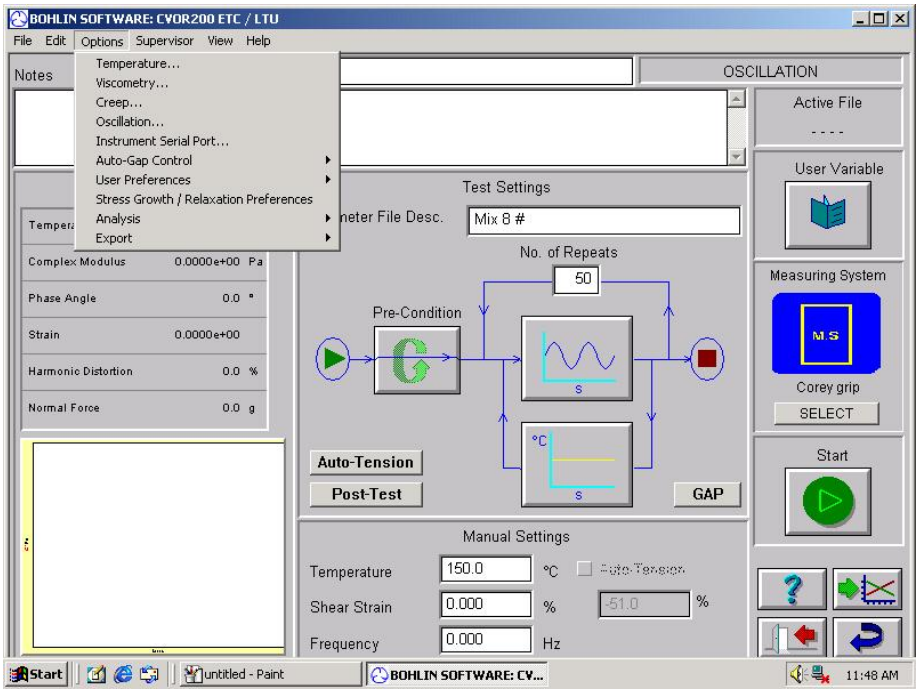

6) In the Oscillation options, click on the “User Interface” tab and select:

   a. Raw data enabled
   b. Show harmonics on graph
   c. Harmonic distortion
   d. Show strain percent
   e. Save raw data
   f. Strain control
   g. Hz

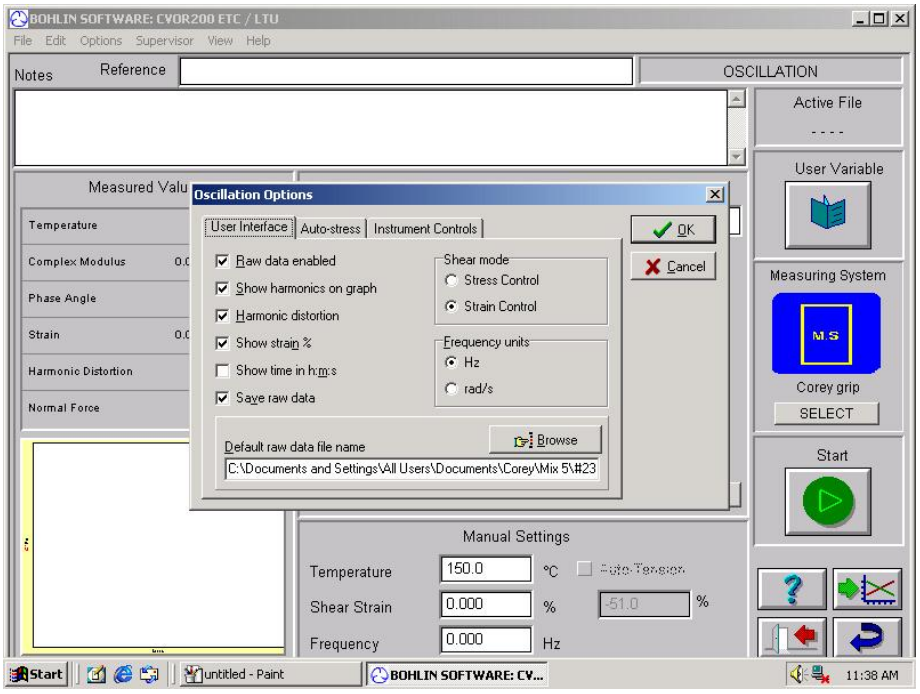

7) In the "User Interface" tab, select browse to choose where to save the raw data files. Set up folders for high strain and low strain. When saving, make sure to save in the correct folder (high strain or low strain), and make sure the file type is .raw, not .geometry compliance. There will be a Microsoft Excel file created for each data point.

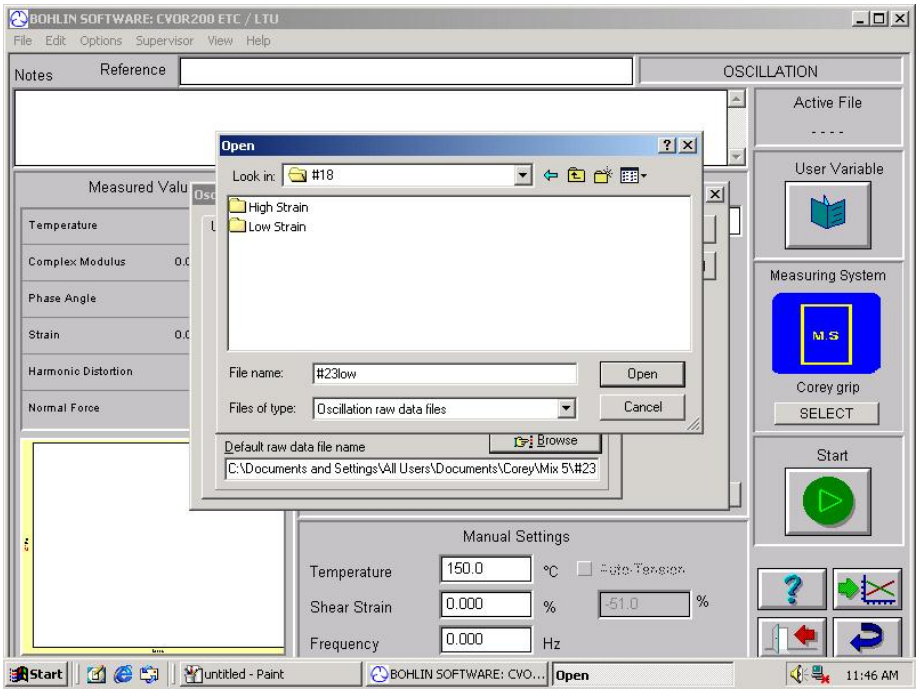

8) In the Oscillation options, click on the “Instrument Controls” tab and select:
    a. Auto-Resolution
    b. Low under Strain control sensitivity settings if the sample is very stiff, or auto if the sample is not as stiff.

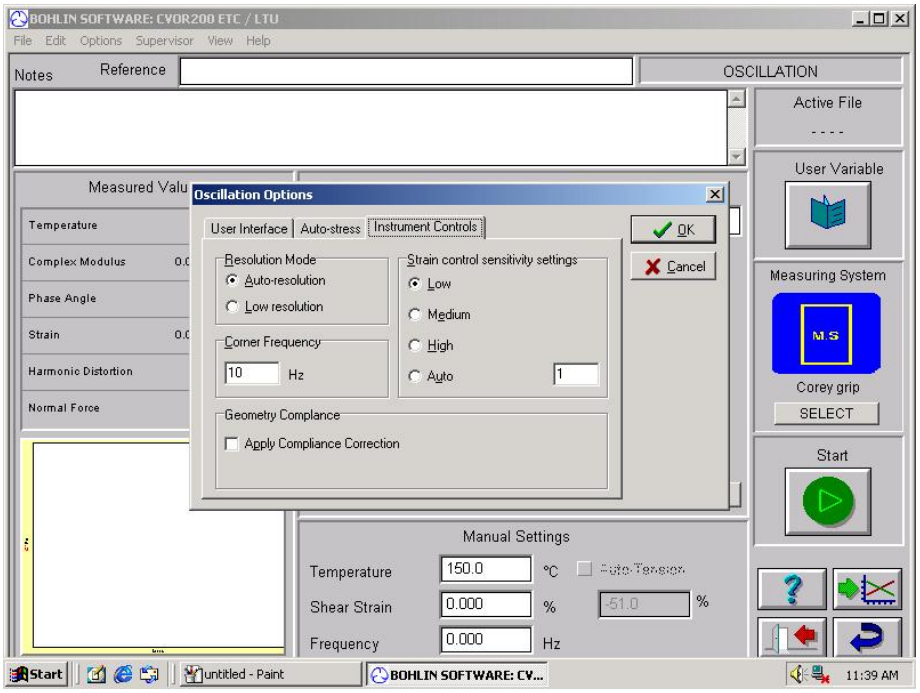

9) Click “OK” and go back to Main Oscillation screen. Press start to begin test and go to test screen. Select yes to run with current gap.

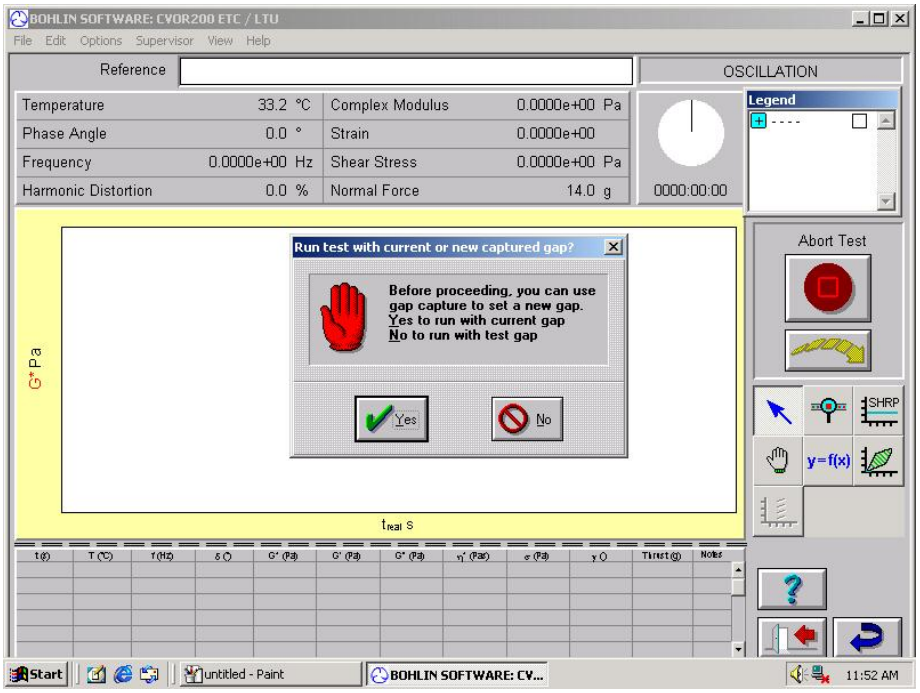

10) Wait for the specimen to reach thermal equilibrium as seen at the bottom left corner of the screen. Then select the arrow on the right to begin the test.

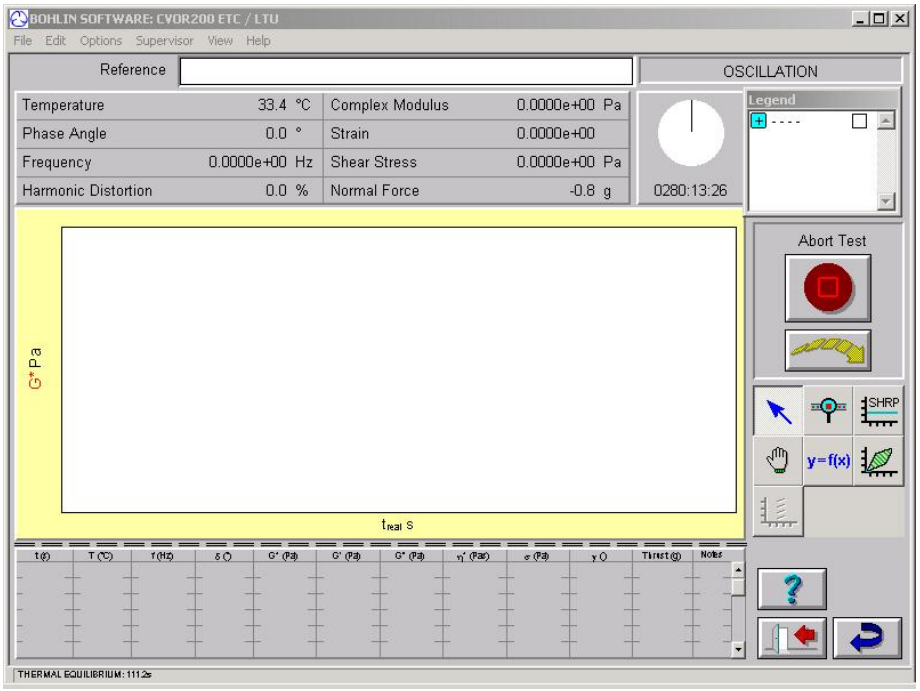

11) The test will proceed as shown below for high strain. Make sure to test low strain first and let the test run for approximately 30 seconds. For high strain, let the test run until fatigue failure is achieved.

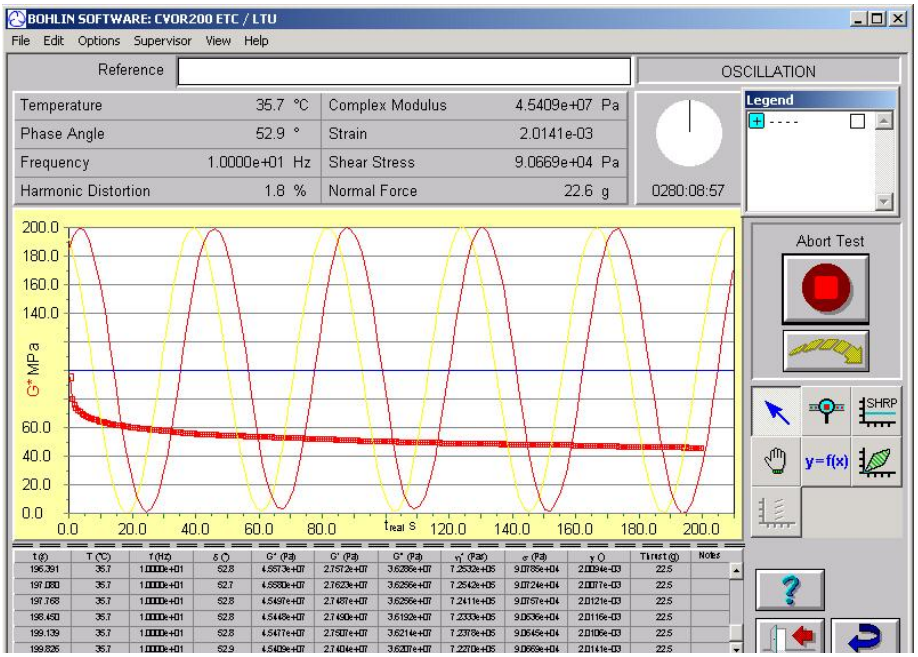

12) When the test is completed, click abort test to stop the test and save data.

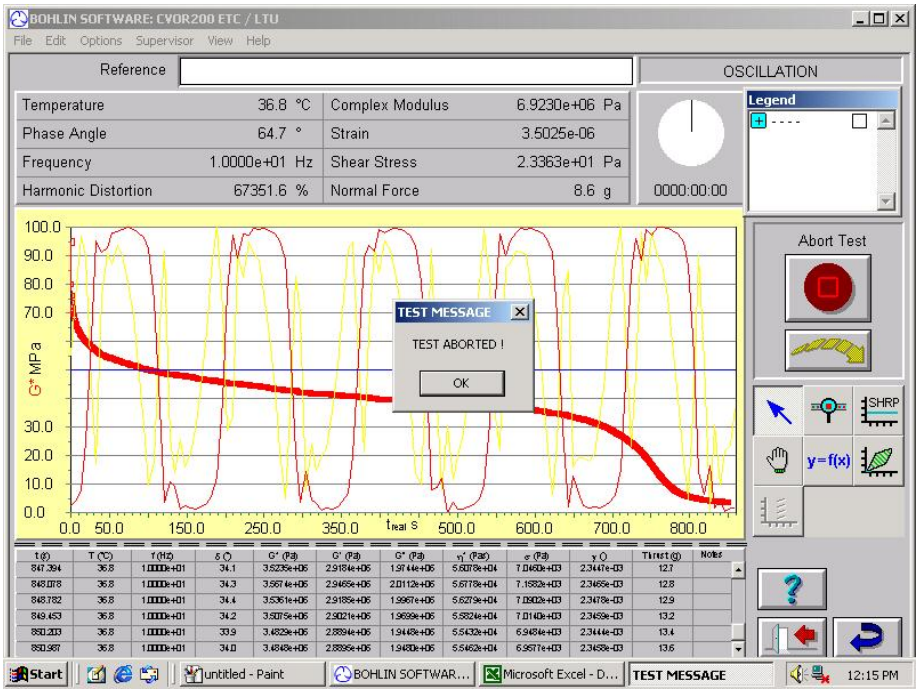

13) After clicking abort test, click the arrow on the bottom right corner to go back to oscillation main screen to save data. Click yes to save parameter settings.

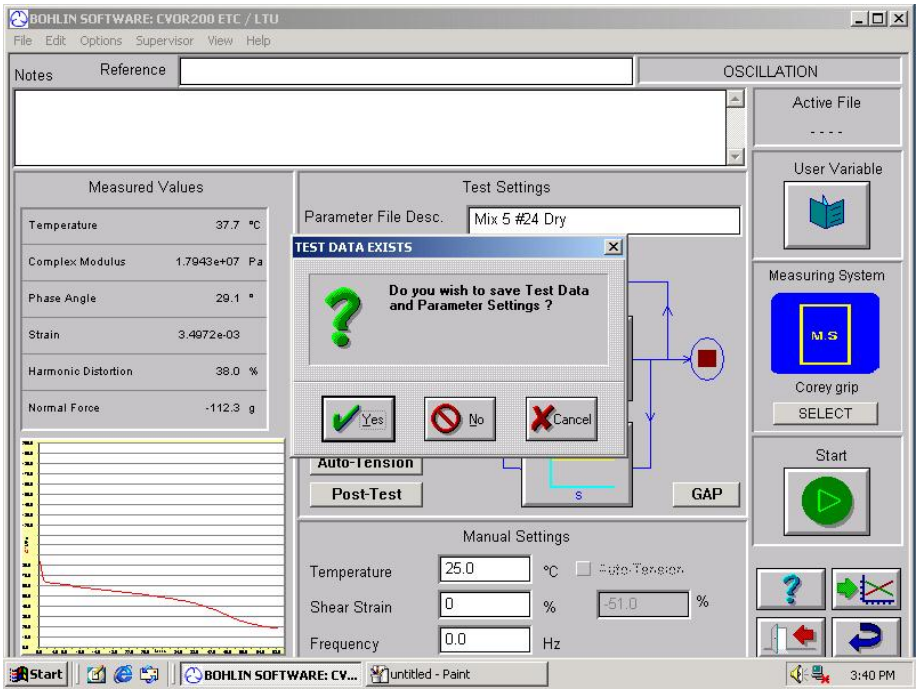

14) Save parameter settings in the desired location. The file type will be .pow. Click “save.”

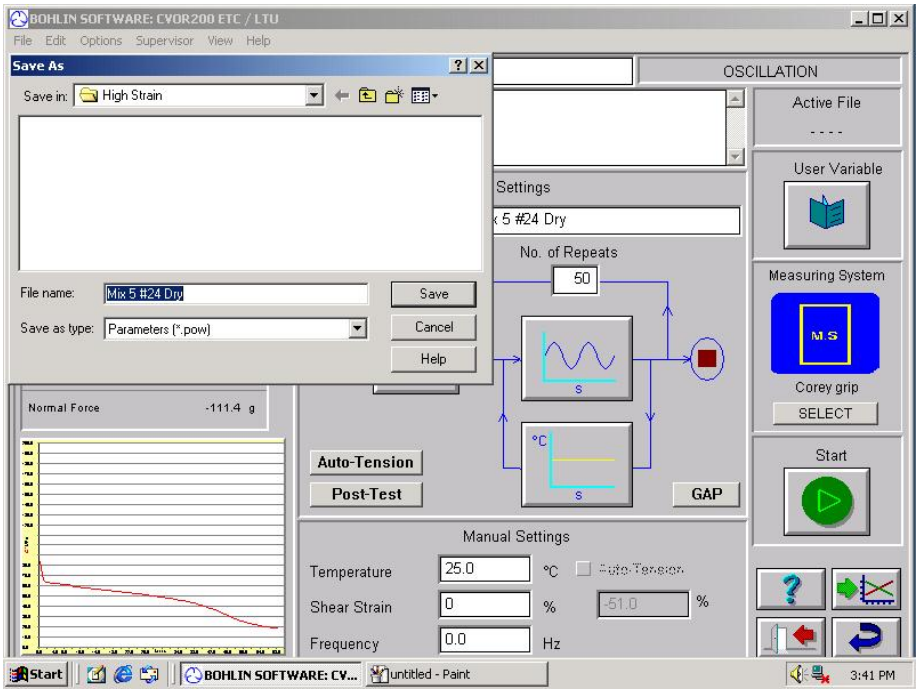

15) Click yes to save test data. As in step 13, save data in desired location, and file type will be .dow. This will be the summary file.

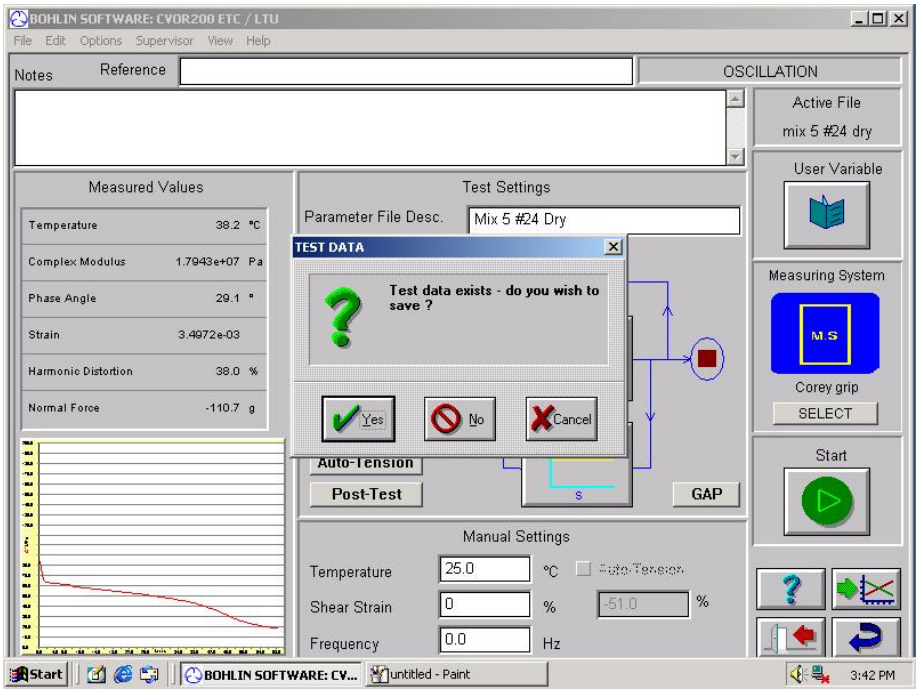

APPENDIX F

DYNAMIC MODULUS TESTING TEMPLATES AND DATA

Table F-1. Stresses Used for Dynamic Modulus Testing for Mixtures 3, 4, and 6.

Temperature (°C)	Stress (kPa) for different Frequency					
	25 Hz 200 Cycles	10 Hz 200 Cycles	5 Hz 100 Cycles	1 Hz 20 Cycles	0.5 Hz 15 Cycles	0.1 Hz 7-15 Cycles
	Dry Condition					
4.4	800	800	800	800	800	800
21.1	100	60	50	40	40	30
37.8	25	25	25	15	10	8
54.4	15	10	10	5	5	5
	Wet Condition					
4.4	700	700	700	700	650	600
21.1	90	50	40	30	30	20
37.8	20	15	15	8	8	8
54.4	10	8	5	5	5	5

Table F-2. Stresses Used for Dynamic Modulus Testing for Mixture 5.

Temperature (°C)	Stress (kPa) for different Frequency					
	25 Hz 200 Cycles	10 Hz 200 Cycles	5 Hz 100 Cycles	1 Hz 20 Cycles	0.5 Hz 15 Cycles	0.1 Hz 7-15 Cycles
	Dry Condition					
4.4	800	800	800	800	800	800
21.1	80	45	35	30	25	25
37.8	25	20	15	8	8	8
54.4	15	10	5	5	5	5
	Wet Condition					
4.4	700	700	700	700	650	600
21.1	80	45	35	30	25	20
37.8	20	15	10	8	8	8
54.4	10	5	5	5	5	5

Table F-3. Stresses Used for Dynamic Modulus Testing for Mixtures 7 and 8.

Temperature (^{O}C)	Stress (kPa) for different Frequency					
	25 Hz 200 Cycles	10 Hz 200 Cycles	5 Hz 100 Cycles	1 Hz 20 Cycles	.5 Hz 15 Cycles	.1 Hz 7-15 Cycles
	Dry Condition					
4.4	800	800	800	800	800	800
21.1	80	45	35	30	25	25
37.8	25	20	15	8	8	8
54.4	10	10	5	5	5	5
	Wet Condition					
4.4	600	600	600	600	550	500
21.1	70	35	30	25	20	20
37.8	15	10	8	5	5	5
54.4	8	5	5	5	5	5

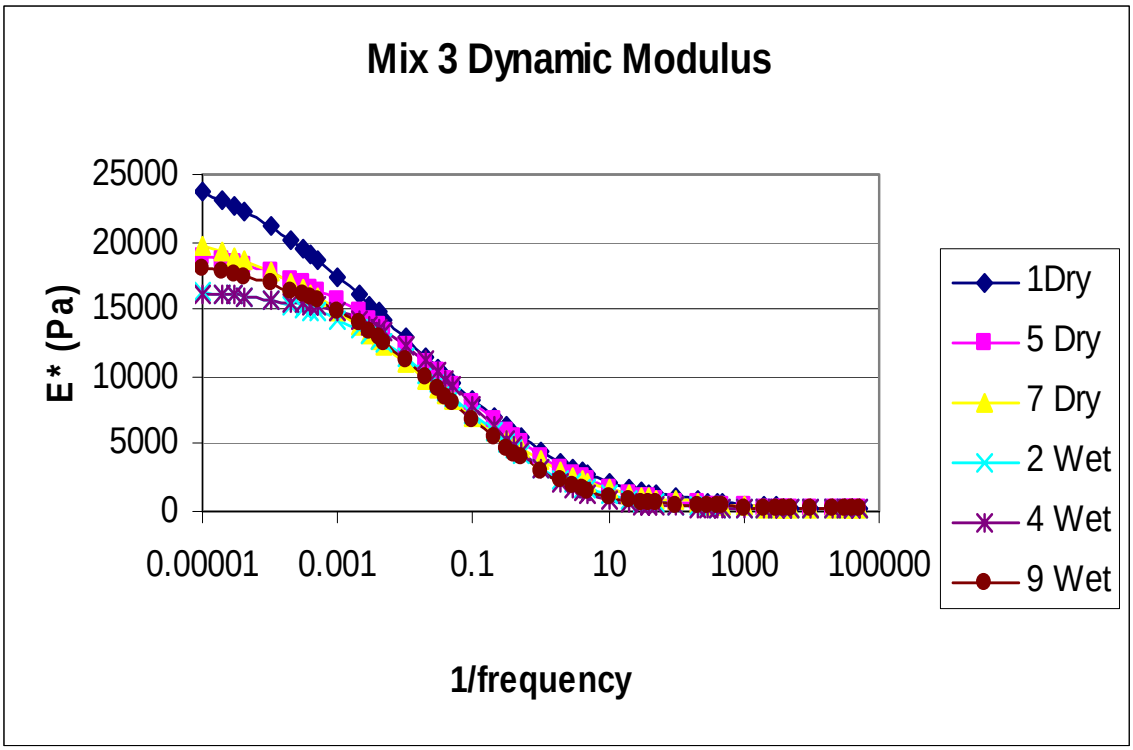

Figure F-1. Master Curve for Mixture 3.

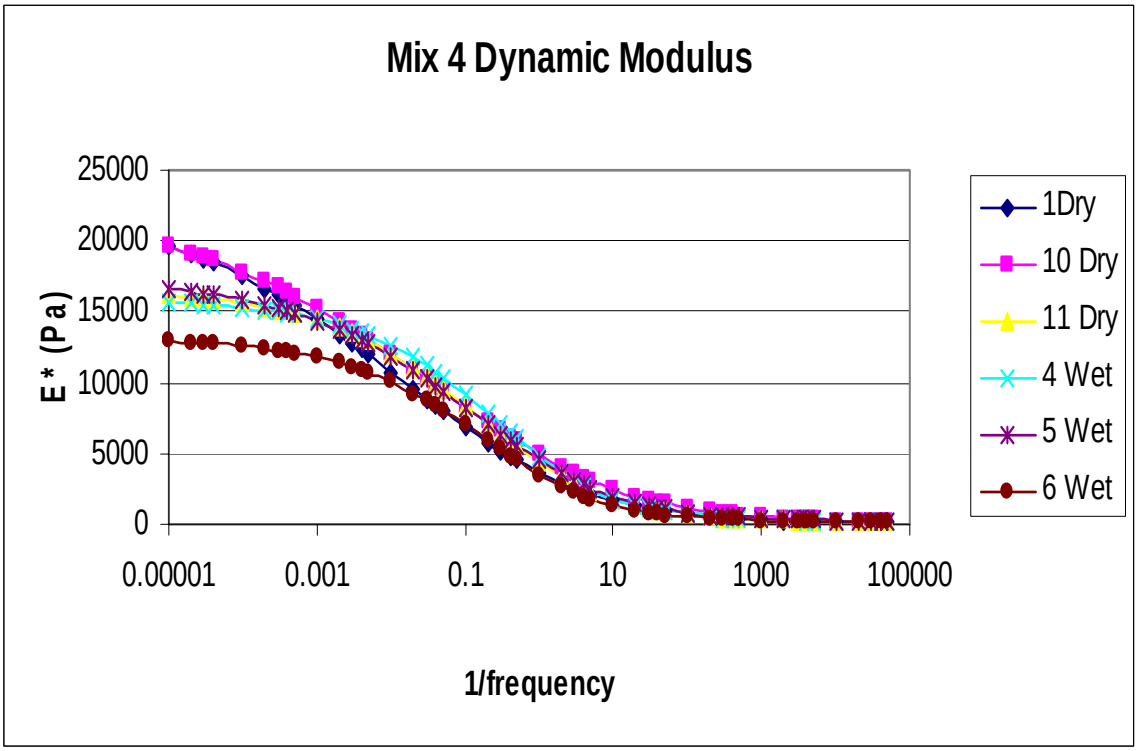

Figure F-2. Master Curve for Mixture 4.

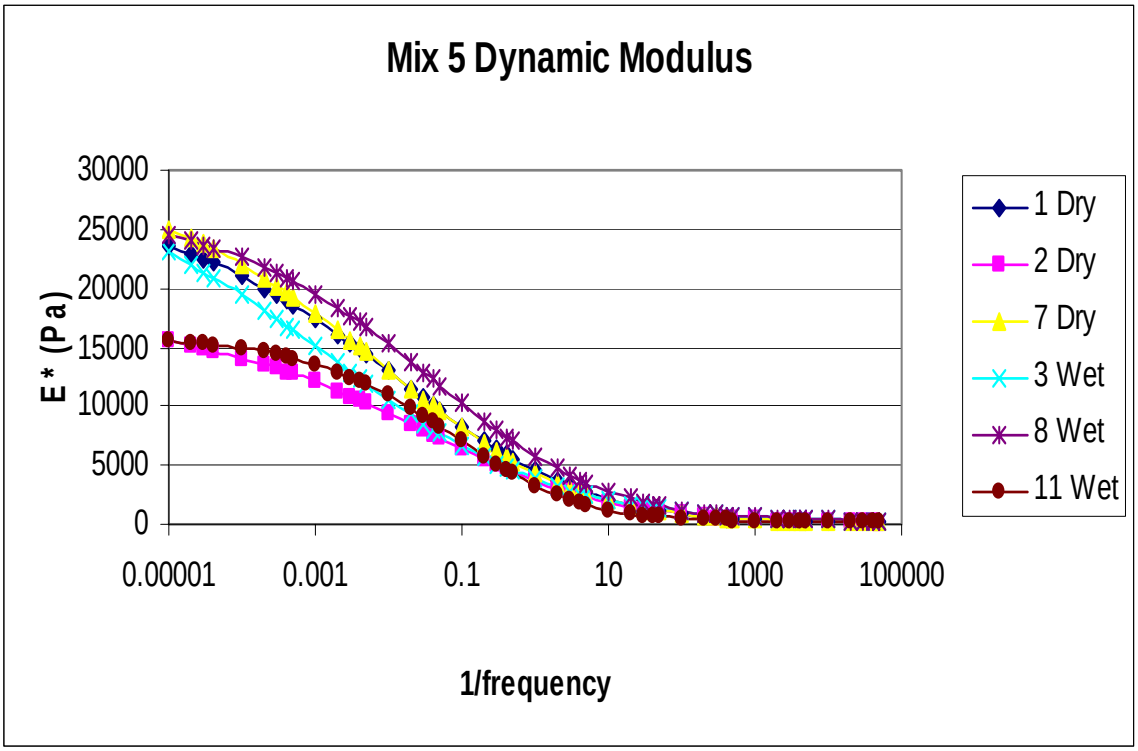

Figure F-3. Master Curve for Mixture 5.

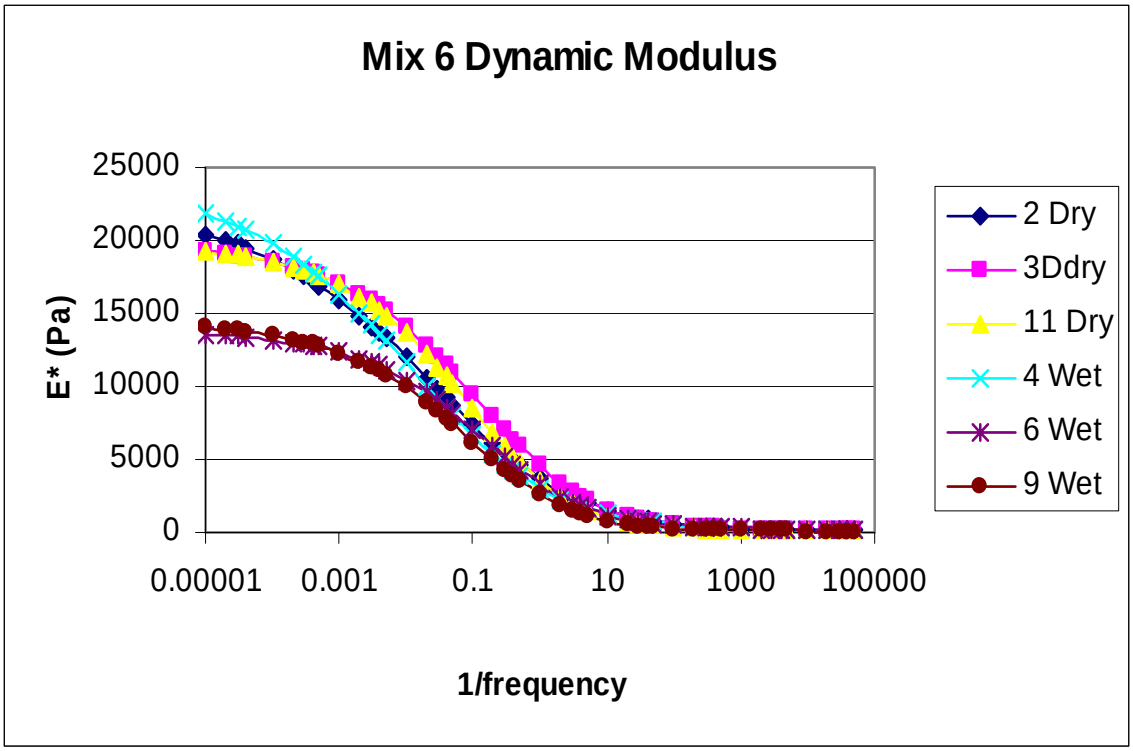

Figure F-4. Master Curve for Mixture 6.

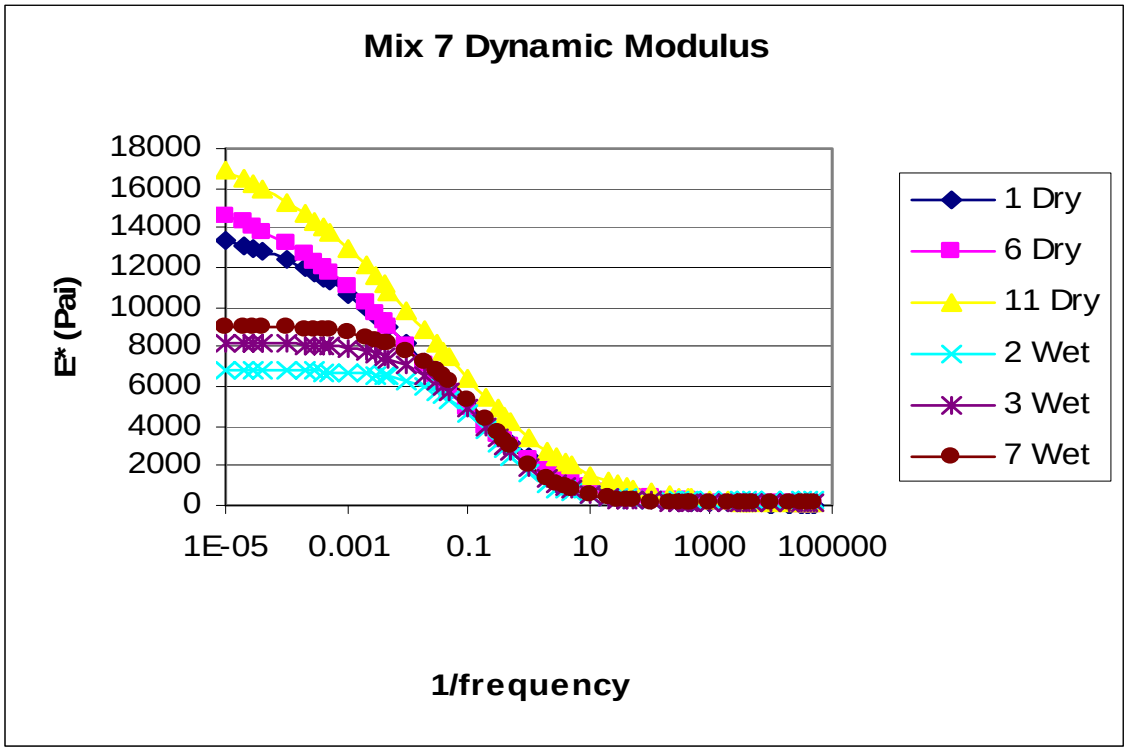

Figure F-5. Master Curve for Mixture 7.

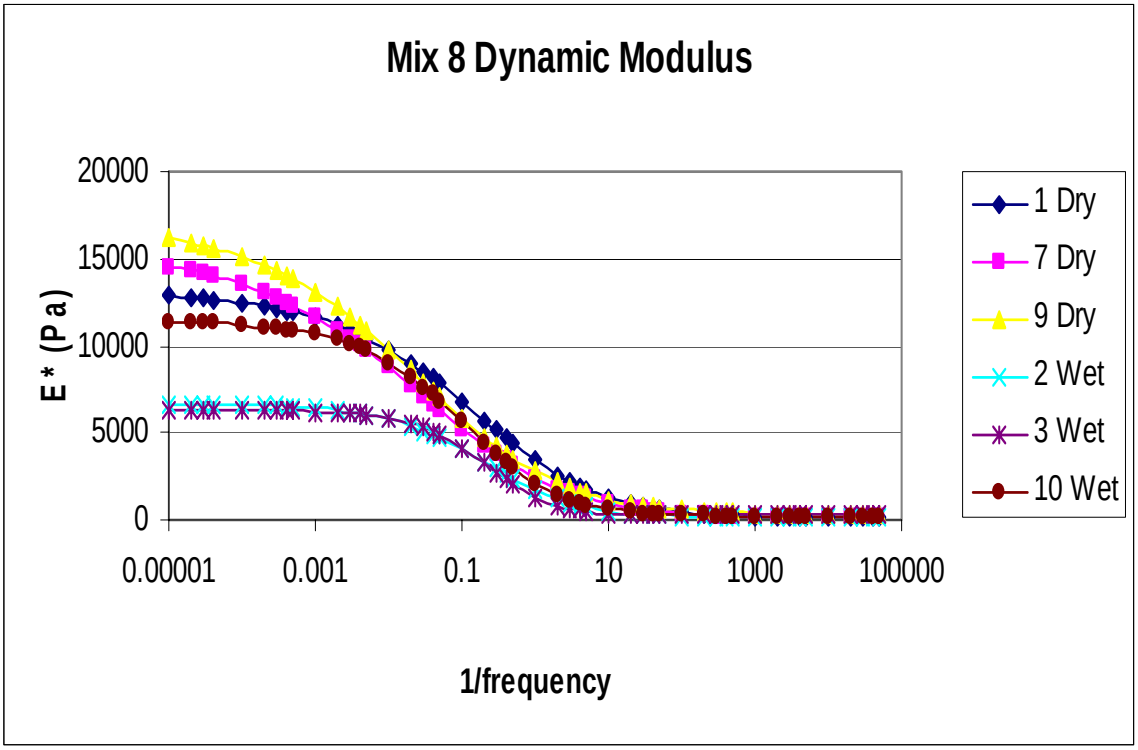

Figure F-6. Master Curve for Mixture 8.